EXPLORING MICRO X-RAY COMPUTED TOMOGRAPHY COUPLED WITH SCANNING ELECTRON MICROSCOPY AS TOOLS FOR PALEOZOIC SHALE STUDIES

By

MICHAEL R. POWERS

Bachelor of Science in Geology

Western Kentucky University

Bowling Green, KY

2013

Submitted to the Faculty of the
Graduate College of the
Oklahoma State University
in partial fulfillment of
the requirements for
the Degree of
MASTER OF SCIENCE
December, 2015

EXPLORING MICRO X-RAY COMPUTED TOMOGRAPHY COUPLED WITH SCANNING ELECTRON MICROSCOPY AS TOOLS FOR PALEOZOIC SHALE STUDIES

Thesis Approved:

Dr. Jack Pashin

Thesis Adviser

Dr. Jeffrey Byrnes

Dr. Joseph Donoghue

ACKNOWLEDGEMENTS

This project would not have been possible without the guidance and support of Dr. Jack Pashin. He continually provided feedback and suggestions throughout the project and his support was invaluable throughout the National Science Foundation Graduate Research Fellowship Program (NSF GRFP) application process. Also, thank you to Dr. Estella Atekwana for your assistance in my NSF GRFP application. Thanks to my committee members, Drs. Jeffrey Byrnes and Joe Donoghue, for your guidance. Thanks to Dr. Tyler Ley, Masoud Moradian, Beth Vanden Berg, Brent Johnson, and Lisa Whitworth for your assistance with instrumentation. Special thanks to my family and friends for your continued support throughout my academic career. Lastly, thanks to the NSF for the financial support provided for this project. Cores used in this study were graciously made available by the Geological Survey of Alabama, the Oklahoma Geological Survey, EOG Resources, Newfield Exploration Company, CNX Gas, and Virginia Tech.

Note: This material is based upon work supported by the National Science Foundation Graduate Research Fellowship under Grant No. 1144467. Any opinion, findings, and conclusions or recommendations expressed in this material are those of the authors(s) and do not necessarily reflect the views of the National Science Foundation.

Name: MICHAEL RAY POWERS

Date of Degree: DECEMBER, 2015

Title of Study: EXPLORING MICRO X-RAY COMPUTED TOMOGRAPHY COUPLED WITH SCANNING ELECTRON MICROSCOPY AS TOOLS FOR PALEOZOIC SHALE STUDIES

Major Field: GEOLOGY

Abstract: Despite the ubiquity of shale in the rock record, the complex physical, biological, and chemical processes that determine its properties has inhibited our understanding of its origin and reservoir characteristics. The fine-grained texture and heterogeneity of shale, moreover, makes analysis challenging. Accordingly, the study of shale requires a systematic, multidisciplinary approach. Although scanning electron microscopy/energy dispersive spectroscopy (SEM/EDS) and x-ray computed tomography (CT) have been recognized as useful instruments for observing shale fabric on microscopic to nanoscopic scales, these tools remain underutilized. CT provides a noninvasive way to image specimens in three dimensions, and this thesis explores its utility for shale analysis.

Shale samples from several Paleozoic formations in the southeastern and south-central United States were analyzed during this study. Qualitatively, CT facilitated the characterization of heterogeneity and a variety of depositional, diagenetic, and structural features. Features that were imaged include micro-scale rock fabric, physical and biogenic sedimentary structures, body fossils, diagenetic minerals, fractures, and faults. Quantitatively, data from CT were used to calculate volumetric percentages of porosity and mineral constituents. SEM/EDS data were collected from the samples used for CT analysis. The CT was used for pinpointing locations in which the microfabric could be further resolved and analyzed using SEM. SEM was then used observe pores, sulfide morphology, fossils, mineral grains, and fracture-filling cement. EDS allowed for rapid and straightforward determination of mineral composition. In turn, data gathered from SEM/EDS were used to supplement interpretations made from the CT analysis. This work demonstrates the utility of incorporating CT and SEM/EDS analyses into geologic workflows for the evaluation of shale. By using these technologies, microstructure can be related to macrostructure, thereby informing a range of sedimentologic, structural, and petrologic interpretations.

TABLE OF CONTENTS

Chapter Page

LIST OF TABLES

Table Page

LIST OF FIGURES

Figure Page

CHAPTER I

INTRODUCTION

I. 1 Shale overview

Shale is commonly defined as a fine-grained, organic-rich, detrital sedimentary mudrock in which 50% of the rock by weight is composed of clay size particles less than 3.9 μm (Potter and Pryor, 1980). Shale is an extremely complex rock type that may be composed of clay minerals, quartz silt, carbonate, and kerogen, and in practice includes strata that can be more properly classified as siltstone or carbonate (Wignall, 1994). Shale also contains calcite, dolomite, pyrite, phosphate, and a variety of other minerals. The dark color of many shale units is due primarily to organic matter and finely disseminated pyrite (Trask and Patnode, 1942; Berner, 1980). Generally, the distinguishing characteristics of shale and mudstone are that shale has fissility, whereas mudstone does not. For the sake of simplicity, the two terms will be used interchangeably in this thesis. In general, shale constitutes about two thirds of the sedimentary record, and so an understanding of shale deposition is a key to the reconstruction of ancient environments and depositional processes (Schieber, 2011). These deposits are of great economic interest as hydrocarbon source rocks, hydrocarbon reservoirs, and host strata for ore deposits (Potter et al., 1980). In addition, many shale units are reservoir seals (Surdam, 1997; Downey, 1984). More than 90% of the world's recoverable oil and gas reserves are thought to have been generated from organic-rich shale (Klemme and Ulmishek, 1991).

I. 2 Statement of problem

While shale has been drilled routinely for gas production since the early 1800s (Nuttall et al., 2009), its potential for producing economic volumes of oil has not always been recognized. In the past, shale was recognized primarily as a source and seal, so most sedimentologic research focused on sandstone and carbonate strata due to their reservoir potential and overall economic significance. Only recently, due to the combination of precision horizontal drilling and multi-stage hydraulic fracturing, has shale emerged as a world class petroleum reservoir. As a result, there has been an increased interest in shale research, which, in turn, has caused the gaps in our understanding of shale to to begin closing. While shale research is no longer the wide open frontier that it was in the early 1990s, it is still fertile ground that can yield increased understanding of the geologic record and natural resource exploration and development.

In regards to classification schemes for sedimentary rock types, the Folk (1959) and Dunham (1962) classification schemes for carbonates and the McBride (1963) and Folk (1974) sandstone classification schemes have garnered widespread acceptance amongst geologists. On the contrary, many classification schemes have been proposed for shale. These schemes are based on grain size (Lewan, 1979), texture (Shepard, 1954), and mechanical-chemical stability (Loucks et al., 2012), but no single classification has had sufficient utility to gain widespread acceptance by the geologic community. No proposed classification has been universally accepted in part because it is impossible to devise a simple and practical classification that adequately treats all important shale attributes and addresses all purposes for classification.

Depositional environments of mudrock units in the North American craton span everything from paleosols and tidal flats to epicontinental shelf, slope, and basin floor environments. Despite the ubiquity of shale in the rock record, the complex interplay among the physical, biological and chemical processes that determines its properties has inhibited our

understanding of its origin (Schieber, 1998). As such, interpretations that rely on a single perspective typically are inconsistent with conclusions obtained from multiple avenues of inquiry. Accordingly, successful studies of mudstone fabric require the integration of all available sedimentologic, paleontologic, petrographic, and geochemical observations. In addition, the fine-grained texture, compositional variability, and facies heterogeneity of shale make its analysis challenging. Consequently, the full range of sedimentary processes associated with shale remains a vital subject of scientific endeavor.

Another notable topic of discussion is faulting and fracturing in the field of shale research. Natural fractures have long been considered the primary factor controlling oil and gas production in low-porosity and low-permeability shale reservoirs. Production from these self-sourced host rocks relies heavily on natural fractures, as they provide effective permeability and a means for hydrocarbons to migrate to the producing wellbores. Hydraulic fracturing commonly reactivates natural fractures, as evidenced by image logs and microseismic event patterns (Gale et al., 2007, 2014). The Barnett Shale typifies this, as gas production relies upon reactivation of natural opening-mode fractures via hydraulic-fracture stimulation (Gale et al., 2007). Conversely, fractures can compromise seals and may cause undesirable complications for unconventional reservoirs. A remarkable example that demonstrates the sensitivity of the economics of hydrocarbon extraction in a structurally complex self-sourced reservoir is the U.S. Energy Information Administration's recently reported 96% reduction in estimated recoverable oil from the Monterey Shale in California (Ferrill et al., 2014). Thus, the role of natural fractures often plays a key role in the success or failure of unconventional reservoir plays. Fracture systems in shale are heterogeneous; they can enhance or reduce producibility and affect rock strength and fluid conductivity (Gale et al., 2014). Gale (2014) also points out that the role of microfractures is potentially critical in production from shale, yet it is not fully understood.

Multidisciplinary workflows are an effective way of advancing the state of research (e.g., Hill and Jarvie, 2007; Pashin et al., 2011; Ross and Bustin, 2008). Using new and emerging investigative approaches, like micro x-ray computed tomography (micro-CT), coupled with the many well-established tools at our disposal, may prove to be an excellent way of progressing our understanding of shale. Thus, the focus of this thesis is to help fill the void in shale research by exploring the utility of micro-CT coupled with scanning electron microscopy (SEM) as investigative tools and incorporating them into an established workflow from core and outcrop description to nanoscopic analysis. Micro-CT is underutilized in the study of consolidated sedimentary rocks, and the goal of this work is to identify its full capabilities as well as its limitations in the analysis of shale. CT analysis is an evolving technology, so today's limitations may be overcome as technology progresses.

CHAPTER II

PREVIOUS WORK

II. 1 Workflows Shale investigation is a diverse and evolving field of geologic research. As such, the study of shale requires a systematic, multidisciplinary approach. Many modes of investigation have been utilized in the study of shale. While there is overlap among several approaches, each possess their own inherent advantages. Tools for shale evaluation include but are not limited to: core descriptions, graphic core logs, x-radiography, and wireline well logs for stratigraphic, sedimentologic, and structural evaluation; thin sections and x-ray diffraction for petrographic analysis; x-ray fluorescence and isotope geochemistry for geochemical analysis; rock-eval pyrolysis for measuring organic content and thermal maturity; porosimetry, pressure and pulse-decay permeability determination, grain density and fluid saturation analyses; adsorption isotherms; and SEM/EDS and small angle x-ray and neutron scattering for microfabric and nanofabric evaluation.

Recent studies have proven the usefulness of establishing integrated workflows to guide their inquiries (e.g., O'Brien and Slatt, 1990; Ross and Bustin, 2008; Pashin et al., 2011). A study of production of natural gas from diverse shale formations (Pashin et al., 2011) is a useful example of how valuable establishing a multidisciplinary workflow can be. The study demonstrates how geologic factors from megascopic to nanoscopic scale influence each other and

reinforce the need for an integrated methodology for shale evaluation. The approach incorporates many geologic variables (e.g. sedimentology and stratigraphy, structural geology, hydrodynamics and geothermics, petrology and geochemistry, gas storage, petrophysics, resources, and reserves).

The workflow presented by O'Brien and Slatt (1990) is a useful approach that was adapted and modified for this thesis research. Their book outlines a three-fold approach involving the use of x-radiography, petrography and SEM. The workflow in this research has substituted CT for x-radiography and has incorporated the use of argon ion milled samples, along with freshly broken surface samples, for the SEM work.

II. 2 X-radiography and x-ray computed tomography

In the past, the use of x-rays for observing the internal fabric of rocks has revolved around the use of x-radiography (Bouma, 1969; O'Brien and Slatt, 1990). The problem with the classic approach to x-radiography is that it is a destructive method in which samples must be slabbed, which can be very problematic when dealing with fissile shale and other delicate samples. This problem was solved when x-ray computed tomography (CT), which was established in the biomedical field, was adapted for other types of research, such as geology and materials science. CT has been recognized as a revolutionary tool for imaging internal rock fabric (Holler and Kögler, 1990; Ketcham and Carlson, 2001; Mees et al., 2003). Because it is a relatively nondestructive method, degradation of samples during preparation can be minimized or avoided. CT analyses of consolidated sedimentary rocks have numerous applications: imaging and evaluating pore geometry and distribution (Spanne et al., 1994; Ketcham and Iturrino, 2005; Taud et al., 2005); imaging of multiphase fluid flow experiments (Wellington and Vinegar, 1987); evaluating deformation structures (Soh et al., 1993; Ashi, 1993); evaluating ore deposits (Kyle and Ketcham, 2015); imaging of fossils (Penney et al., 2007; Dierick, 2007); and performing three-dimensional grain fabric measurements (Ketcham, 2005).

Indeed, the potential for using CT imagery to solve geological problems is only beginning to be explored. Furthermore, the perpetual advancement of CT technology is continually improving image resolution and overall functionality. While some CT studies have imaged sedimentary structures in unconsolidated sediment (Soh et al., 1993; Holler and Kögler, 1990), relatively few have focused on such structures in consolidated rocks (Shirai et al., 2007). The same can also be said for the study of fracturing and faulting in sedimentary rocks. Because of its origin as a medical diagnostic tool, the ideal CT scanner for geologic applications does not exist (Cnudde et al., 2006). With CT scanning of shale in its infancy, this work will provide another investigative approach to consider when studying shale and organizing analytical workflows for sedimentologic, structural, and reservoir studies.

II. 3 Scanning electron microscopy/energy dispersive spectroscopy

Several microfabric investigations over the past few years have demonstrated the utility of using SEM/EDS on argon ion milled samples for characterizing pore types in shale (Camp et al., 2013). In particular, Slatt and O'Brien (2011) showed how pore types in the Barnett and Woodford gas shales contribute to understanding gas storage and migration pathways in fine-grained rocks. Another study on the Woodford Shale by Curtis et al. (2012) showed how increasing thermal maturity played a role in the development of organic porosity. A broader study by Loucks et al. (2012) discussed the spectrum of pore types and networks in mudrocks and created a descriptive classification for matrix-related mudrock pores based on their findings. It is apparent that SEM/EDS work on argon ion milled samples of shale is an emerging trend for high-resolution studies of microfabric.

.

CHAPTER III

METHODOLOGY AND TECHNIQUES

Shale samples from a variety of formations were analyzed from a series of basins in the southeastern and south-central United States (Fig. 3). Having a broad spectrum of samples from numerous different depositional environments enabled a large variety of observations to be made. A total of 30 shale samples from nine different cores in four different basins and a thrust belt were scanned with a Zeiss Xradia VersaXRM 410 CT scanner (Fig. 4) using parameters tailored to each individual sample (Table 1). The samples are from six different formations ranging from Cambrian to Pennsylvanian in age (Table 2).

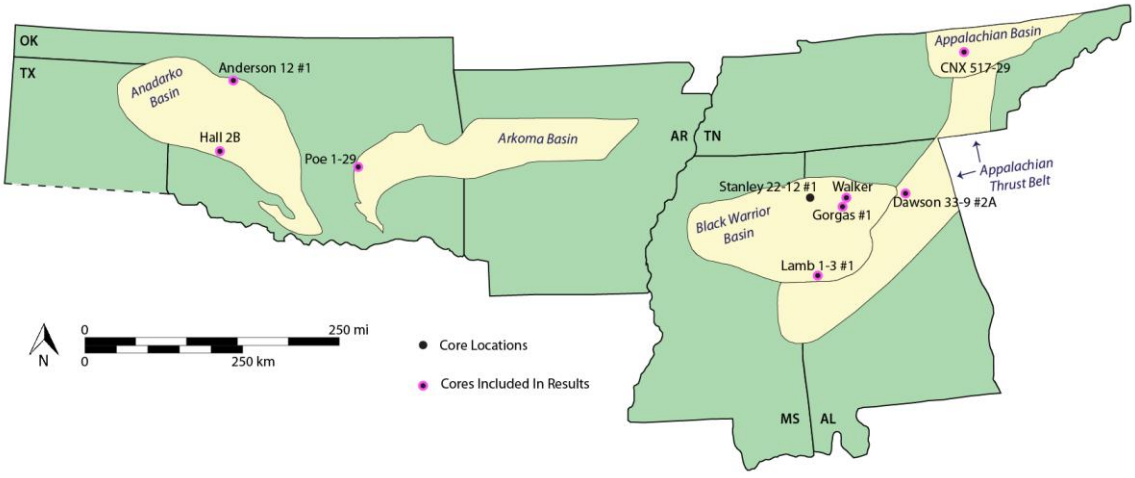

Figure 1. Generalized map showing the locations of cores used in this study.

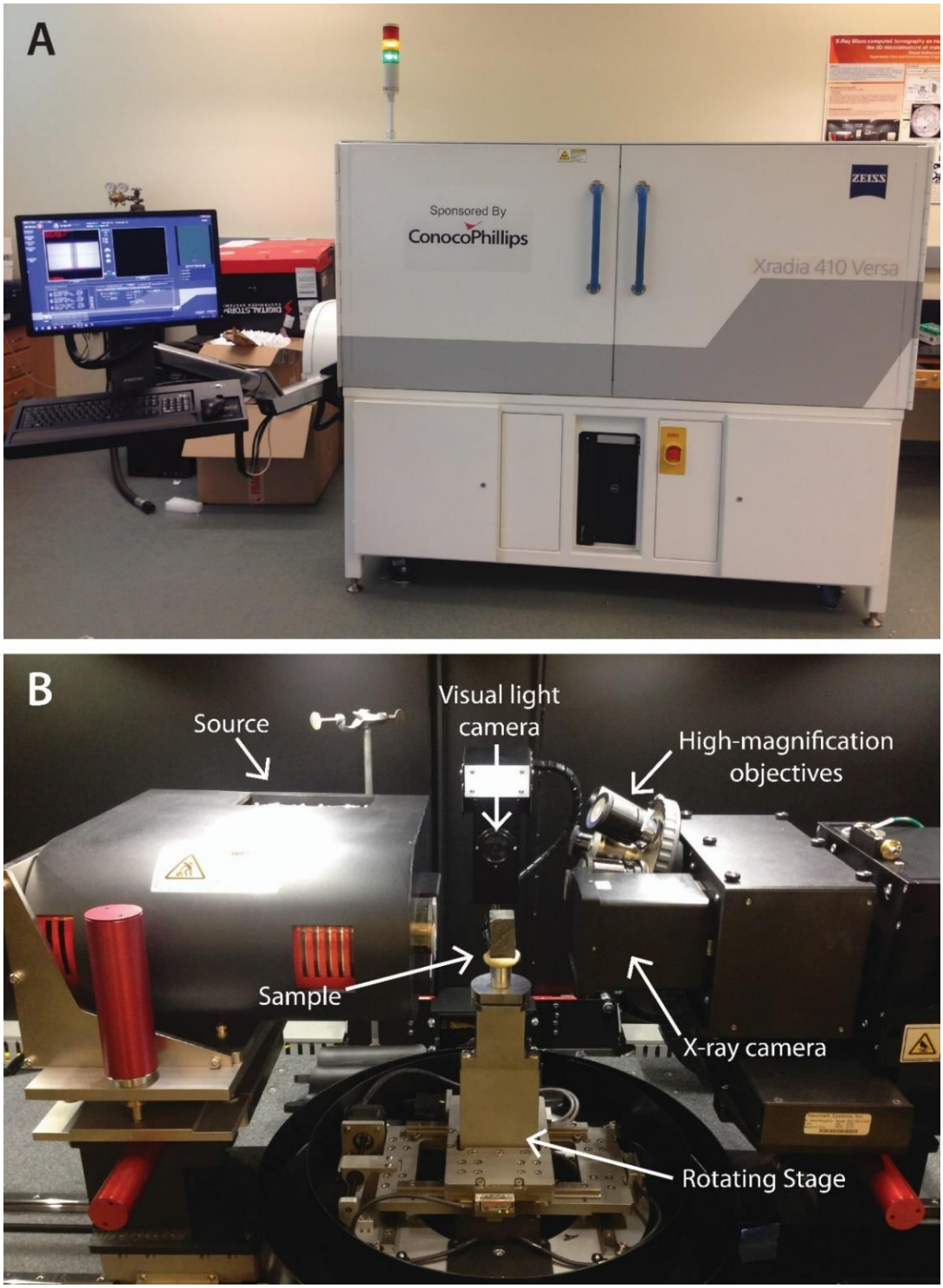

Figure 2. Photographs of the Zeiss Xradia VersaXRM 410 CT scanner. (A) The whole unit with the monitor used to scan, reconstruct, and process images. (B) The internal components of the CT scanner that are used for sample placement and imaging.

Sample Data			Scanning Conditions			
Core Name	Depth (ft)	Dimensions (mm)	Voxel Size (µm)	Scan Time		X-Ray Energy (kV)
				Hours	Minutes	
Dawson 33-9 #2 A	* 7565.7	13 x 26 x 4	25.427	3	50	80
Lamb 1-3 #1	* 9167.5	90 x 60 x 50	48.972	6	30	149
	* 9173.5	30 x 13 x 2	19.274	4	30	55
	* 9180.0	36 x 25 x 24	42.495	2	44	147
	* 9192.5	5 x 4 x 4	0.899	12	41	90
CNX 517-29	* 3200.0	16 x 9 x 7	18.515	3	2	80
Anderson 12 #1	* 6839.8	23 x 30 x 20	37.167	3	0	135
	* 6843.6	22 x 16 x 14	25.896	2	56	115
	6874.2	11 x 11 x 6	17.963	2	34	84
	6882.7	31 x 27 x 11	34.758	4	0	118
	6875.5	29 x 19 x 20	35.239	3	7	124
	6893.2	27 x 20 x 18	33.798	3	45	125
	* 6900.7	33 x 21 x 13	30.680	3	45	130
	6927.5	35 x 12 x 13	41.503	3	1	100
Poe 1-29	7747.0	30 x 20 x 22	34.170	3	5	114
	7772.2	35 x 20 x 21	41.208	3	27	108
	7832.0	21 x 26 x 25	36.332	3	0	128
	* 7843.7	30 x 32 x 24	39.240	3	0	122
	* 7848.0	32 x 22 x 20	37.821	3	18	112
	7849.6	28 x 19 x 18	33.793	2	46	105
Hall 2B	5887.5	38 x 19 x 17	41.395	2	57	95
	* 5899.0	26 x 18 x 17	30.981	3	3	120
	5903.0	28 x 23 x 23	35.788	3	1	115
	6172.0	37 x 22 x 22	43.430	4	0	110
	* 6178.5	36 x 20 x 17	41.587	3	2	105
Stanley 22-12 #1	4644.8	14 x 10 x 10	18.515	2	45	140
Walker	2616.0	20 x 26 x 21	37.118	3	0	147
	* 2619.0	25 x 21 x 17	31.699	2	44	147
Gorgas #1	* 1235.6	35 x 28 x 28	43.646	3	0	149
		0.3 x 0.2 x 0.2	0.475	13	19	40

Table 1. Sample depths, dimensions and scanning conditions. Samples with asterisks are discussed in detail in this thesis.

Core Data			
Age	**Formation**	**Well Name**	**Location**
Pennsylvanian	Pottsville Formation	* Gorgas #1	Walker County, AL
Mississippian	Floyd tongue of Bangor Limestone	* Walker	Walker County, AL
	Pride Mountain Formation	Stanley 22-12 #1	Lamar County, AL
Devonian	Woodford Shale	* Hall 2B	Caddo County, OK
		* Poe 1-29	Hughes County, OK
		* Anderson 12 #1	Garfield County, OK
	Chattanooga Shale	* CNX 517-29	Campbell County, TN
		* Lamb 1-3 #1	Greene County, AL
Cambrian	Conasauga Formation	* Dawson 33-9 #2 A	St. Clair County, AL

Table 2. Well locations and the formations analyzed with their corresponding ages. Note: Only the well names with asterisks are discussed.

Using the reconstructed CT scans to pinpoint areas of interest for microfabric analysis, 11 argon ion milled and 3 freshly broken surface samples were observed and analyzed using a FEI Quanta 600 SEM/EDS unit. Samples were argon ion milled using a JEOL IB19500CP cross section polisher and were sputter coated for analysis using a Balzers Union MED 010 Au/Pt coater. A wealth of supporting data is available for the cores that were analyzed (e.g., Pashin et al., 2011; Clark et al., 2013; Callner, 2014), including core descriptions, graphic core logs, geophysical well logs, thin sections, x-ray diffraction mineralogy, geochemical data, rock-eval pyrolysis, tight rock analyses (porosity, pulse-decay permeability, grain density, fluid saturation, and adsorption isotherms). These supplementary data were drawn upon as appropriate when performing this thesis research.

III. 1 Instrumentation

X-ray computed tomography (CT) is a nondestructive technique for visualizing features within solid objects, and for obtaining digital information on their 3-D geometry and physical properties. The way it works is an x-ray source emits x-rays that pass through a rotating sample and are then captured by an x-ray camera (Fig. 1). The x-ray camera consists of a scintillator and photo detector. After the x-rays have passed through the sample, they first hit the scintillator, which creates light, and then that light is captured by the photo detector. Upon capturing the light, a photographic image called a radiograph, is taken. Because the sample is rotating, multiple radiographs are taken. After the scan is finished, these radiographs can be stitched together into CT slices by a process known as reconstruction. Stacking a set of contiguous CT slices enables the user to render a full 3D tomograph of the sample.

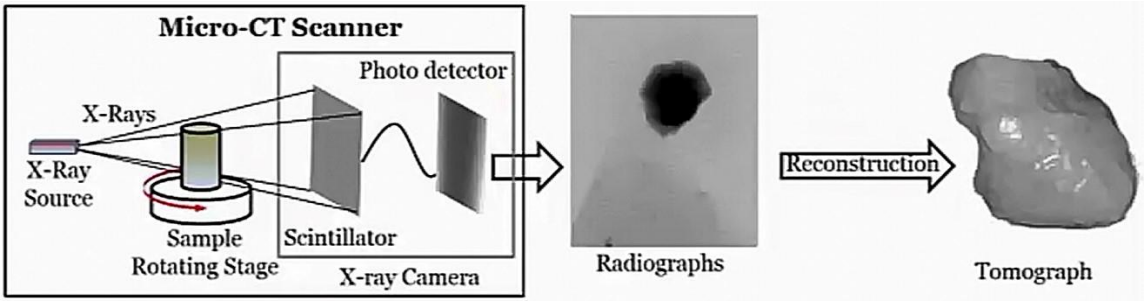

Figure 3. General overview of CT scanning and reconstruction (courtesy of Dr. Tyler Ley).

A typical digital image is composed of pixels (picture elements), whereas a CT slice is composed of voxels (volume elements). The CT slices that are generated via reconstruction are along the XY plane of the sample and have a thickness of one voxel. Higher voxel resolution can be acquired by decreasing the size of a sample. The gray levels in a slice correspond to x-ray attenuation, which reflects the proportion of x-rays scattered or absorbed as they pass through each voxel. X-ray attenuation is a function of x-ray energy and the density of the material being imaged. The denser materials will appear bright in the final image, while the less dense materials

will appear darker. By obtaining a contiguous set of slices, volumetric data for all or part of a sample can be obtained, allowing for three-dimensional inspection and measurement of features of interest. While the output of CT generally leads to straightforward interpretation, beam hardening and partial-volume effects can render the data problematic for quantitative use. Beam hardening is the most commonly encountered artifact in CT scanning. It is caused by the x-ray beam losing intensity as it passes through an object and results in the edges of an object appearing brighter than then the center, even if the material is the same throughout. The partial-volume effect occurs when a voxel is comprised of more than one constituent. Because each voxel represents the attenuation properties of a specific material volume, if that volume is comprised of a number of different substances then the resulting CT value represents some average of their properties. This causes material boundaries to be blurred to some extent and can lead to erroneous determinations of isolated nano- to micro-scale features, such as pores. However, the upside to this effect is the ability to image contiguous features that are below the voxel resolution of a scan, such as microfractures.

Scanning electron microscopy (SEM) is a form of microscopy that, instead of using light, produces highly magnified images of a sample by scanning it with a focused beam of electrons. The beam of electrons is produced by an electron gun at the top of the microscope. The beam is held within a vacuum and travels through electromagnetic fields and lenses, which focus the beam into the sample. When the beam contacts the sample, electrons and x-rays are scattered from the sample. Detectors collect these x-rays, backscattered electrons (BSE), and secondary electrons and convert them into a signal that is used to produce the final micrographic image. One of the most common SEM detectors, and the one used for this thesis research, is the Everhart-Thornley Detector (ETD), which collects both secondary and back-scattered electrons (Everhart and Thornley, 1960).

Due to their low energy, secondary electrons originate within a few nanometers of the sample surface (Goldstein et al., 2012) and are useful for imaging sample topography. Conversely, BSE consist of high-energy electrons that interact with much larger volumes of the sample. Heavier elements backscatter electrons more strongly than light elements and will appear brighter in the final image. Because of their larger interaction volume and elemental sensitivity, BSE are used to detect contrast between areas with different chemical compositions (Goldstein et al., 2012). Energy dispersive spectroscopy (EDS) is an analytical technique used in SEM for the detection of x-rays that are generated when the beam interacts with the sample. The x-rays are collected by a detector and are converted to voltage signals. These signals are then processed and displayed in an EDS spectrum which allows for identification of particular elements and their relative proportions. By coupling SEM with EDS, microfabric elements can be observed and analyzed compositionally.

The advent of argon ion milling has revolutionized the preparation of samples for SEM/EDS analysis. Argon ion milling simplifies the preparation of samples and makes it possible to prepare highly polished sections of samples with minimal surficial artifacts. Use of the broad argon ion beam eliminates the problems associated with conventional polishing and allows for larger specimens to be prepared with precision. Argon ion mills consists of a specimen chamber with a turbo pump vacuum system, an optical microscope for specimen positioning, and controls for the vacuum system and stationary ion beam. The specimen stage in the chamber features a holder and masking plate. To produce a polished surface, the specimen is placed in the holder, and the region of the sample to be cross sectioned is selected under the optical microscope (Fig. 2). The masking plate is placed across the selected region. After evacuating the specimen chamber, the region is milled with a broad argon ion beam. During milling, the specimen stage can be automatically rocked ± 30° to prevent beam striations and ensure uniform etching of materials with different hardness, which prevents the soft portions from being cut faster than the

hard portions (Erdman et al., 2006). As it is not a mechanical polishing method, abrasives are never embedded in the polished surface, and samples that are sensitive to heat can be milled without distortion.

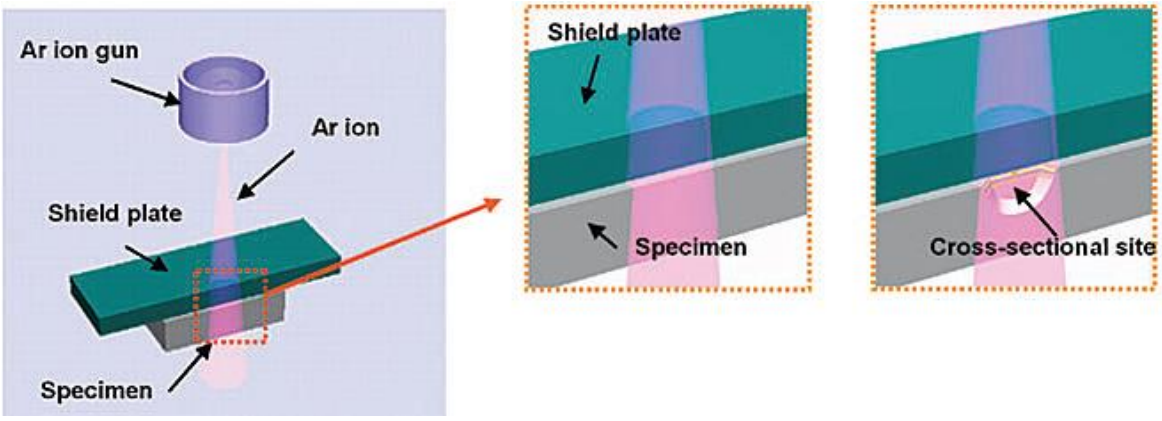

Figure 4. General overview of the argon ion milling process and the milling components (modified from Erdman et al., 2006).

III. 2 Sample identification

The majority of samples chosen for CT analysis were picked because they contain distinctive features identified during core description and thin section analysis. Those areas included physical sedimentary structures, structural deformation, fossils, diagenetic structures, and sections with differences in mineralogical composition. These samples were chosen in order to assemble a spectrum of observations and to determine the efficacy of the CT scanner for imaging and extracting data that cannot be obtained readily using other methods. While most samples were chosen this way, two were picked based on size in order to determine the effects that sample size has on the contrast and voxel resolution of a scan. One sample was also picked in an effort to image microporosity.

Observations of rock features and fabric from CT analysis were used to identify samples for microfabric investigation via SEM/EDS. The areas that were studied in further detail were

sections of the rock where mineral composition and morphology could not be accurately determined and also areas where pore identification could not be performed with confidence due to partial-volume effects.

III. 3 Preparation techniques

The maximum sample volume that can be imaged using the Xradia VersaXRM 410 CT is 5 cm in height, 4 cm wide and 4 cm thick. Thus, while whole H-gauge (~10 cm diameter) core samples can be scanned, only a portion of the core can be scanned at one time. This requires use of the maximum x-ray energy condition (150 kV) and results in a scan with low contrast due to the high x-ray energy and loss of x-rays that attenuate before they reach the volume of sample to be imaged. Therefore, the majority of the core samples scanned were sawn to a smaller sample size in order to acquire the best possible results.

The most efficient geometry to scan is a cylinder because the full scan field for CT is a cylindrical. Accordingly, cylindrical samples were first attempted to be made by using 3/8 inch and 1 inch coring bits on a drill press. The vibrations from the bit and the fissile nature of the shale caused the rock to break, and so high quality samples could not be retrieved reliably using conventional core plugging techniques. Subsequent attempts at creating smaller samples involved the use of a MK 101 water-cooled rock saw with a diamond impregnated blade. While some of the fissile samples were challenging to cut, the rock saw worked well for the majority of the samples. Size of the cut samples was tailored to what was desired to be imaged.

Samples for CT analysis were mounted in four different ways. The most common mounting method employed plumber's putty to fix the sample to the sample stage. A few samples were mounted using a clamp holder. Due to its large size, the butt slab of a core that was scanned was secured to the sample stage using electrical tape to ensure its stability throughout the scan. Lastly, the smallest sample scanned, measuring 0.3 mm in height, 0.2 mm wide and 0.2

mm thick, was mounted to a sharpened piece of 0.3 mm wide graphite pencil lead. Pencil lead was chosen because of its relatively low density compared to that of a rock in order to reduce beam hardening artifacts. First, the lead was sharpened to a fine point by rubbing and rotating it against a piece of paper. Another piece of dull pencil lead was then dipped into a small droplet of 5-minute epoxy and placed under a binocular microscope. With the epoxy-dipped lead in the field of view, the sharpened piece of lead was then carefully moved towards the epoxy until they barely came in contact. This was done to ensure that only a very small amount of epoxy was on the end of the sharpened pencil lead. Next, the point of the lead was pushed lightly against the sample so that it would adhere to the lead. After drying, the lead was placed into a miniature pin vise mount.

Both freshly broken surface and argon ion milled samples were inspected and analyzed using SEM/EDS. Freshly broken surface samples were prepared using the technique detailed in the *Argillaceous Rock Atlas* by O'Brien and Slatt (1990) (Fig. 5). First, a narrow groove was cut completely around the rock with a diamond impregnated saw blade. Roughly 3 mm of sample was left uncut. Next, a freshly broken surface was produced by placing pliers or fingers on both sides of the sample and applying pressure until it broke along the grooved cut. Any fine dust that was left on the surface of the sample was blown free. The broken samples were then mounted to circular stands using double-sided adhesive tape.

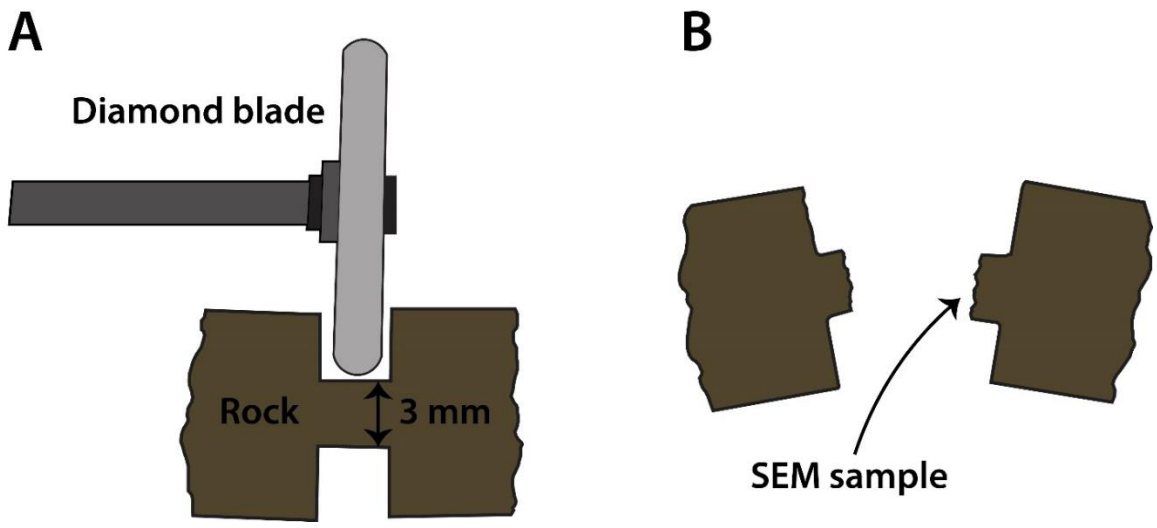

Figure 5. Overview of freshly broken surface sample preparation. (A) Using a diamond blade to cut a narrow groove around the rock. (B) Applying pressure on the sample to create a freshly broken surface. (modified from O'Brien and Slatt, 1990).

Samples for ion milling were cut to a dimension of 7 mm in height, 10 mm wide and 2 mm thick using a SYJ-160 low speed diamond saw with a digital micrometer head and edge sintered diamond blade. Samples were then marked with a fine point marker and pencil lead, with the boundary between the two marks serving as an indicator for the area to be milled. Samples were fixed to bronze blocks using silver paint so they could be mounted in the mill. Samples were milled at a range of 5 - 7 kV for 6 - 8 hours each, depending on their hardness (i.e. the harder samples were milled at a higher voltage and for longer periods of time). After milling, samples were removed from the bronze blocks and attached to circular SEM sample stands, measuring 12 mm in diameter, using silver paint. Once mounted, both freshly broken surface and ion milled samples were sputter coated using a Balzers Union MED 010 coater. Applying a thin coat of metal serves to concentrate the electron beam and allows for a clearer image to be obtained. Samples were coated with a gold-palladium (Au-Pt) mixture. While coating the samples with carbon would have allowed for quantitative EDS maps to be made, it would have resulted in a loss of image quality when compared to the Au-Pt coating. Au-Pt was chosen over

carbon coating because the goal of the SEM work was to make qualitative microfabric observations rather than quantitative chemical analyses. Even though EDS maps were not possible with the Au-Pt coated samples, the coating still allowed for EDS spot analysis, which enabled rapid identification of mineral constituents.

III. 4 X-Imaging techniques

Performing a CT scan was a five-step process: 1) sample directory and recipe, 2) load, 3) scout, 4) scan and 5) run. Step 1 was setting up the sample's directory and data folder and to initiate the creation of a recipe. A recipe is essentially the sequence of spatial and scanning, parameters applied to a given sample. Recipes can be saved for future use to expedite the scanning process for samples with similar dimensions and composition. Step 2 was to load the sample and use the visual light camera to center it along its x, y and z axes at 0° and 90° positions. Step 3 is scouting the sample to find the desired region of interest and determine imaging parameters using x-ray images. The scout phase consists of finding and centering the region at low magnification and then fine-tuning the region of interest if a high magnification is used. After centering, the detector and x-ray source positions are set while keeping the sample in the frame of reference in order to obtain maximum resolution. Next, the proper x-ray filter and kV are selected to ensure a maximum contrast is achieved. Lastly, the acquisition time is determined by altering the x-ray exposure time until the proper intensity value is achieved. Step 4 is setting the 3D scan parameters for the recipe. During this step, the number of projections (i.e. number of radiographs) to be taken is chosen. Higher quality tomographs are acquired by increasing the number of projections. This is also the time to set up a variable exposure time if it is needed. Samples that are thin and wide produce non-uniform x-ray attenuations across a typical range of rotation angles. At long view angles, low x-ray transmission can introduce noise to reconstruction and potentially lead to artifacts. Variable exposure is used to vary the exposure time between scan angles for high aspect ratio samples and achieve more uniform x-ray counts

throughout scan angles. Step 5 is to run the recipe and acquire a scan file. Before running the main recipe, it is good practice to copy the main recipe and create a warm-up recipe. The warm-up recipe is ordered before the main scan and its scan time is trimmed down to 30 minutes by lowering the number of projections. The warm-up is run before the main scan in order to calibrate the instrument.

The Au-Pt coated SEM samples were imaged using a voltage range of 20 – 30 kV, a spot size of 2.5 – 3.5 μm and a working distance of 9 – 11 mm. Samples were first observed in their entirety at a low magnification in order to locate areas for higher magnification observation (Fig. 6). For the ion milled samples, observing at low magnification allowed for identifying and characterizing the area of sample that had been milled. All features were imaged perpendicular to bedding and included mineral grains, crystals, organic matter, pores, and fossils. All mineral identifications were based on morphology and EDS spot analysis.

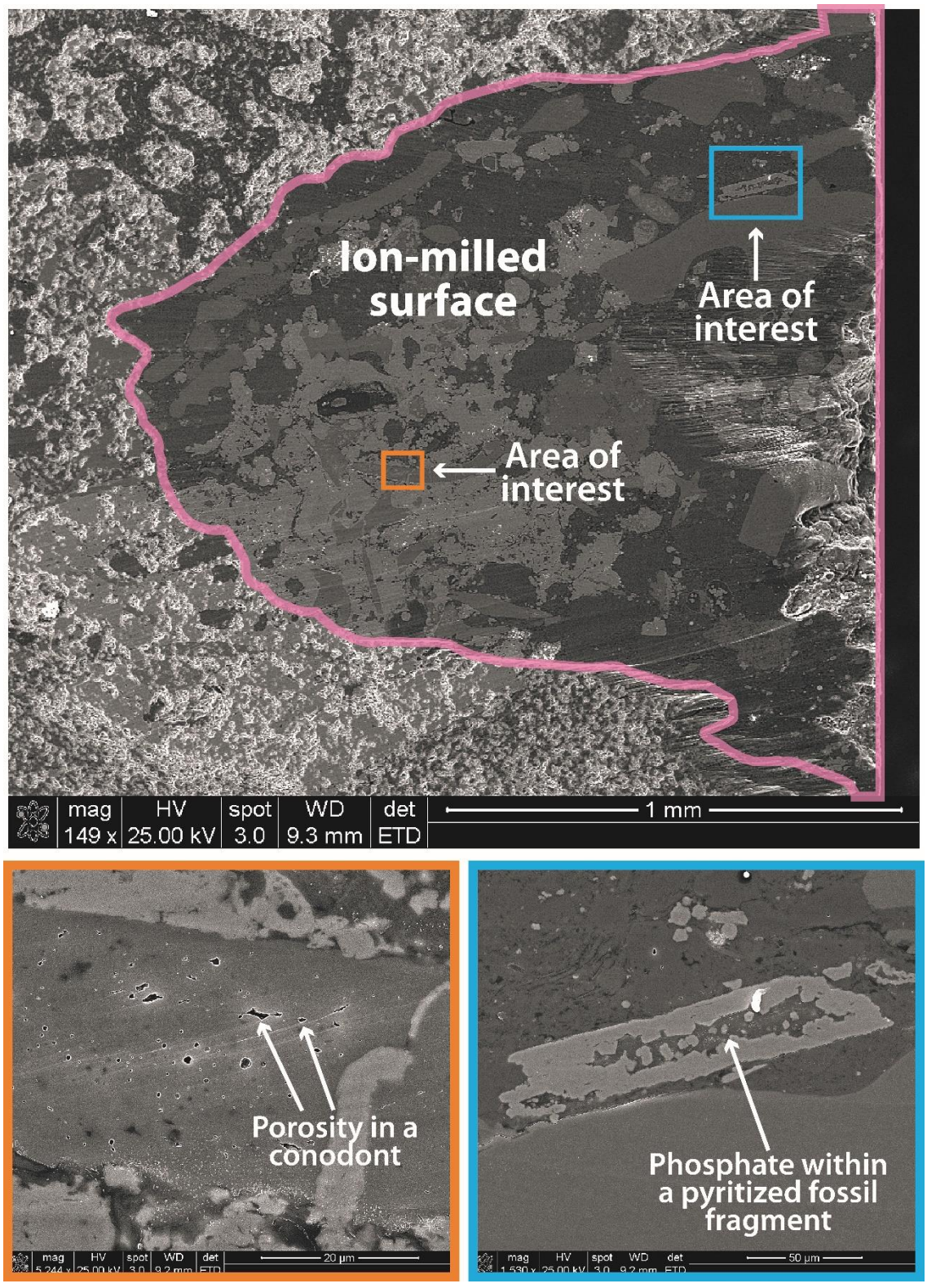

Figure 6. SEM imaging strategy. Samples are viewed in their entirety at a low magnification to identify areas for higher magnification imaging.

III. 5 Image processing

After each CT scan was finished, XMReconstructor software was used to reconstruct the scans by stitching together the individual radiographs and generating CT slices. The slices for each scan were generated along the XY plane of the sample and had a thickness of one voxel, with the size of the voxel depending on the resolution of the scan. The number of slices in each scan ranged from 950 to 1,004. Reconstructions were performed by manually entering inputs that corrected for sample shifting or beam hardening. Reconstructed scans were used to gather both qualitative and quantitative data using two different software packages. Qualitatively, XM3DViewer was used to view scanned samples in two and three dimensions and to produce images. The types of images that were generated were 2D slices and 3D volumes that could be cropped and density filtered. The software package enables stacking of a contiguous set of CT slices to create a 3D tomograph of a sample and then allows for lower density constituents to be stripped from the rendering using a density filter. The density filter is a histogram of the gray values in a scan that can be segmented. Because the gray values for each scan are assigned on a relative scale based on the intensity data received by the detector, there is no way to know the precise density of what is imaged in every voxel. This is because the x-ray intensity received by the detector is affected by all density variations along the x-ray path rather than the absolute density of any specific object. The density filter coloring options (Fig. 7) were used to highlight sedimentary structures, fossils, minerals and fractures, but this, too, must be displayed on a relative intensity scale rather than an absolute density scale. Quantitatively, an image analysis software called ImageJ was used to calculate volumetric percentages of mineral constituents and fracture porosity by segmenting gray values using hand-selected histogram cutoffs.

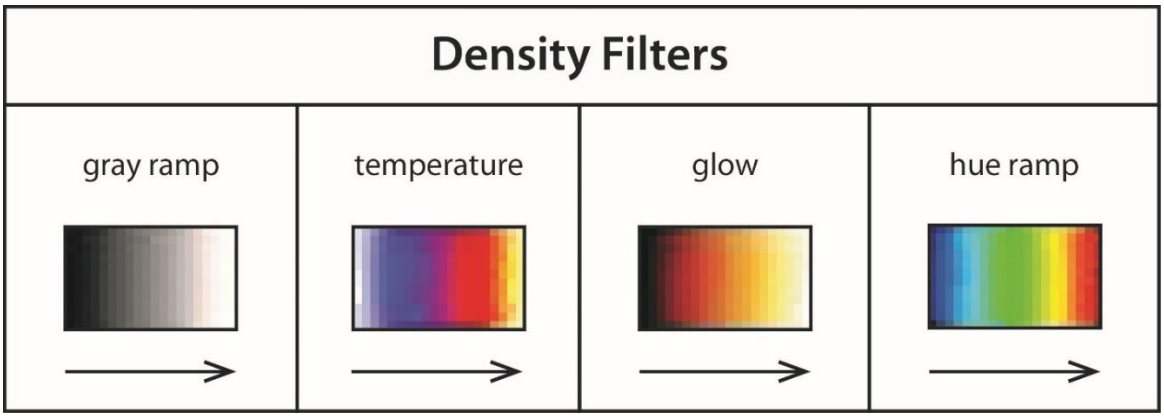

Figure 7. Density filter color schemes used to generate 3D images. Arrows indicate increasing density as received at the x-ray detector.

Image processing for ETD micrographs obtained from the SEM was minimal. Adobe Photoshop CC 2014 and Apple Aperture software were used to sharpen micrographs and also alter brightness and contrast values in order to highlight different features. Embedded scale bars from micrograph labels were used to measure features of interest.

CHAPTER IV

RESULTS

This section presents major results of CT and SEM/EDS analysis of cores used in this study listed in stratigraphic order, starting from the oldest. The discussion of each core begins with a brief summary of the lithology and paleoenvironment. The discussion then shifts to the results and basic interpretation of the tomographs and micrographs acquired from each sample. Sample photography was used as a visual aid. Although numerous samples were analyzed, only the samples with the most demonstrative results are discussed herein (Table 1).

IV. 1 Conasauga Formation; Dawson 33-9 no. 2A core

The Conasauga Formation in Alabama is mainly of Upper Cambrian age and has been explored for natural gas in the Appalachian Thrust Belt. It is characterized as a shoaling-upward succession in which an array of inner ramp carbonate facies passes laterally into interbedded shale, limestone, and dolostone that was deposited in an intrashelf basin (Astini et al., 2000; Thomas et al., 2000; Pashin, 2008; Pashin et al., 2012). During the late Paleozoic Alleghanian Orogeny, the shale was thrust into giant antiformal stacks, or ductile duplexes, that are up to 14,000 feet thick and occur in a belt 120 miles long and 30 miles wide (Thomas, 2001; Pashin et al., 2012).

The Dawson 38-9 #2A core comes from the Big Canoe Creek Field in St. Clair County, which is the first shale gas field established in Alabama. One sample of the shale from a depth of 7,565.7 ft. was CT scanned. The sample is from a weakly deformed block in the Conasauga shale mass and is from a laminated shale containing sand- to granule-size pyrite nodules; a nodule approximately 5 mm in height is preserved in the upper part of the sample (Fig. 8). The tomograph of the sample reveals an abundance of information about the nodule. The interior of the nodule is less dense than any of the surrounding material, suggesting that it is contains a significant amount of clay and microporosity. This is a very peculiar observation considering thin section petrography on the nodules within the Conasauga shale facies determined them to be peloidal dolomicrite (Pashin et al., 2012). There also is a horizontal network of microburrows within the nodule that appear to be filled with denser carbonate material. Also, inside the nodule are some pyrite bodies that image very brightly. The nodule extends into a carbonate lamina, which is a feature that is commonly observed in the Conasauga shale facies (Pashin et al., 2012). Dispersed throughout the rest of the sample are a numerous clay laminae, bed-parallel fracture partings and bright particles that are not evident in the photograph. An SEM image suggests the bright particles are either likely pyrite framboids (Fig. 9).

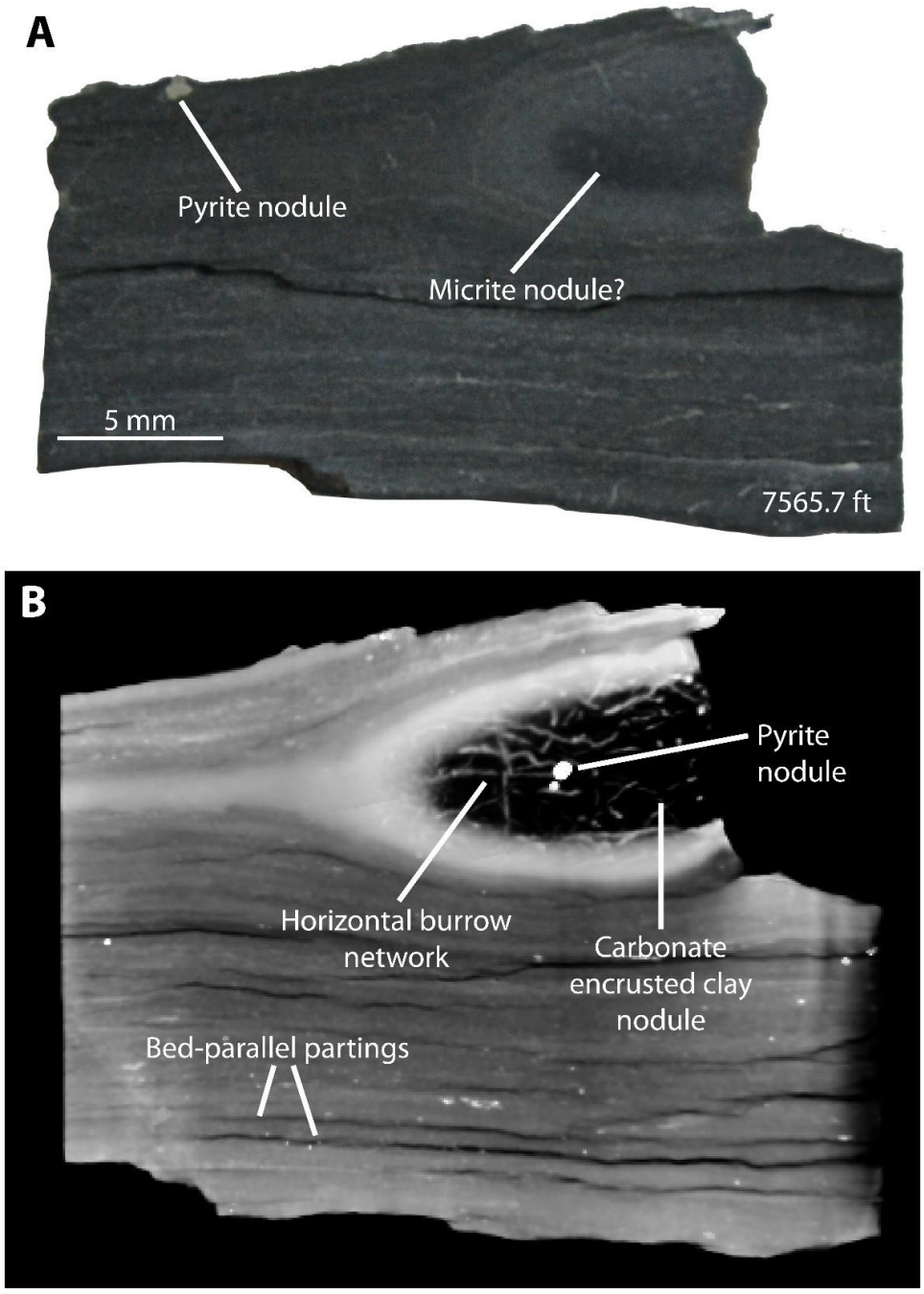

Figure 8. Photograph and corresponding tomograph of Dawson 38-9 #2A core, 7,565.7 ft. (A) Black shale containing a pyrite nodule and what appears to be a micrite nodule encrusted in carbonate. (B) Black shale with a carbonated encrusted low-density nodule containing horizontal carbonate-filled burrows and pyrite nodules. Bed-parallel partings, demonstrating the high fissility of the shale, and indiscernible bright grains are present throughout the sample.

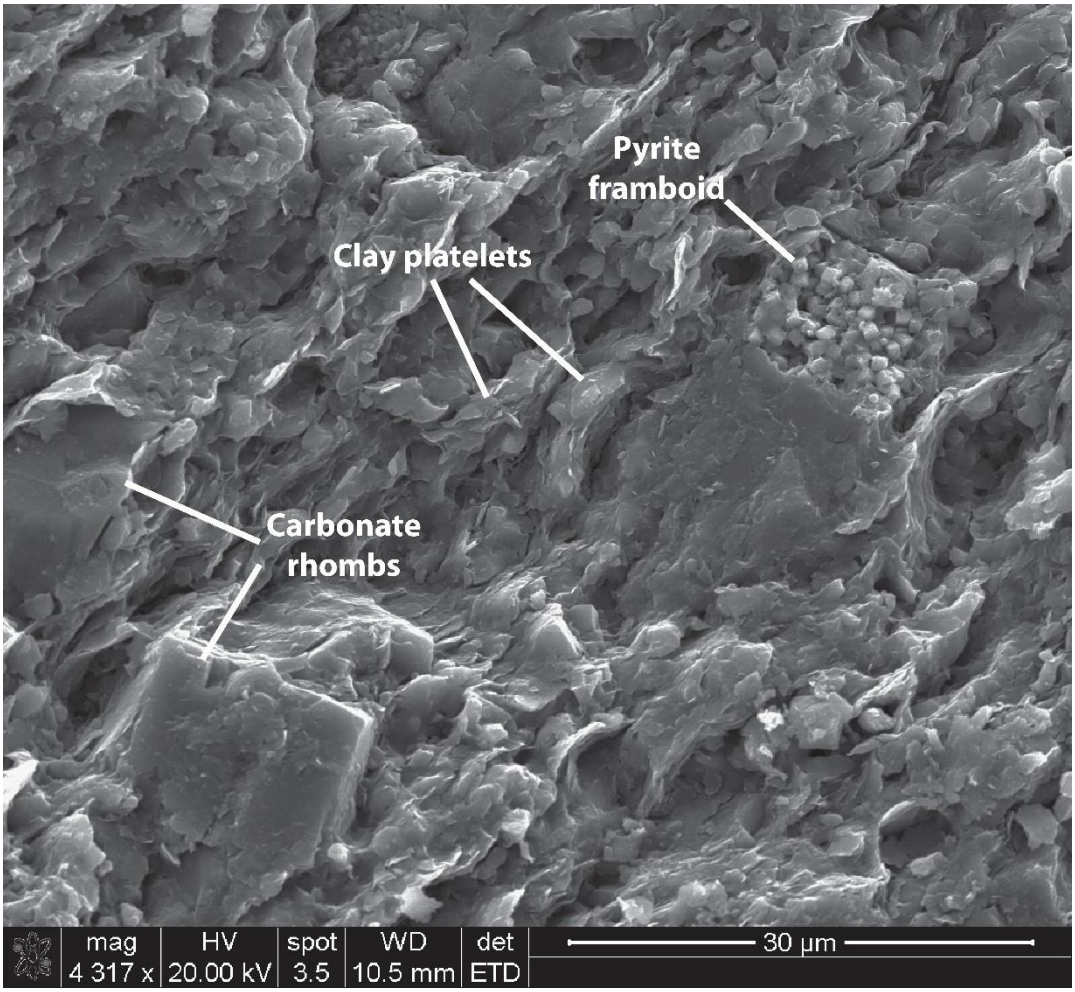

Figure 9. SEM ETD image of microfabric from a freshly broken sample of Conasauga Shale in the Dawson 33–9 #2A core, 7,565.7 ft. A pyrite framboid and carbonate rhombs are preserved in a matrix of platy illite with poorly aligned and folded clay platelets.

IV. 2 Chattanooga Shale

The Chattanooga Shale in the Black Warrior Basin and Appalachian Basin is of Late Devonian age and was deposited as an organic-rich cratonic shelf facies (Rheams and Neathery, 1988; Pashin et al., 2010). It was deposited in dysoxic to anoxic subtidal environments in a density stratified water column and is an important petroleum source rock and unconventional reservoir target in the southeastern United States (Pashin, 2008). Five samples from the

Chattanooga Shale in the Lamb 1-3 #1 and CNX 517-29 cores were photographed and CT scanned, and additional data from the Lamb core are available in Pashin et al. (2011).

IV. 2.1 Lamb 1-3 no. 1 core

The Lamb 1-3 no. 1 well is in Greene County, Alabama in the Black Warrior Basin. Four samples at depths of 9,167.5 ft., 9,173.5 ft., 9,180 ft. and 9,192.5 ft. were taken from the Lamb 1-3 #1 core. The sample from 9,167.5 ft. is a black shale with alternating novaculitic chert, clay and pyrite laminae (Fig. 10). This was the largest sample scanned, and the purpose of scanning it was to determine the efficacy of scanning butt slab core samples on the XRadia VersaXRM 410 system that was used. As previously mentioned, while the machine is equipped to physically accommodate large samples, only a small volume (5 cm in height, 4 cm wide and 4 cm thick) within a sample can be imaged.

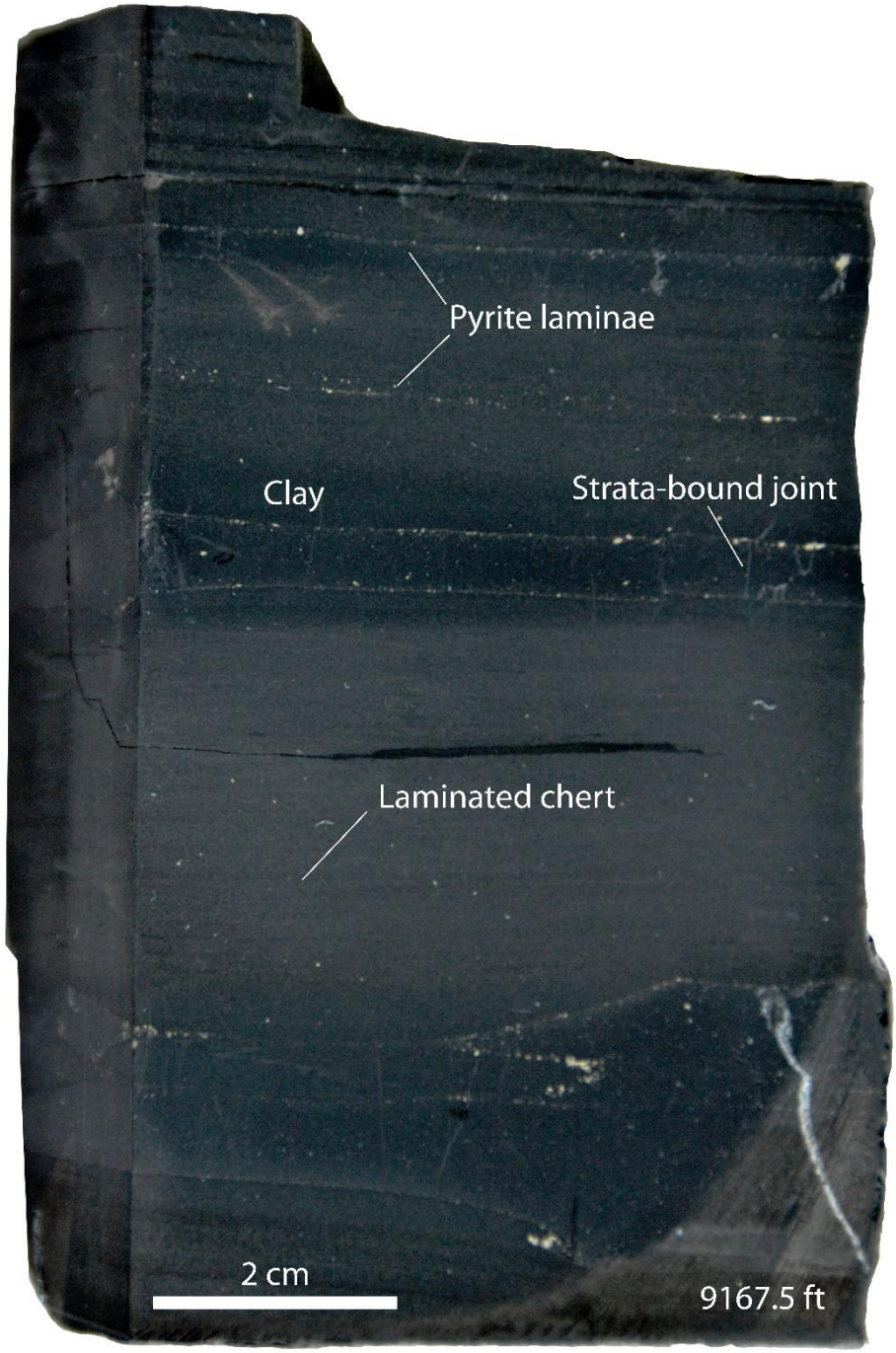

Figure 10. Photograph of black shale with alternating chert, clay and pyrite laminae, Lamb 1-3 #1 core, 9,167.5 ft. Note strata-bound joints are present within the chert laminae.

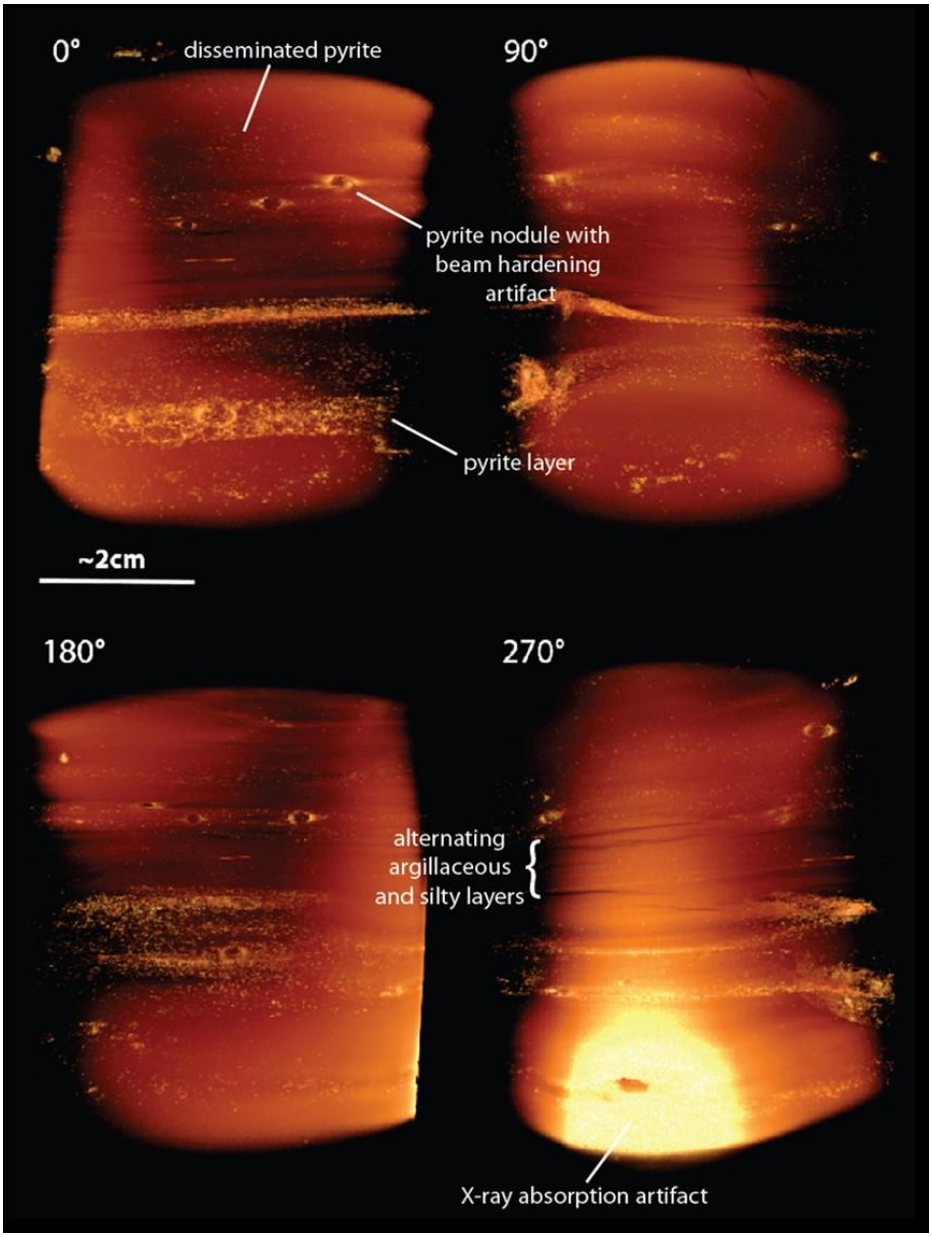

Figure 11. Glow density filtered tomograph presented at four different angles, Lamb 1-3 #1 core, 9,167.5 ft. At 0°, pyrite can be seen in several different forms; disseminated grains, nodules and laminae. The nodules have significant beam hardening artifacts, as indicated by their edges being much brighter than their centers. At 270°, there is another beam hardening artifact where the edge of the sample absorbed a large amount of x-rays, making it appear much brighter than the rest of the sample. Alternating argillaceous and silty layers can also be observed at this angle.

The resulting tomograph for the sample demonstrates the problems encountered when attempting to scan large core samples without cutting them to into smaller samples (Fig. 11). With the exception of the high density pyrite grains, which image as bright yellow, the information that can be gained from the tomograph is limited. The beam hardening artifacts present within the tomograph overshadow any useful data. The edges of the sample are much brighter than the center due to the loss of x-ray intensity where the beam penetrates the sample. Some of the pyrite nodules also have very bright edges due to this same x-ray artifact, which makes a body of uniform density appear as though it has a low density core.

The sample taken from 9,167.5 ft. is a black shale with subvertival mineralized fractures that is abundant with pyrite nodules (Fig. 12). Applying a glow density filter to a CT scan of the Lamb sample from 9,173.5 ft. reveals the internal geometry of the overlapping subvertical, mineralized fracture tips (Fig. 13). A thin section of a mineralized fracture from a nearby well contains quartz, calcite, and dolomite, which is typical of veins in the Chattanooga Shale in Alabama (Fig. 14) (Pashin et al., 2011). Pyrite framboids and crystals are imaged as bright bodies that are dispsersed throughout the sample, and several nodules are imaged near the base of the sample. The density filter also facilitates distinction of laminae rich in quartz silt from those rich in clay, which are not obvious in photographs and thin sections.

Figure 12. Photograph of black shale with subvertical mineralized fractures, Lamb 1-3 #1 core, 9,173.5 ft.

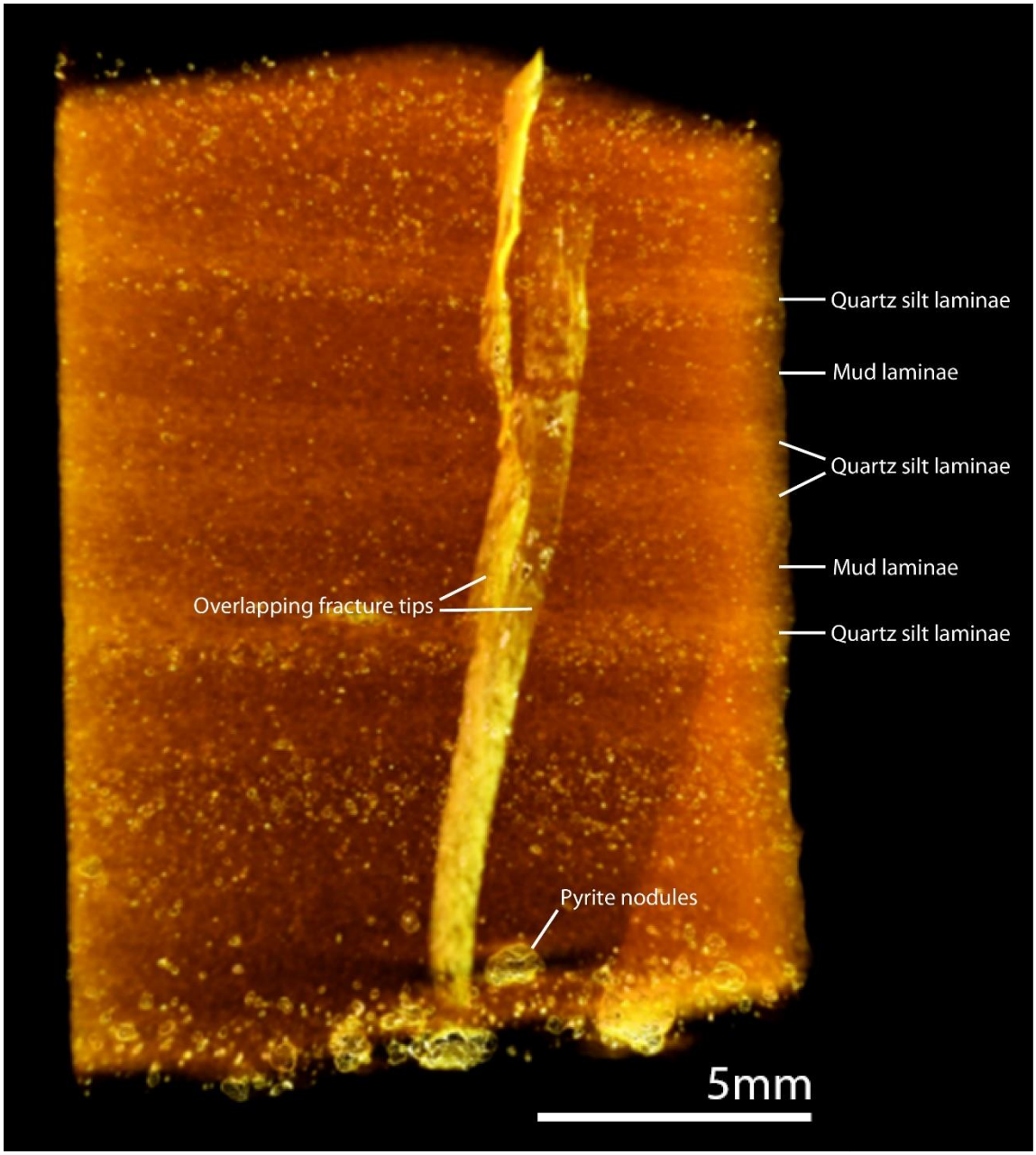

Figure 13. Glow density filtered tomograph of overlapping mineralized fracture tips, Lamb 1-3 #1 core, 9,173.5 ft. Note alternating mud and quartz silt laminae and pyrite nodules are prevalent throughout.

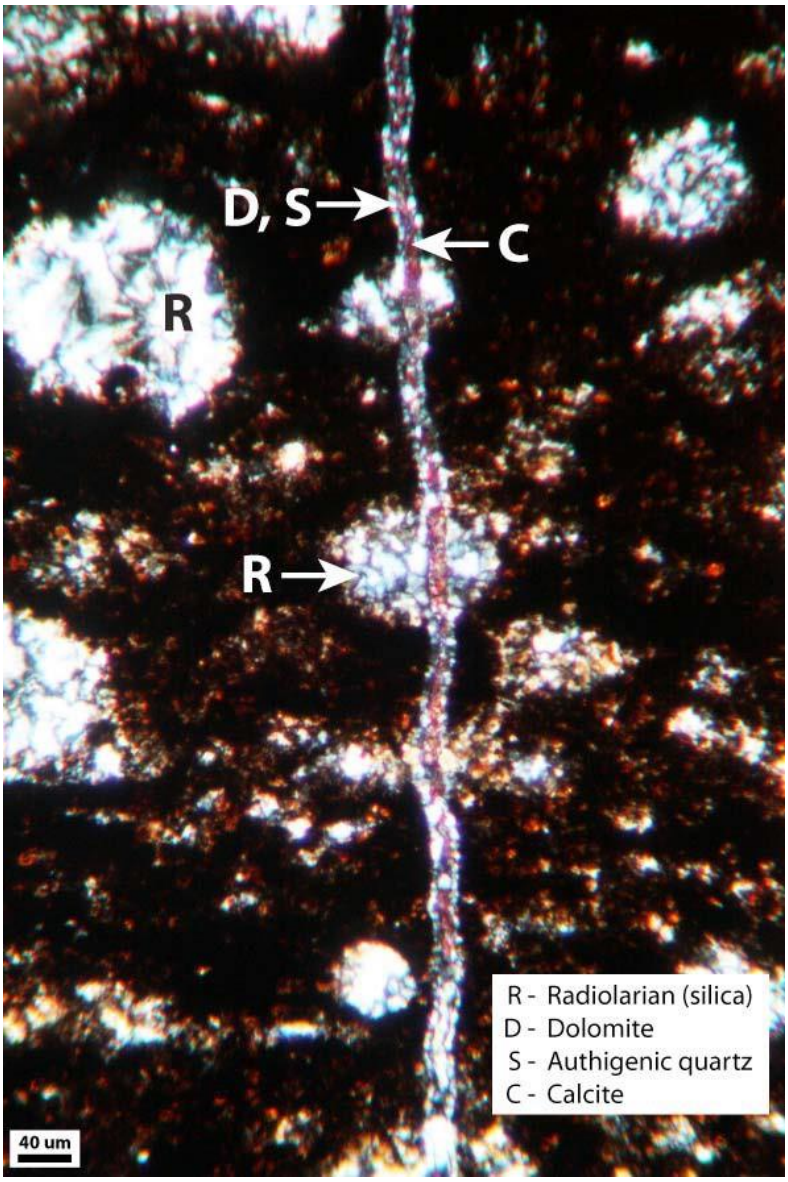

Figure 14. Thin section of a mineralized fracture cutting across rock fabric, including radiolarians in Chattanooga Shale (Weyerhaeuser 2-43-2402 well, Greene County, Alabama, 8,215.1 ft) (Pashin et al., 2011).

SEM secondary electron micrographs of samples from two different Chattanooga Shale wells in Greene County, Alabama show aspects of sulfide and clay morphology that cannot be determined by CT scanning alone (Fig. 15). Illite occurs in platy and lath forms, whereas pyrite forms nodules, euhedral crystals, dispersed euhedra, and as framboidal clusters.

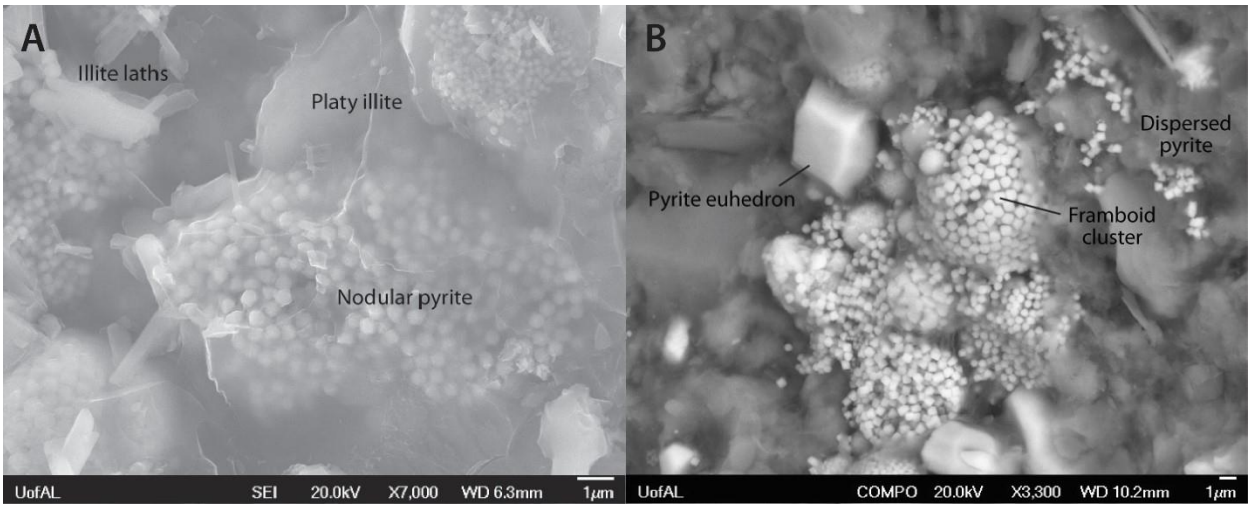

Figure 15. SEM secondary electron images of Chattanooga Shale samples from two different wells in Greene County, Alabama. (A) Illite forms and pyrite in a sample from core of the Bayne Etheridge 36-9 #1 well, 8,317 ft. (B) Diverse pyrite forms in a sample from core of the Weyerhaeuser 2-43-2402 well, 8,211.9 ft. (after Pashin et al., 2010, 2011).

The sample taken from 9,192.5 ft. is a cube of black shale with a rough surface and no discernible sedimentary structures (Fig. 16). It was the smallest Lamb core sample scanned, and the intent was to determine the effects that sample size has on the contrast and voxel resolution of a scan and to also see what features could be imaged near the resolution limits of the scanner. A volume inside the sample was scanned for 12.5 hours, resulting in a voxel resolution of 900 nm and a corresponding CT slice diameter of 900 μm (1,000 voxels wide) in the tomograph.

Figure 16. Photograph of an unpolished cube of black shale with no discernable sedimentary structures, Lamb 1-3 #1 well, 9,192.5 ft.

While porosity was not resolved, the tomograph did demonstrate the types of features that could be imaged close to the resolution limit of the instrument (Fig. 17). A microfracture and high-density mineral particles were easily recognized. Applying a density filter to the entire volume allowed for visualization of the individual mineral grains. Degree of crystallinity could not be determined, but the shapes of the grains could be observed, which include some distinctive angular elements. Applying the same density filter to a slice of the data also allowed for inspections of mineral grains, as well as the rock fabric. Grains ranged from round to angular and the fabric displayed moderate sorting. In addition, distinction of quartz and pyrite is probable because of their density differences. The yellow tinted, less dense grains are likely quartz, which has a specific gravity of 2.65 g/cm^3, as well as other silicate minerals with similar density, such as feldspar. The denser, bright white grains are likely pyrite because it has a much higher specific gravity of 5.01 g/cm^3. It is apparent from this scan that pyrite framboid cannot be distinguished. Identification of these mineral constituents was aided by x-ray diffraction (XRD) analysis. No carbonate minerals were recorded by the XRD analysis. The less dense, brown material between the grains is likely clay matrix and the darkest material observed in the last CT slice is possibly organic matter.

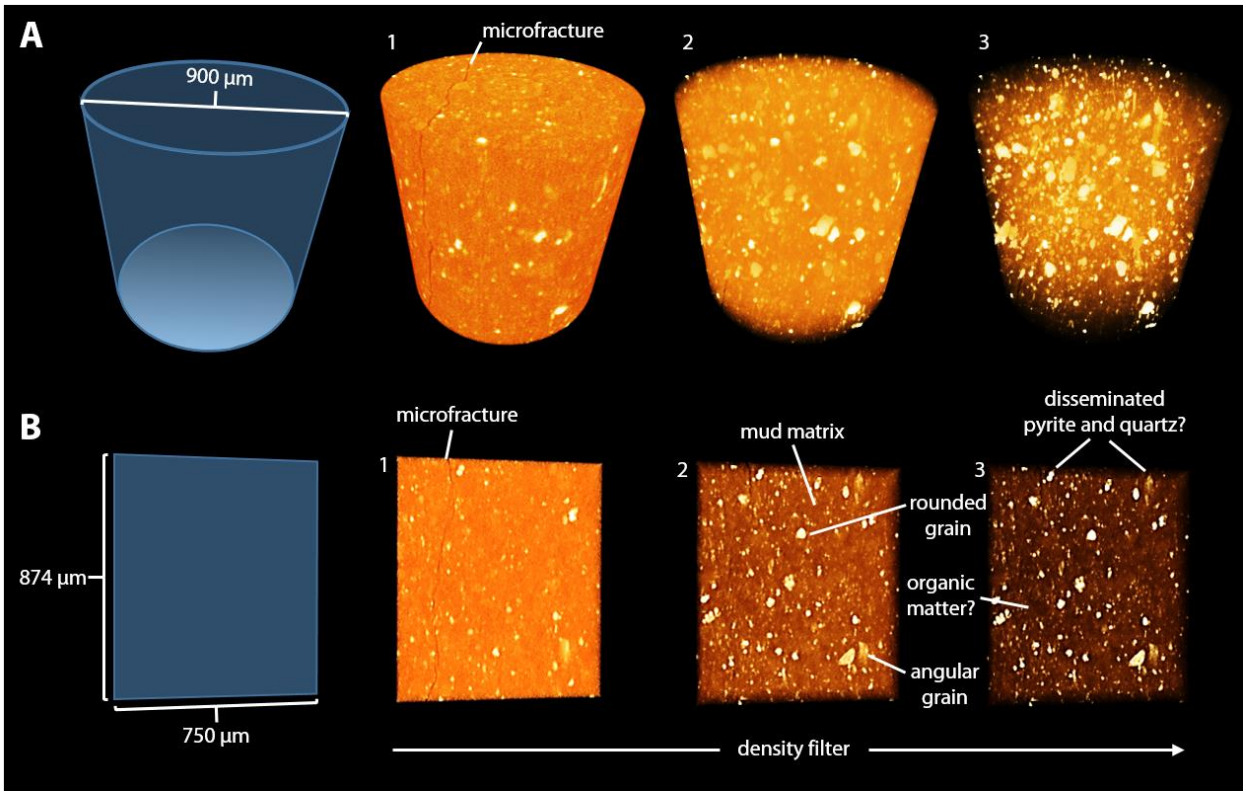

Figure 17. Glow density filtered full volume tomograph and CT slice, Lamb 1-3 #1 well, 9,192.5 ft. (A) Tomograph of the entire volume progressively filtered to isolate high density material. (B) CT slice progressively filtered to isolate high density material.

After successfully imaging fractures at a small scale in the Lamb sample taken from 9,192.5 ft, the larger and highly fractured Lamb sample from 9,180 ft was scanned to see how a varied assemblage of fractures, joints, and faults would image on a larger scale. The sample taken from 9,180 ft is black shale with a normally faulted novaculitic chert lamina containing strata-bound joints with pyrite, silica, and carbonate cement (Fig. 18).

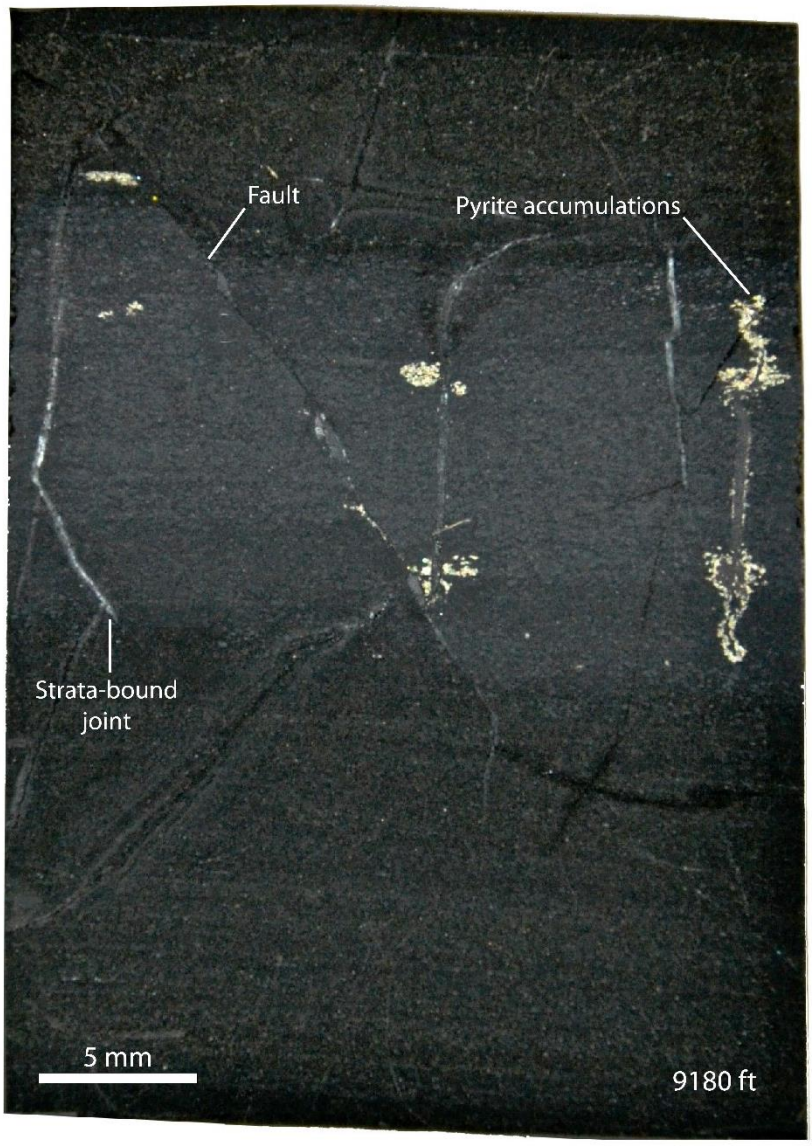

Figure 18. Photograph of black shale with a normal faulted novaculitic chert lamina with strata-bound jointing and pyrite accumulations, Lamb 1-3 #1 well, 9,180 ft. Note silica/carbonate and clay cement along some of the fractures.

The tomograph of the sample revealed a great deal about the internal fracture geometry and the variability of fracture and fault mineralization (Fig. 19). A normally faulted novaculitic chert lamina displays three different types of strata-bound joints. One of the joints offset by the fault is mineralized by silica. The other two joints are filled with silica and clay and have pyrite

accumulations in argillaceous strata on both ends. The CT scanner was able to not only image the mineralized joints that could be seen from the sample photograph, but also microfractures that were not readily visible. Siliceous cement was observed along the normal fault. Disseminated pyrite grains are also observable throughout the sample. While there is limited ability to determine mineralogy from the relative density data in the tomograph, mineral identification is aided by the sample photograph and thin section petrography.

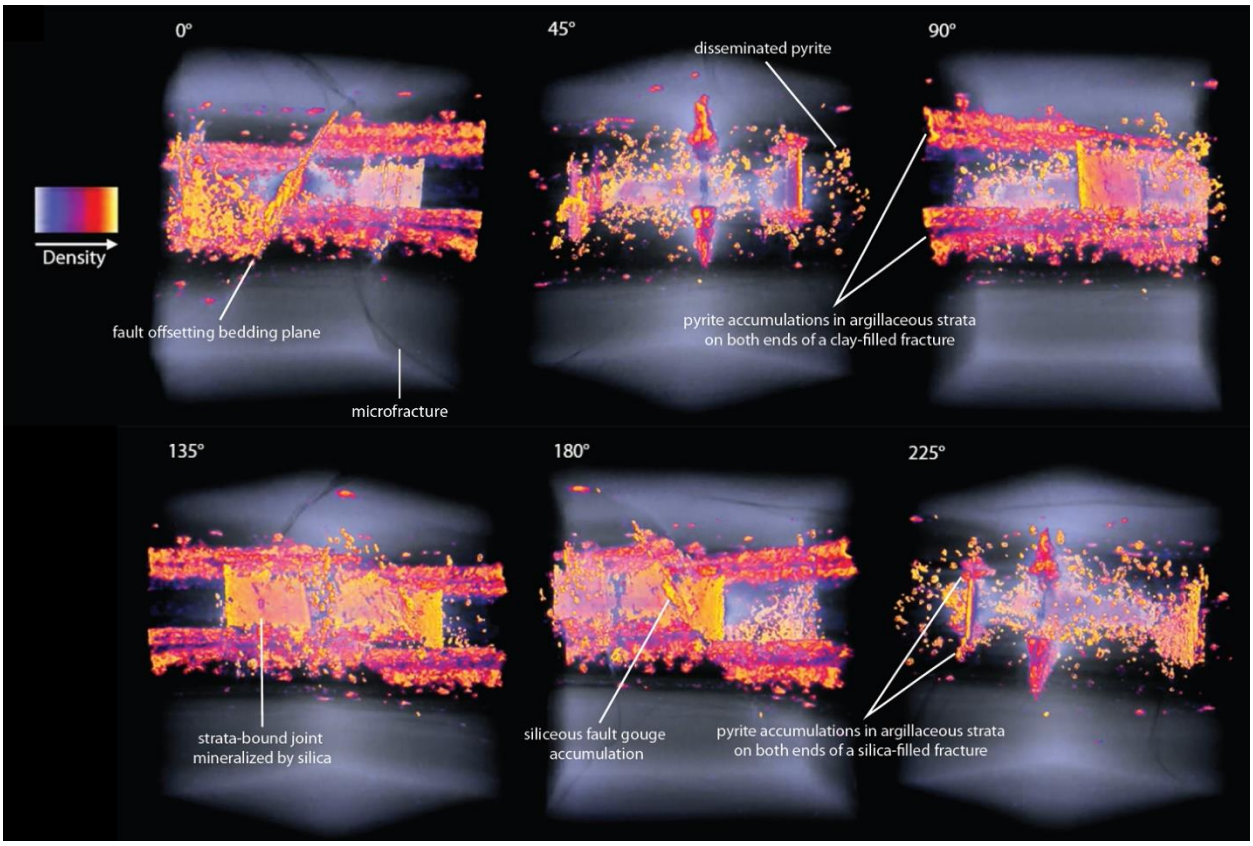

Figure 19. Temperature density filtered tomograph presented at six different angles, Lamb 1-3 #1 well, 9,180 ft. The features imaged include: a mineralized normal fault and fault gouge (180°), a strata-bound joint mineralized by silica and offset by the fault (135°), pyrite accumulations on both ends of a clay-filled joint offset by the fault (90°), a clay filled fracture and disseminated pyrite (45°).

IV. 2.2 CNX 517-29 core

The CNX 517-29 well is in Campbell County, Tennessee near the southern end of the Appalachian Basin. This well was recently used in an experiment to test the potential for CO_2-enhanced hydrocarbon recovery in shale (Louk, 2014). One sample at a depth of 3,200 ft was taken from the CNX 517-29 core. This sample is black shale with a pyrite lamina and alternating silty and muddy laminae (Fig. 20).

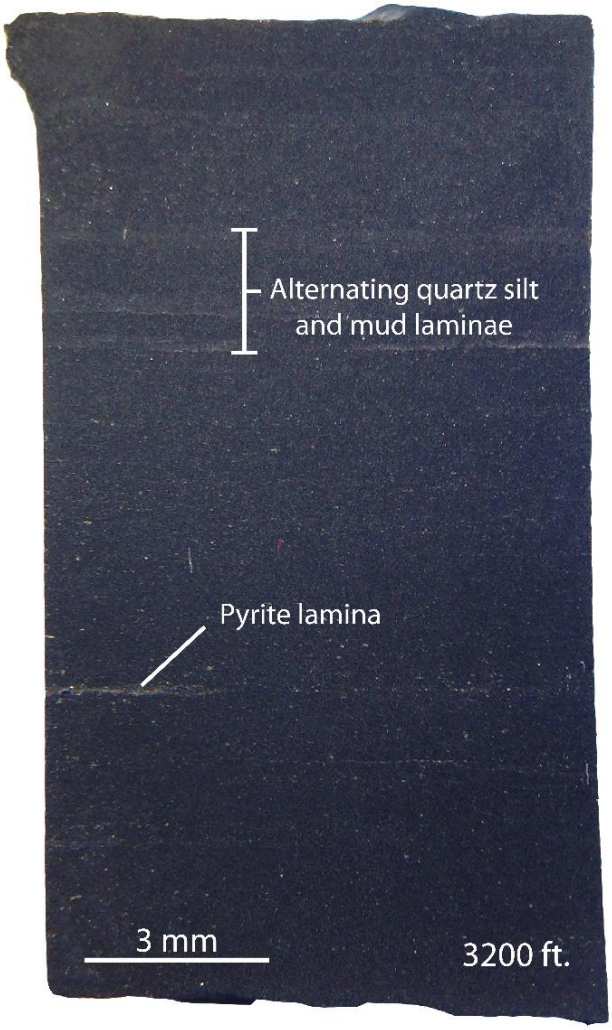

Figure 20. Photograph of black shale with pyrite lamina and alternating quartz silt and mud laminae, CNX 517-29 core, 3,200 ft.

The tomograph for the sample revealed a great deal of information that was not apparent in the hand sample or photograph (Fig. 21). In addition to imaging numerous quartz silt and mud laminae, many pyrite nodules alsowere imaged. However, the most surprising aspect of the tomograph is a dipping fracture plane that cuts across the sample. The fracture plane is defined by an irregular distribution of mineral cement, which arguably helps prop the fracture, thus facilitating fluid flow.

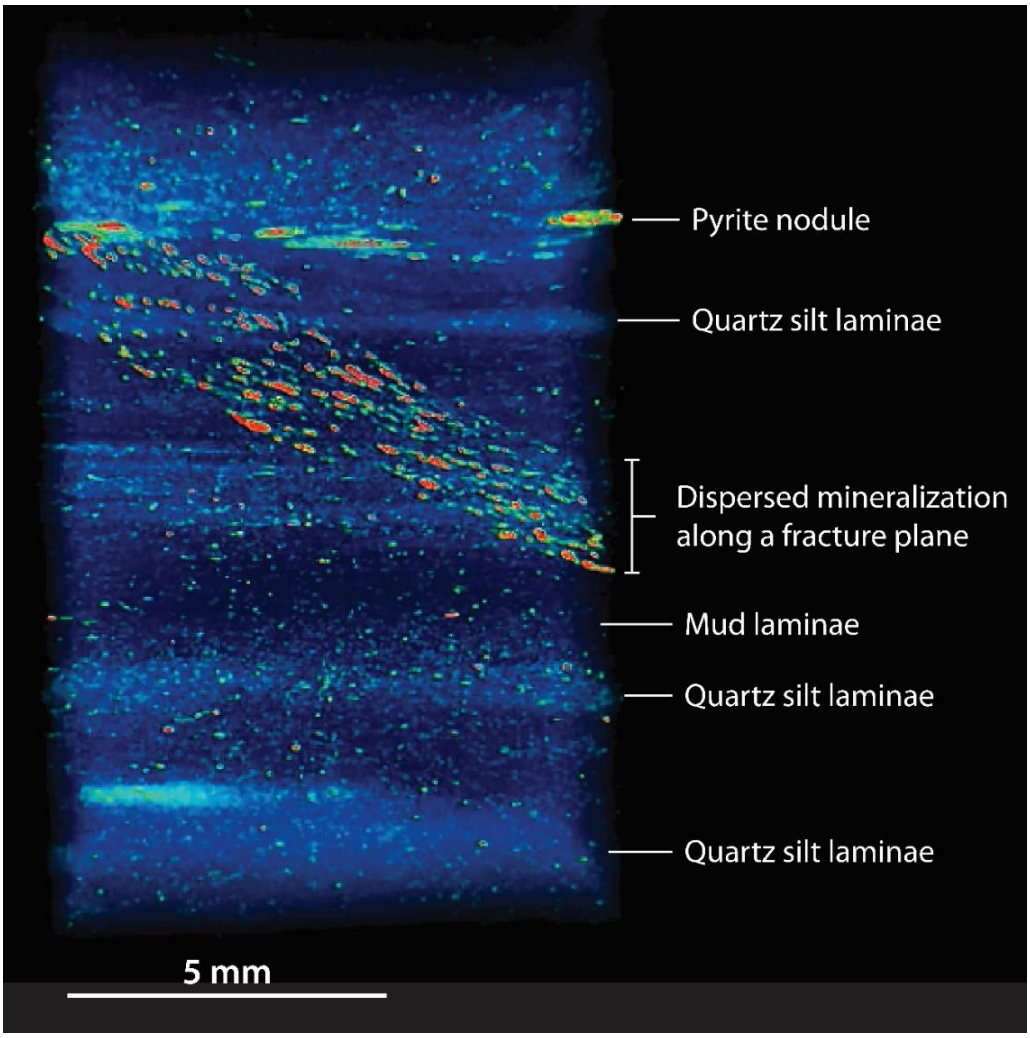

Figure 21. Hue ramp density filtered tomograph of Chattanooga Shale, CNX 517-29 core, 3,200 ft. Numerous pyrite nodules and quartz silt and mud laminae are imaged. A dipping fracture plane with patchy cement cross cuts the sample.

IV. 3 Woodford Shale

The Woodford Shale is of Devonian age and was deposited in the southern Midcontinent on a broad continental shelf bordering the Ouachita Embayment during the Kaskaskia cratonic onlap. The Woodford consists mainly of siliceous and argillaceous mudrock and is largely equivalent to the Chattanooga. The Woodford accumulated under dysoxic to anoxic conditions in an oxygen minimum zone, and biological activity related to oceanic upwelling was a major factor influencing the characteristics of the formation (Callner, 2014). The Woodford is a world-class petroleum source rock, as well as the principal unconventional resource target in Oklahoma. Seven samples from three Woodford Shale cores (Hall 2B, Anderson 12-1, and Poe 1-29) were scanned. The samples were chosen in order to display the variability of Woodford Shale features in the Arkoma and Anadarko basins.

IV. 3.1 Anderson 12 no. 1 core

The Anderson 12. No.1 core comes from Garfield County on the west side of the Nemaha uplift in North Bison Field (Fig. 1). The Anderson is discussed first because it typefies what geologists generally expect to see in Devonian shale. Three samples were taken from the Anderson 12. No.1 core (Table 1). The sample from 6,839.8 ft is black shale containing phosphate nodules coated with pyrite and calcite (Fig. 22).

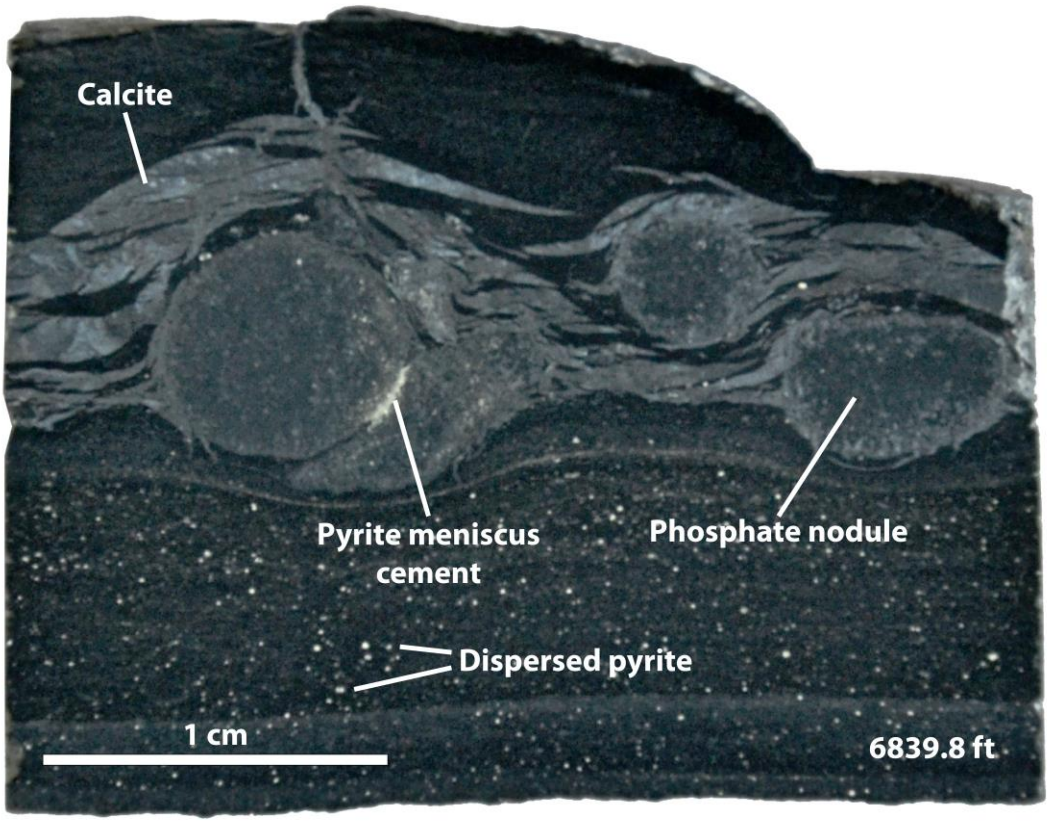

Figure 22. Photograph of black shale containing phosphate nodules coated with pyrite and calcite, Anderson 12 no. 1 core, 6,839.8 ft. Note dispersed pyrite in lower part of sample.

The interior of the sample was imaged by applying a gray ramp density filter to the x-ray tomograph (Fig. 23 A-C). By filtering out the lower density material, a large phosphate nodule was revealed in the interior of the sample. The tomograph was rotated to view the sample from above, and the density filter was changed to the temperature setting in order to illuminate the interior of the sample (Fig. 23 D). This view and filter allowed for closer examination of the phosphate nodules. From this view, the diameter of the phosphate nodules could be measured, and the spatial arrangement and contacts between the nodules could be evaluated. The only complete phosphate nodule imaged is the large one that was revealed by the density filter. It measures 13 mm in diameter and is in contact with two other nodules. Between the grain

contacts is a meniscus of pyrite cement, as indicated by the bright colors. A total of three meniscus pyrite bodies are revealed by the density filter. Small, high density pyrite bodies are also observed within the phosphate nodules and within the shale matrix. Nodule shapes range from tubular to spheroidal.

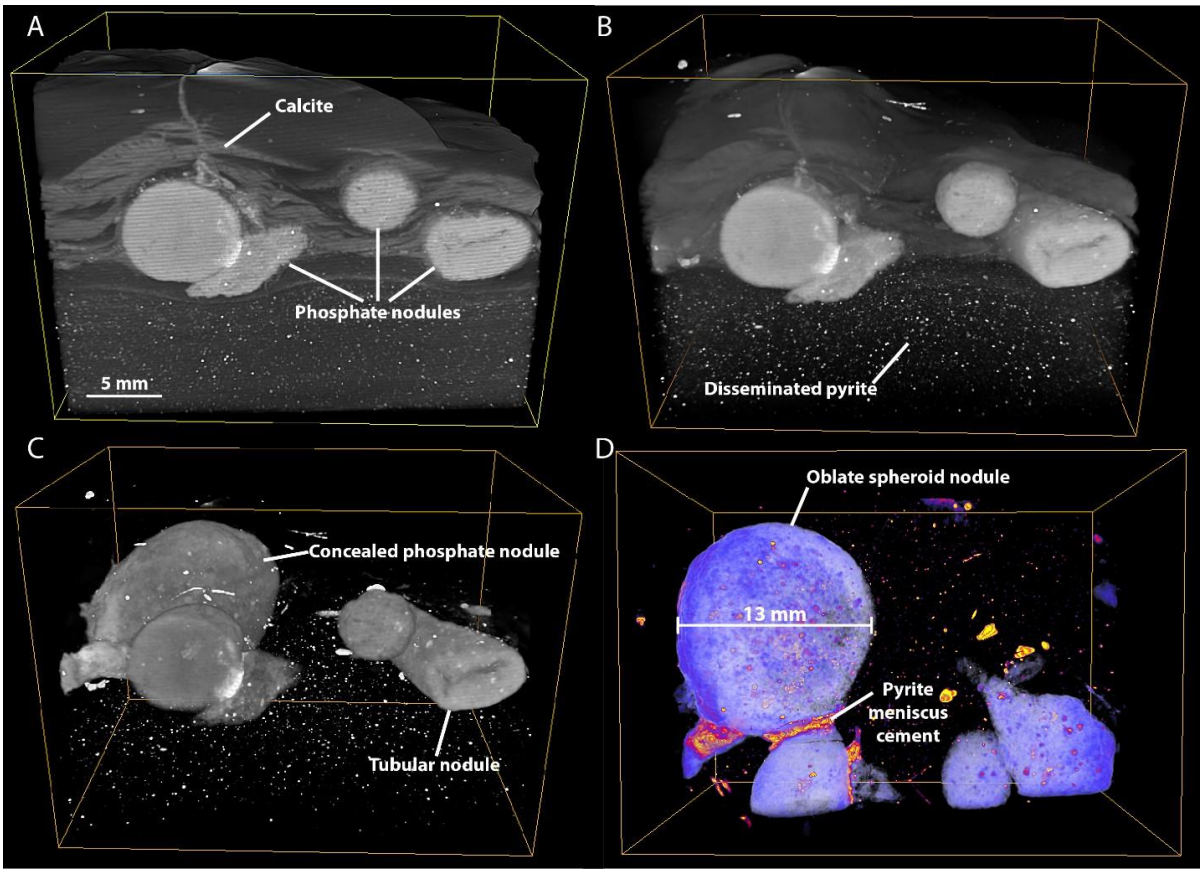

Figure 23. Gray ramp and temperature density filtered tomograph, Anderson 12 no. 1 core, 6,839.8 ft. (A-C) Gray ramp density filter applied to the tomograph filters the low density material and leaves the phosphates nodules and disseminated pyrite. The largest phosphate nodule in the sample is revealed, and the filter also allows for determining nodule shapes. (D) A temperature density filtered view of the sample down the XY plane allows for measuring nodule diameters and observations of meniscus cement and mineral constituents within the nodules.

For close inspection of the interiors of the phosphate nodules, a CT slice was examined (Fig. 24). The cross-sectional slice displays several different types of inclusions within the nodules. All nodules contain numerous micron-sized pores. The nodule to the far left seems to have nucleated around pyrite. The nodule to the far right of the slice appears to contain pyrite inclusions, as well as a low density lithoclast.

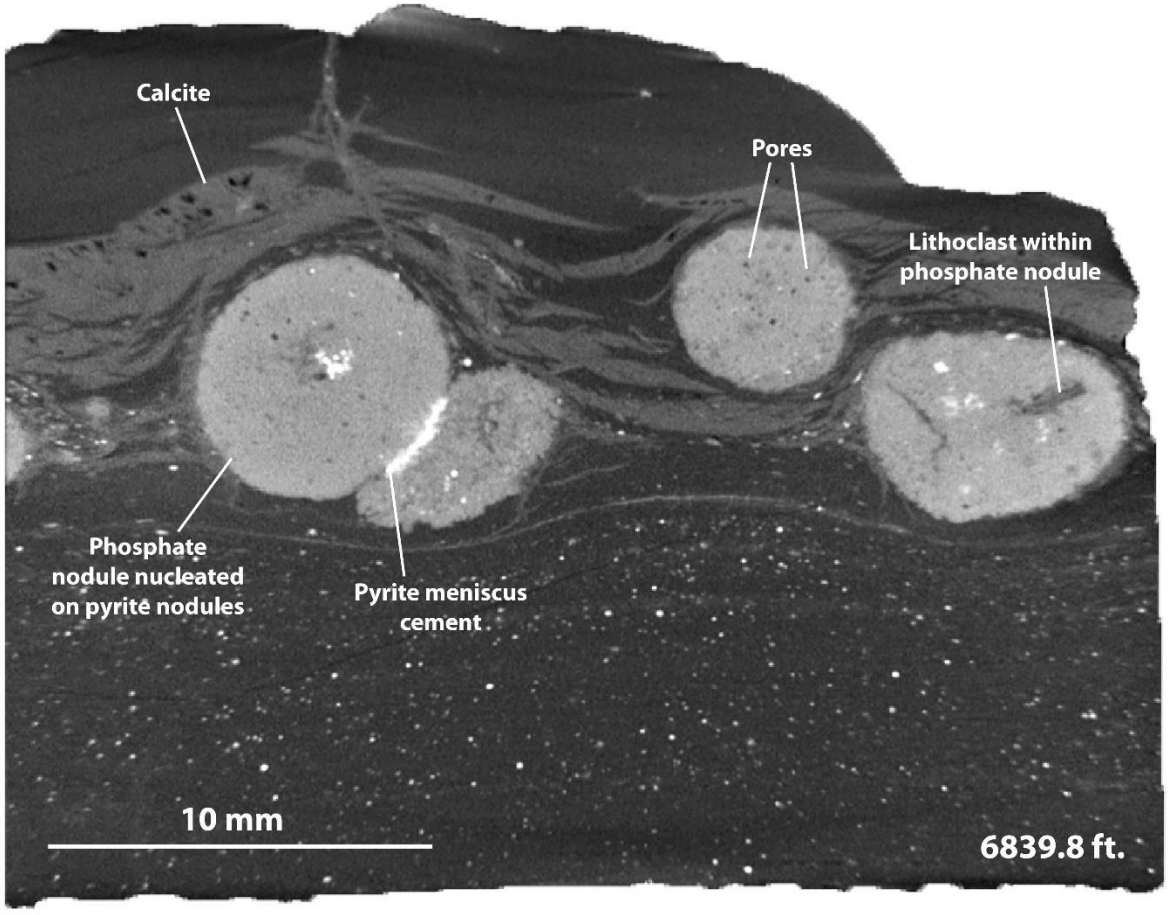

Figure 24. CT slice showing calcite coatings and inclusions in the interior of the phosphate nodules, Anderson 12 no. 1 core, 6,839.8 ft. Inclusions include pyrite grains and a lithoclast. There also appears to be micro-porosity within all of the nodules.

The sample from 6,843.6 ft. is a black shale exhibiting a variety of sulfide morphologies, including an unusual J-shaped form, nodules and an asymmetrical starved ripple made of

resedimented pyrite. (Fig. 25). The sample was CT scanned and a glow density filter was applied to the tomograph and viewed from four different angles (Fig. 26). The J-shaped platy body is visible in the first view at 0° and is connected to a much larger sulfide body that is not visible in the sample photograph. The figure shows small nodules above the rippled lamina and larger nodules below. The larger body below the lamina is also composed of bladed forms of sulfide. The bladed morphology in the large nodular mass is indicative of marcasite.

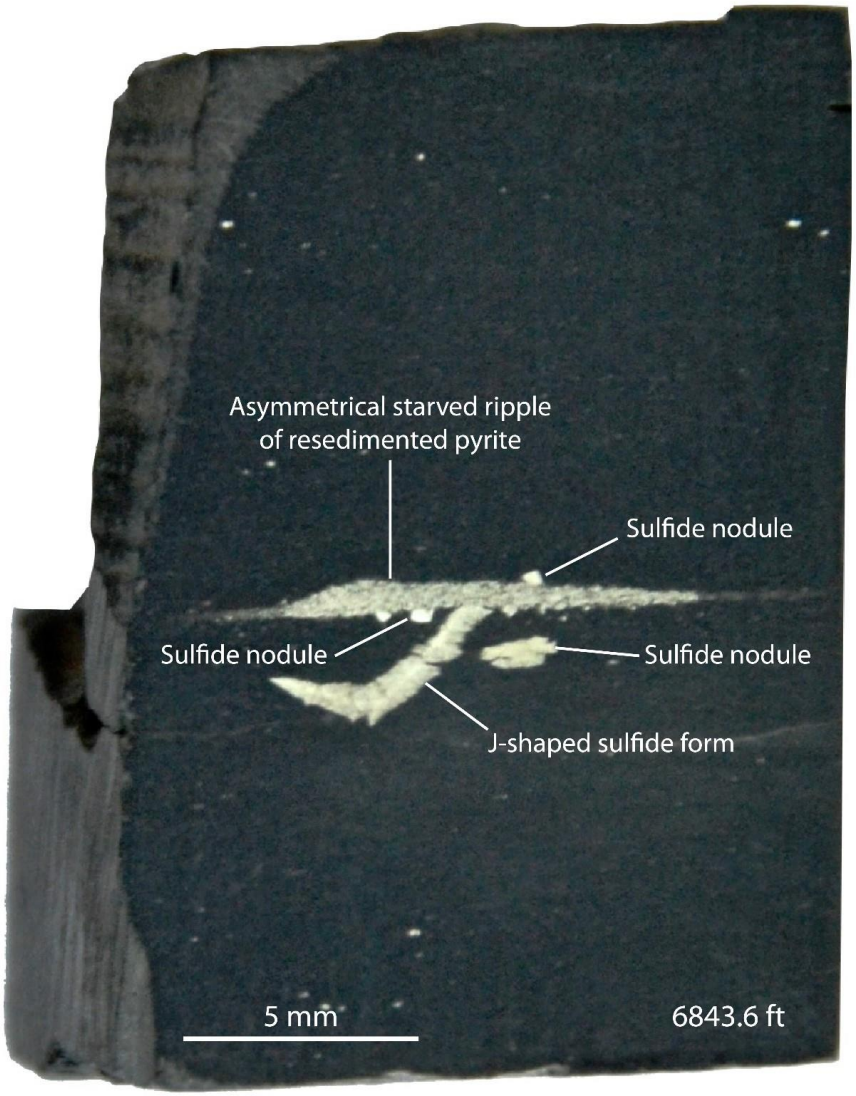

Figure 25. Photograph of black shale containing abundant sulfide minerals with diverse morphology, Anderson 12 no. 1 core, 6,843.6 ft.

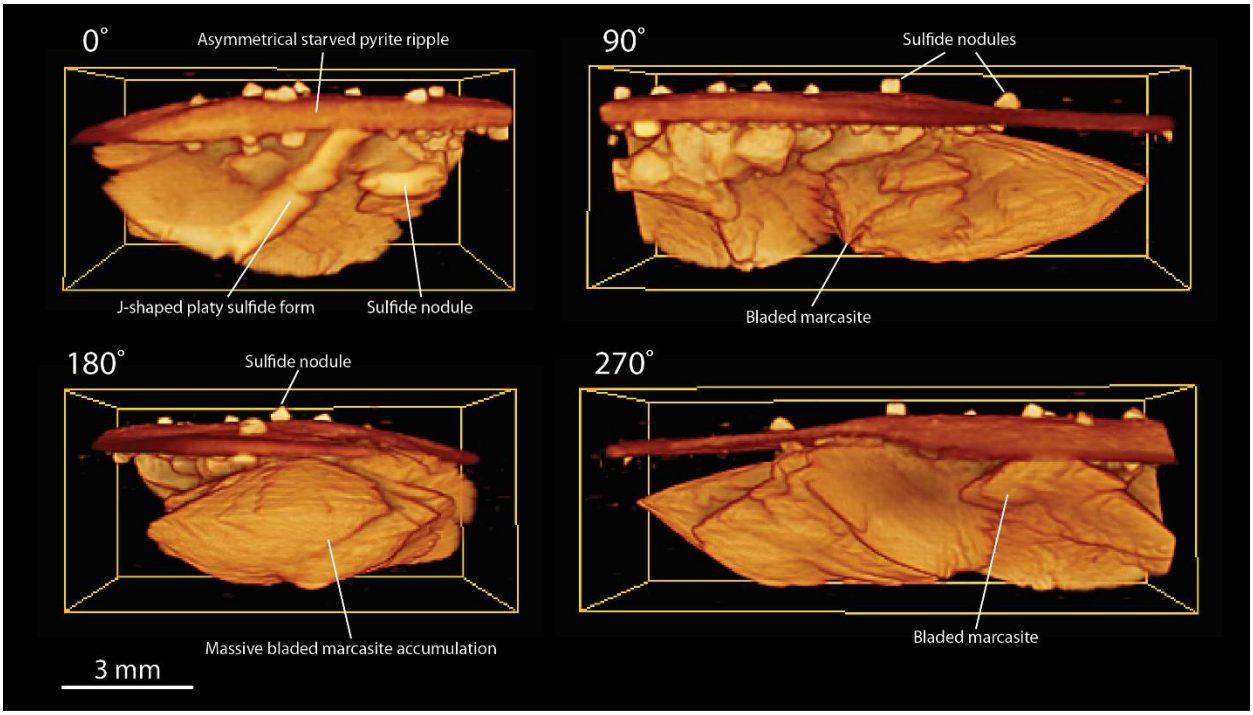

Figure 26. Glow density filtered tomograph presented at four different angles, Anderson 12 no. 1 core, 6,843.6 ft. Pyrite appears as an asymmetrical starved ripple. Sulfide nodules are seen above and below the ripple. The largest sulfide nodules contain platy and bladed crystals, indicating formation of marcasite.

A cross-sectional CT slice of the large sulfide mass reveals its morphology in great detail (Fig. 27). The bladed nature of the marcasite accumulation is very apparent at this view. Marcasite nodules are also visible above and below the pyrite ripple, with a massive nodular accumulation of marcasite to the right of the bladed forms.

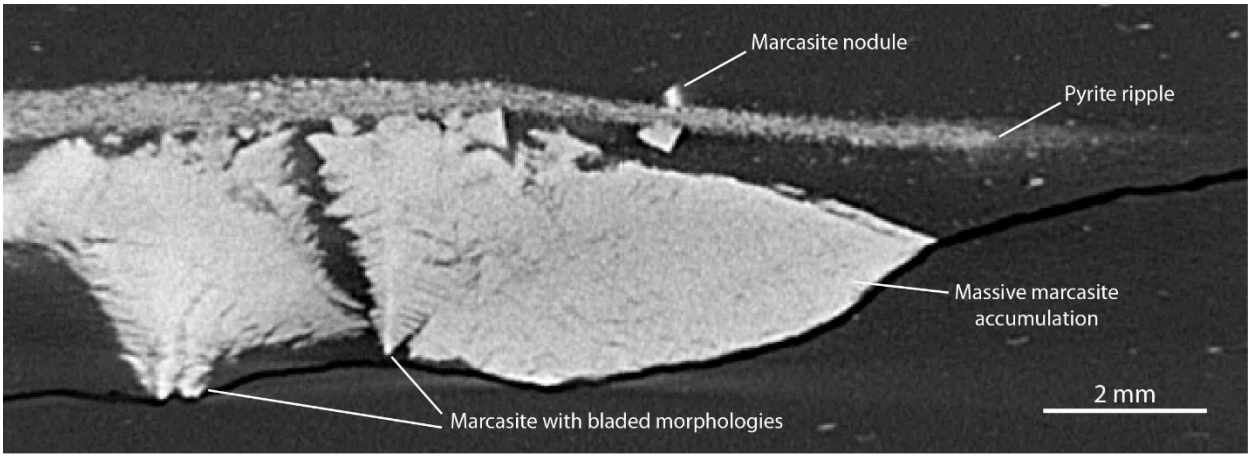

Figure 27. CT slice showing a pyrite ripple with various forms of marcasite above and below, Anderson 12 no. 1 core, 6,843.6 ft. Sulfide is nodular above the ripple and forms large nodules with bladed crystals below.

The sample from 6,900.7 ft is black shale with an unusual lag bed and contains laminasets composed of about 14 siltstone-shale couplets (Fig. 28). The lag bed marks a condensed marine flooding interval near the base of the Famennian Series just above the *Foerstia* zone. A cropped tomograph of the sample proved to be an excellent way of examining the constituents of the lag bed (Fig. 29). The lag is pyritic and includes phosphate and glauconite clasts, detrital quartz grains, conodont elements, and sparse vertebrate skeletal debris. The siltstone-shale couplets form laminasets containing up to 14 laminae, suggestive of spring-neap tidal cycles (Callner, 2014). When compared to the photograph, siltstone-shale couplets in the tomograph did not image clearly.

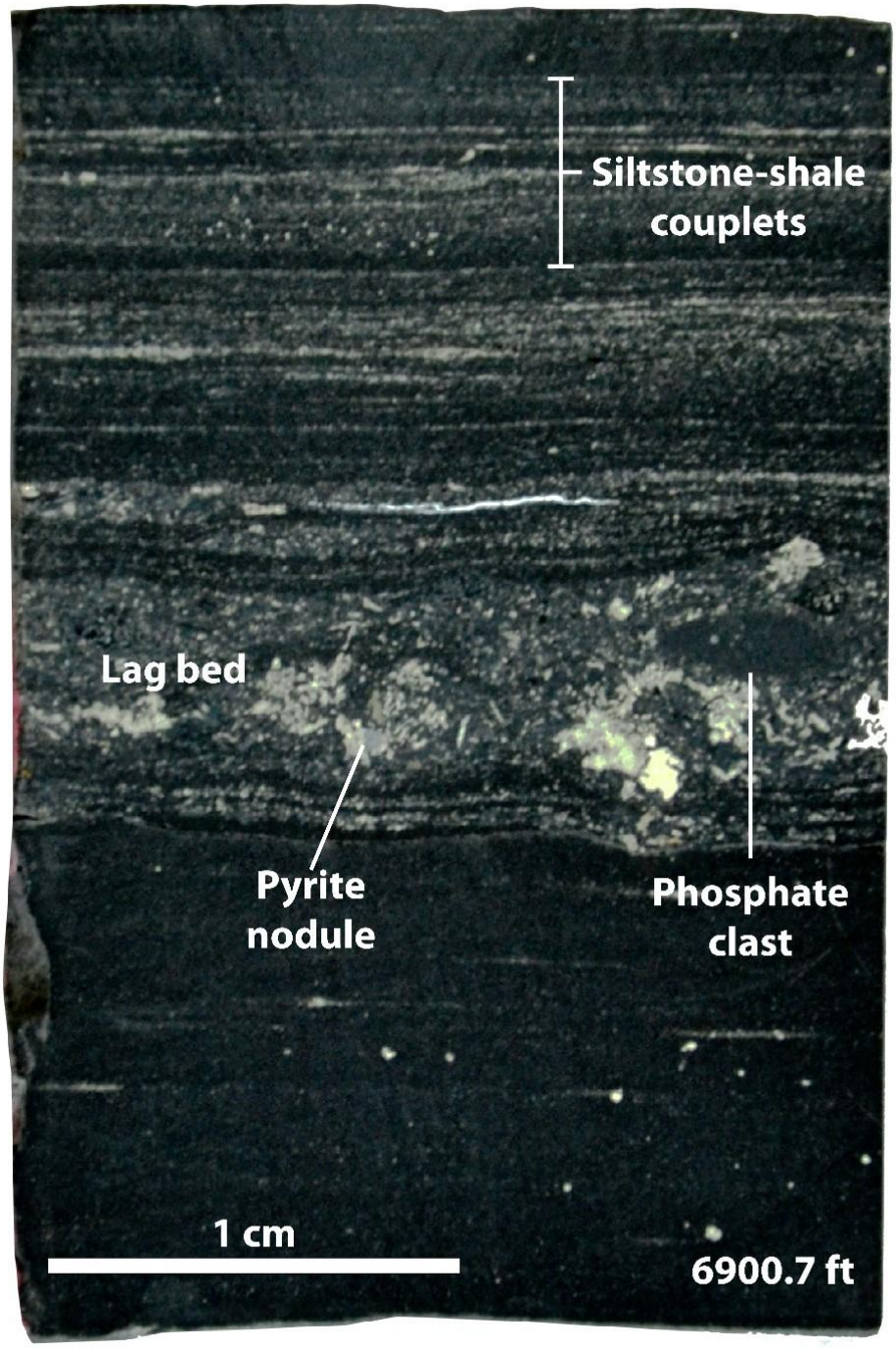

Figure 28. Photograph of black shale containing a thin lag bed and bundled siltstone-shale couplets, Anderson 12 no. 1 core, 6,900.7 ft. The lag bed is pyritic and includes lithoclasts of phosphate and glauconite, as well as abundant conodont elements. .

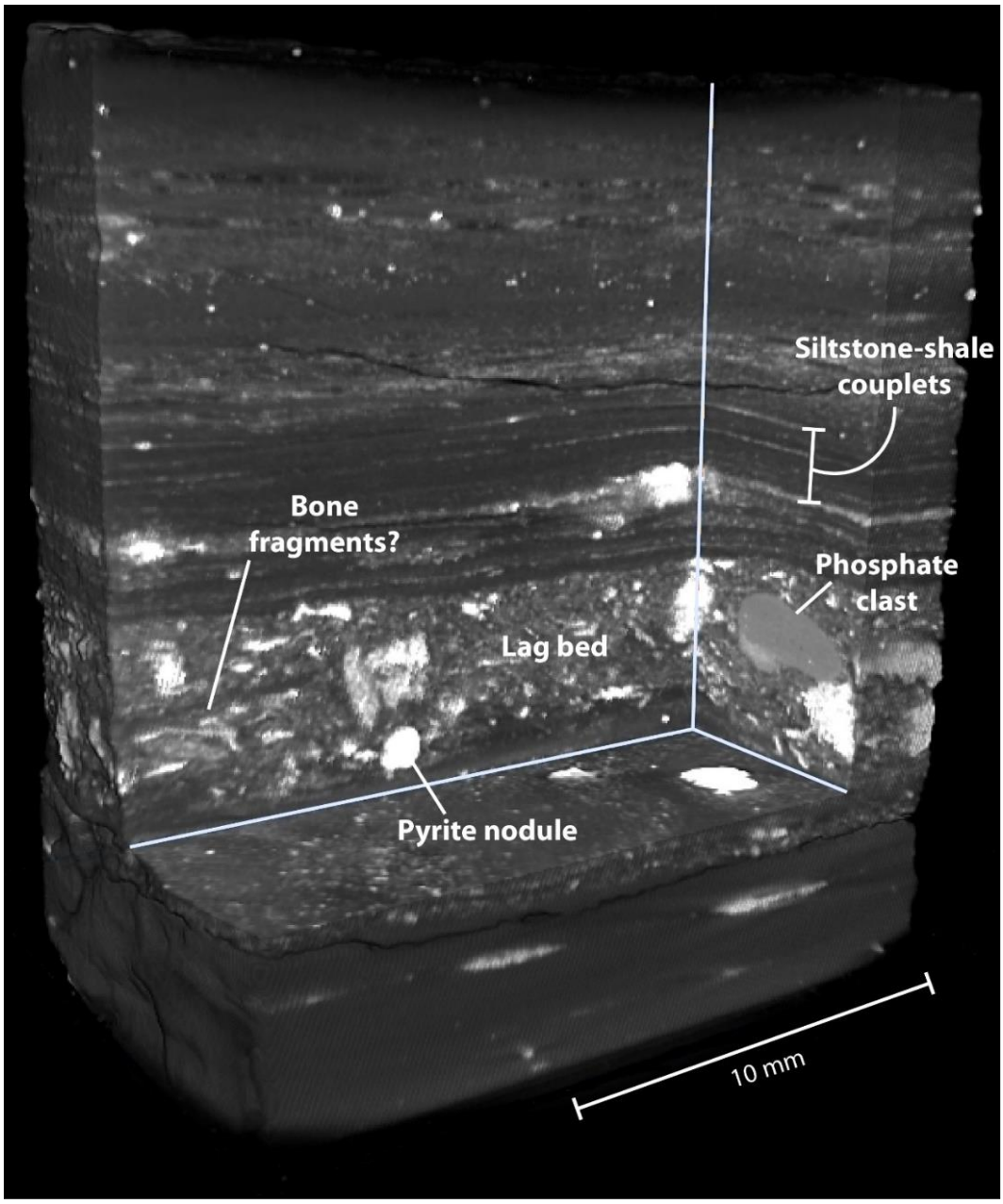

Figure 29. Gray ramp density filtered cropped tomograph, Anderson 12 no. 1 core, 6,900.7 ft. Cropping the tomograph exposed the internal fabric of the rock. Siltstone-shale couplets appear blurry. Lag constituents are readily identified.

Everhart-Thornley SEM micrographs of an argon ion milled sample from the Anderson core show aspects of the rock matrix and porosity that were not observable using CT analysis. A look at the microfabric reveals detrital quartz grains and a variety of pyrite forms in a matrix of

clay platelets aligned with bedding (Fig. 30). Organic matter fills the void space between the clay, quartz and pyrite particles. Pyrite occurs as framboids, nodules, euhedral crystals and dispersed grains. Pores were was observed as both intraparticle and fissure porosity (Fig. 31). The fissure porosity occurs in the organic matter, typically at or near the contacts between organic and mineral matter and is likely to have formed as a result of hydrocarbon generation (i.e. organic porosity). The elongate fissure pores measure 1 – 5 μm in length and have an average aperture of 0.5 μm. Intragranular porosity was observed within a quartz grain at the nanoscopic scale.

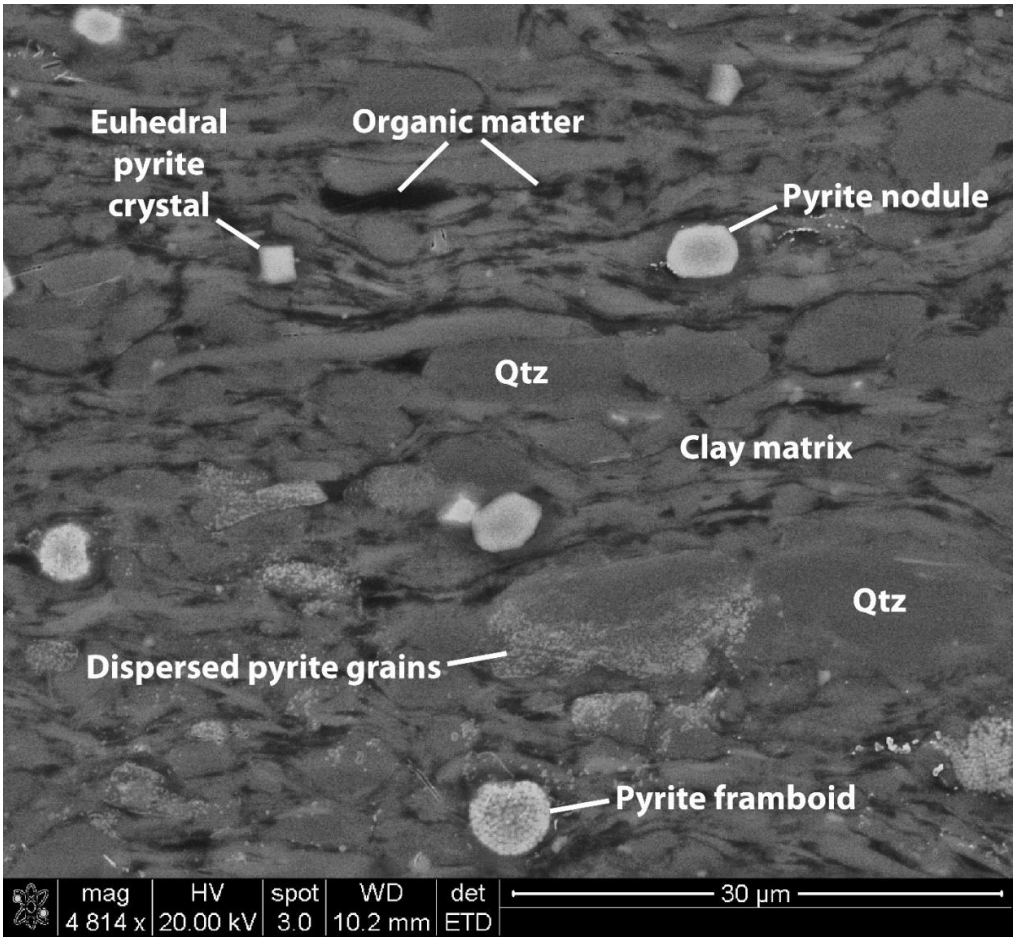

Figure 30. SEM ETD image of microfabric from an argon ion milled sample of Woodford Shale in the Anderson 12 no. 1 core, 6,893 ft. Microfabric shows diverse pyrite forms, detrital quartz, and a clay matrix of clay platelets aligned to bedding. Organic matter lines the mineral constituents.

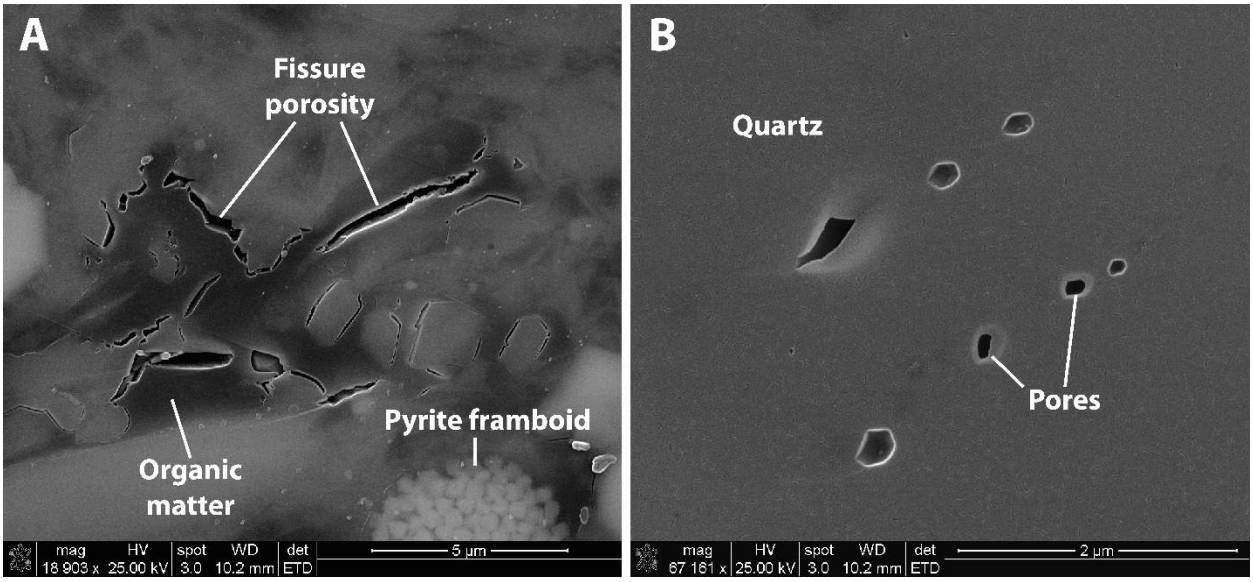

Figure 31. SEM ETD images of pores from an argon ion milled sample of Woodford Shale in the Anderson 12 no. 1 core, 6,893 ft. (A) Fissure porosity is observed in organic matter along mineral grain boundaries. (B) Intragranular, nanometer-scale pores in a quartz grain.

IV. 3.2 Poe 1-29 core

The Poe 1-29 well is in Hughes County in the western part of the Arkoma Basin. Two samples from depths of 7,843.7 ft and 7,848 ft were analyzed. The Poe samples, which underwent significant small-scale faulting and fracturing, were scanned in order to determine the utility of the CT scanner for studying samples from structurally complex areas.

The sample from 7,843.7 ft contains black shale with pyrite nodules and veins with ptygmatic folds that occur principally in chert laminae (Fig. 32). A density filtered CT slice from the sample reveals interlaminated siliceous and argillaceous strata that are not readily visible in the photograph of the sample (Fig. 33). Interestingly, the chert layers are not identifiable in the same CT slice. The silica vein fills also are invisible, apparently because of low density contrast between the silica in the vein fills and that forming the host chert. As in the photograph, pyrite is readily observed in the temperature density filtered CT slice. The varvelike appearance of the

strata is apparently due to variable silica content. Imaging these laminae demonstrates the capability of CT analysis to observe sedimentary features that would have otherwise gone undetected.

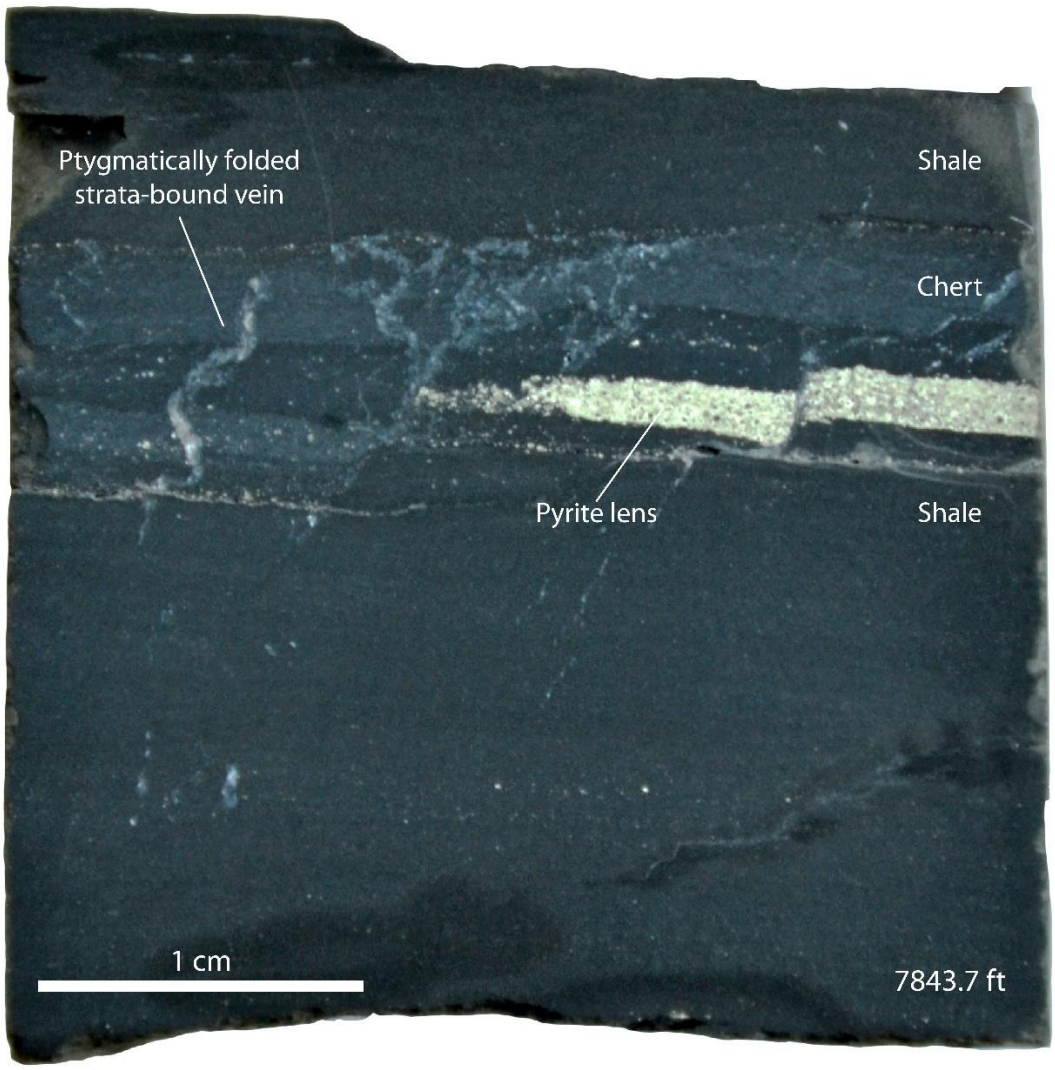

Figure 32. Photograph black shale with chert laminae, Poe 1-29 core, 7,843.7 ft. Note complexly folded strata-bound veins and faulted pyrite lens.

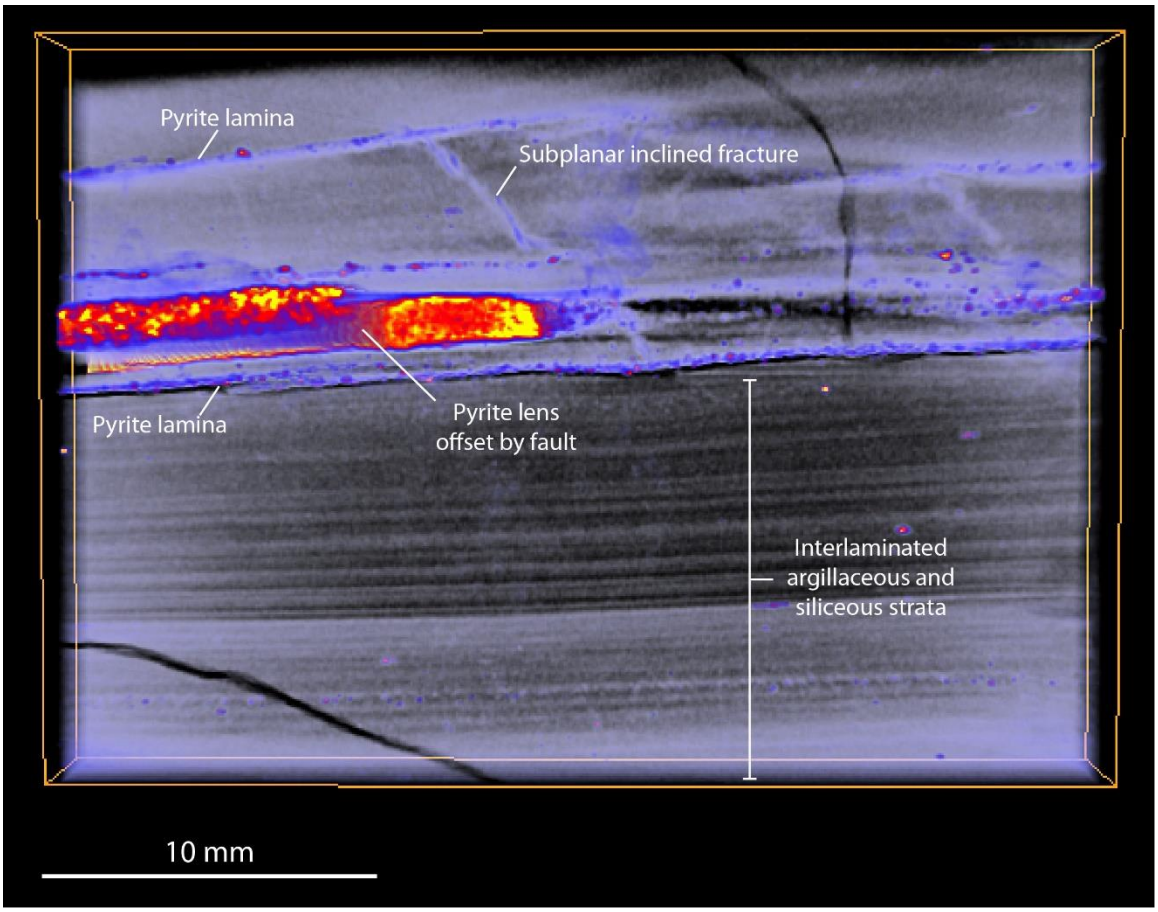

Figure 33. Temperature density filtered cropped tomograph of Woodford Shale, Poe 1-29 core, 7,843.7 ft. Pyrite laminae and nodules and a subplanar inclined fracture occur within the chert laminae. Thinly interlaminated argillaceous and siliceous laminae are also present.

The sample from 7,848 ft. contains black shale with pyrite laminae and strata-bound normal faults and shear veins in laminated chert (Fig. 34). A cropped tomograph of the sample reveals the geometry of the faults and shear veins and enables observation of the internal rock fabric (Fig. 35). The tomograph shows the intensity of strata-bound extensional deformation within interlaminated chert and shale. Shear veins, which apparently have enough density contrast to image, are mainly confined within laminated chert. The cropped face on the right shows a dip view, whereas the one on the left is closer to a strike view. High-angle listric faults are visible in the chert layer near the top of the sample and a bright pyrite lamina helps constrain

fault displacement. Veins in the upper layer correspond well with the faults, whereas those in the lower part of the sample do not match with the faults. A chert bed in the lower part of the sample is faulted, displaying a half graben geometry. The image shows progressive downstepping of antithetic faults in the hanging wall of the system. Above this rollover structure is high angle strata-bound shear veins in the overlying chert.

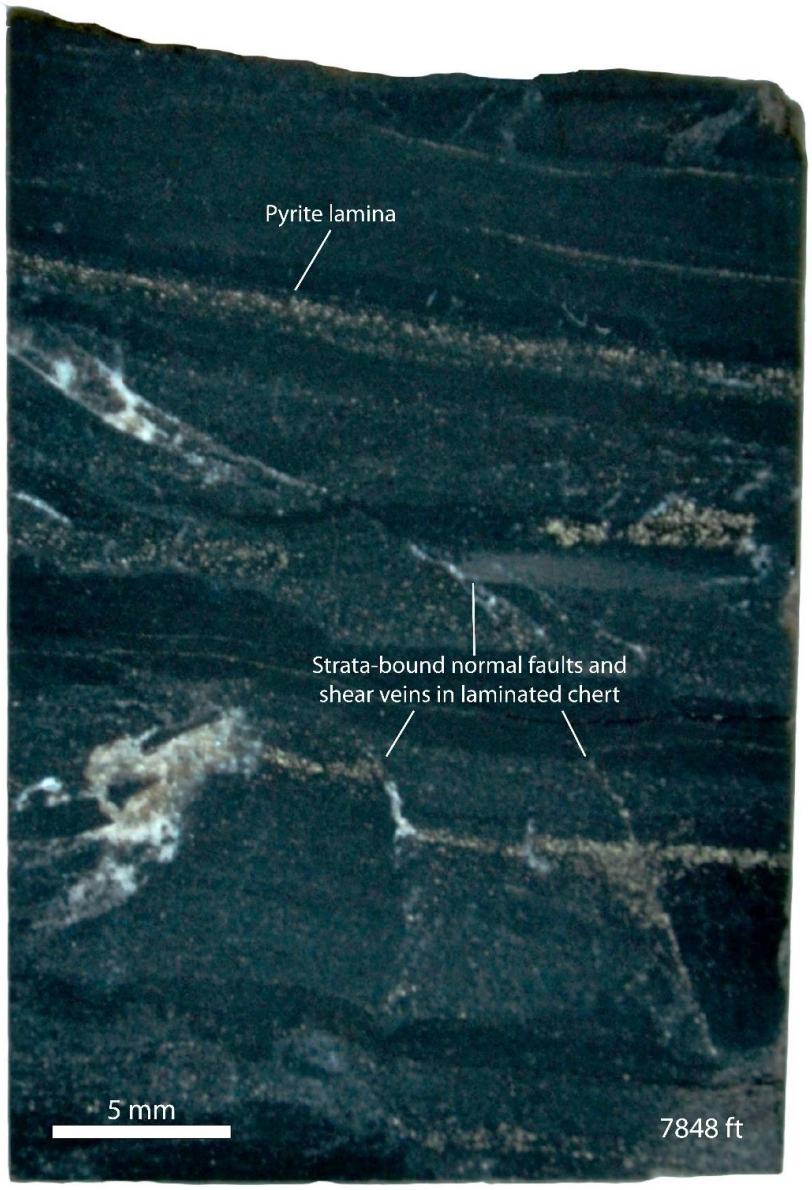

Figure 34. Photograph black shale with pyrite laminae and a complex array of faults and veins, Poe 1-29 core, 7,848 ft.

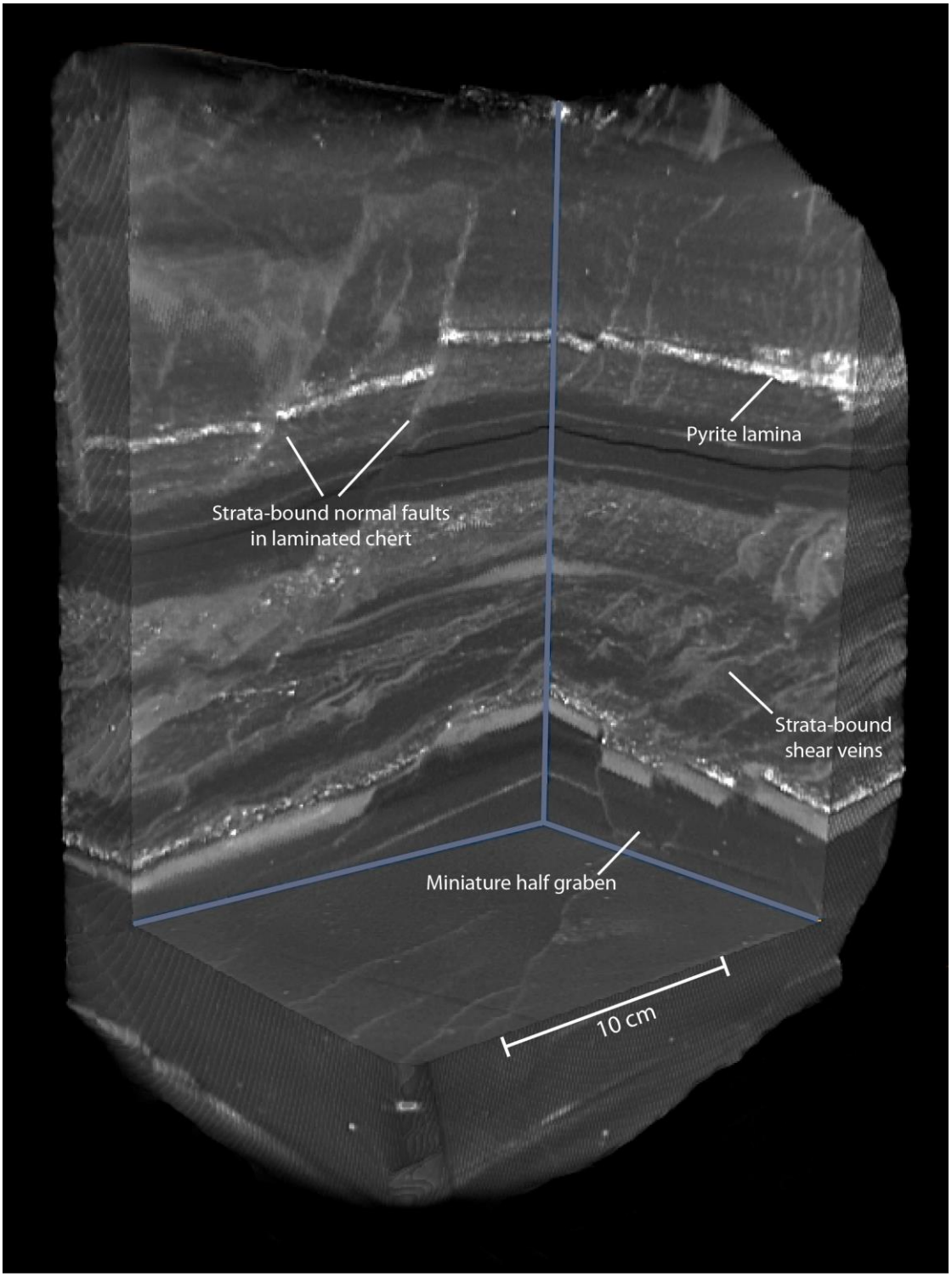

Figure 35. Gray ramp density filtered cropped tomograph of Woodford Shale, Poe 1-29 core, 7,848 ft. Normal faults and shear veins are largely bound within the laminated chert. A miniature half graben is preserved in the lower part of the sample.

IV. 3.3 Hall 2B core

The Hall 2B well is in Caddo County, Oklahoma in an uplifted fault block along the southwestern margin of the Southern Oklahoma Aulacogen, which is an early Paleozoic Iapetan continental rift, and the Anadarko basin which is a flexural basin that formed by thrusting along the margin of the aulacogen during the Carboniferous-Permian Wichita Orogeny. Two samples from the core were analyzed (Table 1). The cored interval is in an intensely fractured and brecciated section dominated by very dark gray novaculitic chert that is interstratified with lesser amounts of black, organic-rich shale. The core contains multiple slumplike structures and internal angular unconformities, suggesting that sedimentation took place on unstable slopes as faults were reactivated along the margin of the aulocogen during Late Devonian time (Callner, 2014).

The sample from 5,899 ft is from a highly fractured chert bed (Fig. 36). The photograph shows abundant quartz veins, as well as some mm-scale brecciated chert clasts and pyrite nodules. A vertical slice acquired from the CT tomograph reveals the internal fabric of the sample (Fig. 37). The CT slice displays several different features, including pyrite nodules and subrounded to angular chert clasts in a shale matrix, two sets of quartz veins dipping at 80° and 50° and a network of fracture porosity. Analyzing these features in the CT slice allows for an interpretation of relative ages and a chronological sequence of events. The majority of the chert clasts near the base of the layer cannot be fit together and are subrounded, indicating that the chert clasts and pyrite were reworked and transported. Although, it is possible that the pyrite nodules were a product of late-stage diagenesis. The next event was deposition of the main chert bed. The chert bed was subsequently fractured and the two sets of veins that were formed were filled with quartz. The veins likely formed simultaneously, as neither of the vein sets appears to cross-cut the other. The next thing to occur was an intense brecciation event that created the open

fractures. The open fracture network offsetting the sets of quartz veins indicates that the brecciation occurred in-situ.

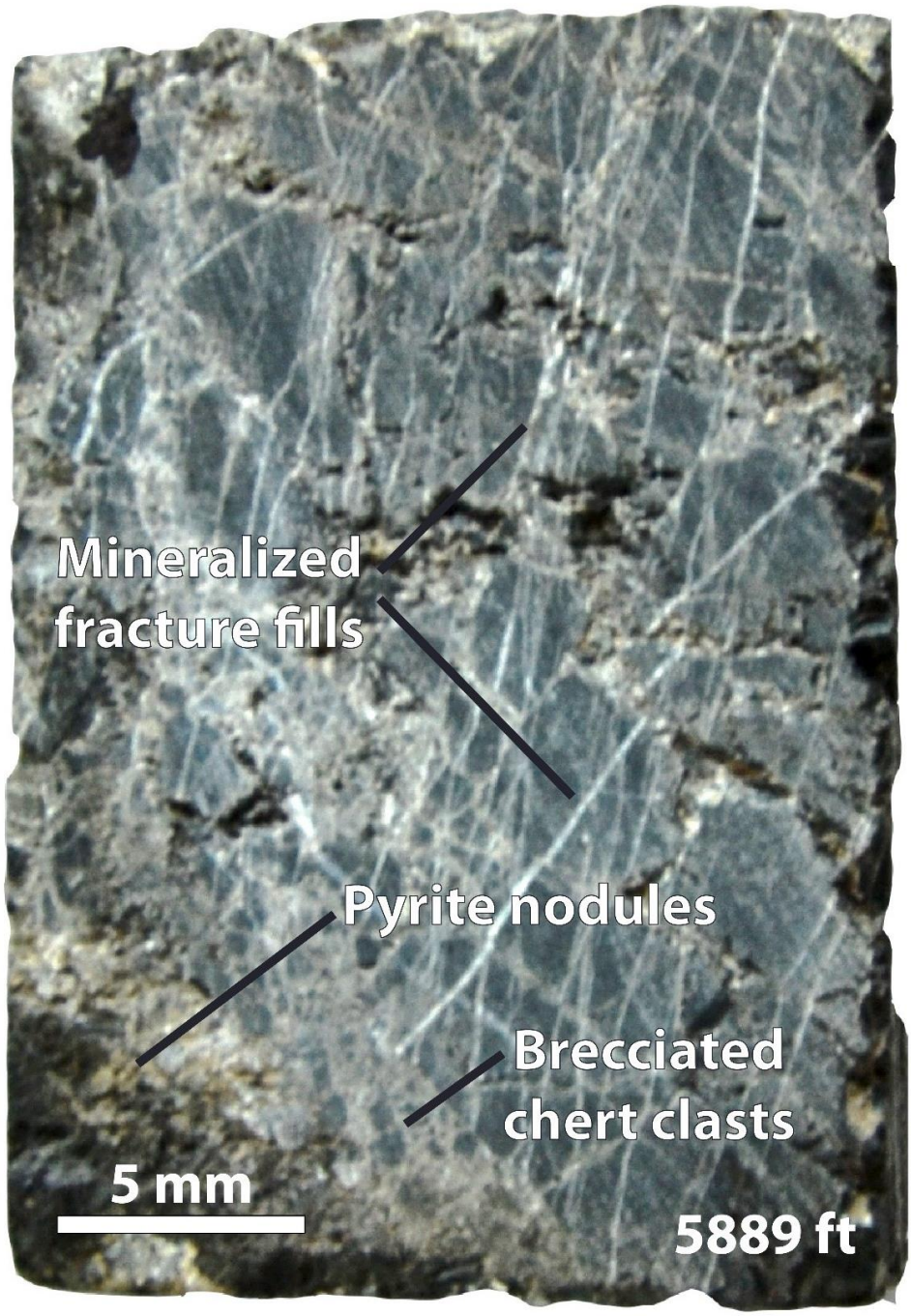

Figure 36. Photograph of highly fractured Woodford chert with quartz veins, Hall 2B core, 5,899 ft. Note brecciated chert clasts and pyrite nodules in lower left part of sample.

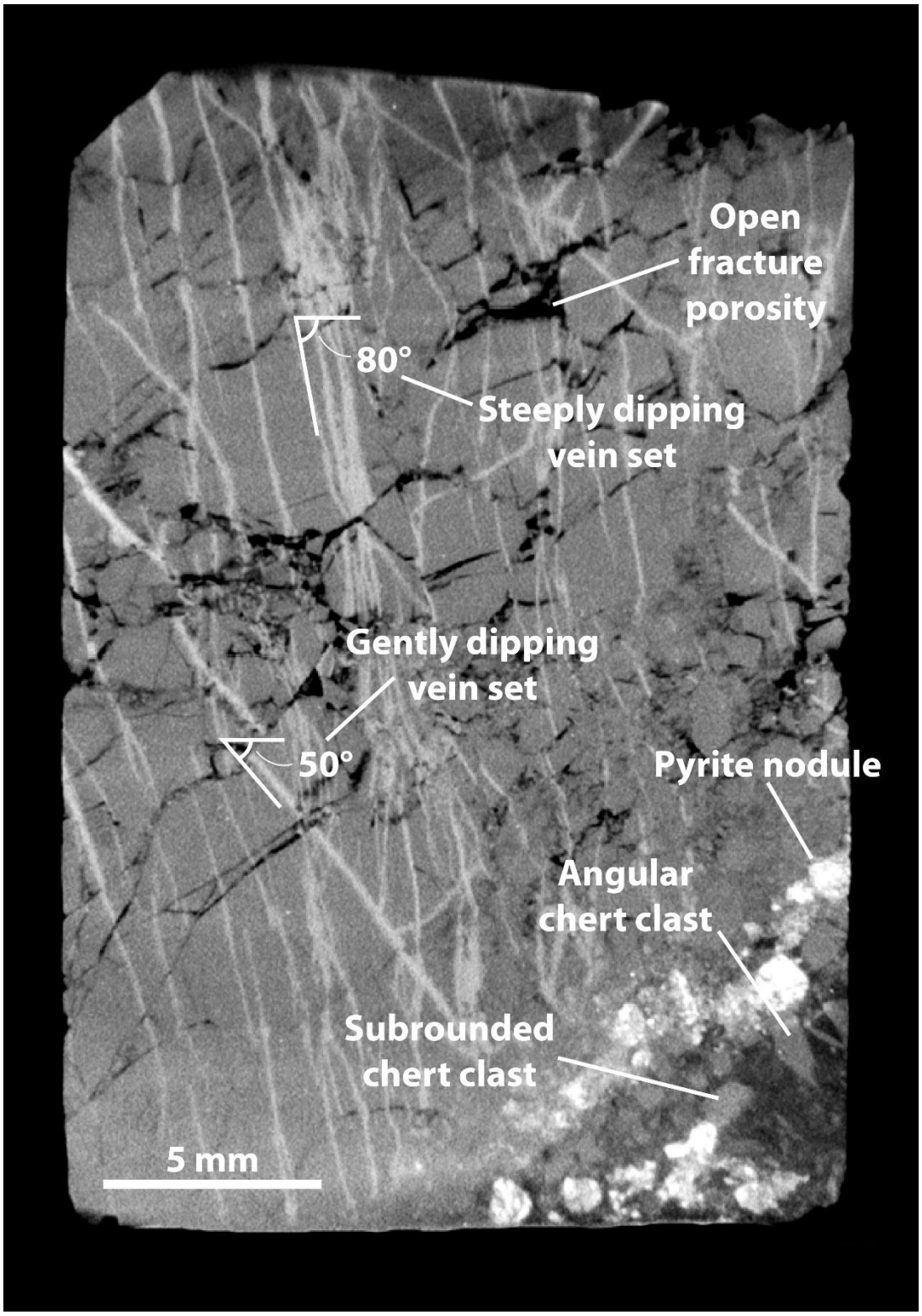

Figure 37. CT slice showing two sets of quartz veins, open fracture porosity, subrounded to angular chert clasts and pyrite nodules, Hall 2B core, 5,899 ft.

By segmenting veins and open fractures via histogram cutoffs, three-dimensional renderings were generated (Fig. 38). Although the two sets of quartz veins are offset slightly by the open fractures, they are readily traceable throughout the entire sample volume. Contrarily, the open fracture network appears as discontinuous pockets of porosity with very little interconnectivity throughout the sample. The three-dimensional rendering of the open fracture network appears this way because the extraction process did not pick up the hairline fractures imaged in the CT slice (fig. 37). The hairline fractures did not image because they were below the voxel resolution of 31 μm. Imaging of these fractures in the CT slice is a result of partial volume effects, which make the fracture apertures appear too wide and with elevated gray levels. While there is clearly a resolution limitation that prevents accurate assessment of interconnectivity in three-dimensions, the image still shows great variation of fracture aperture associated with brecciation.

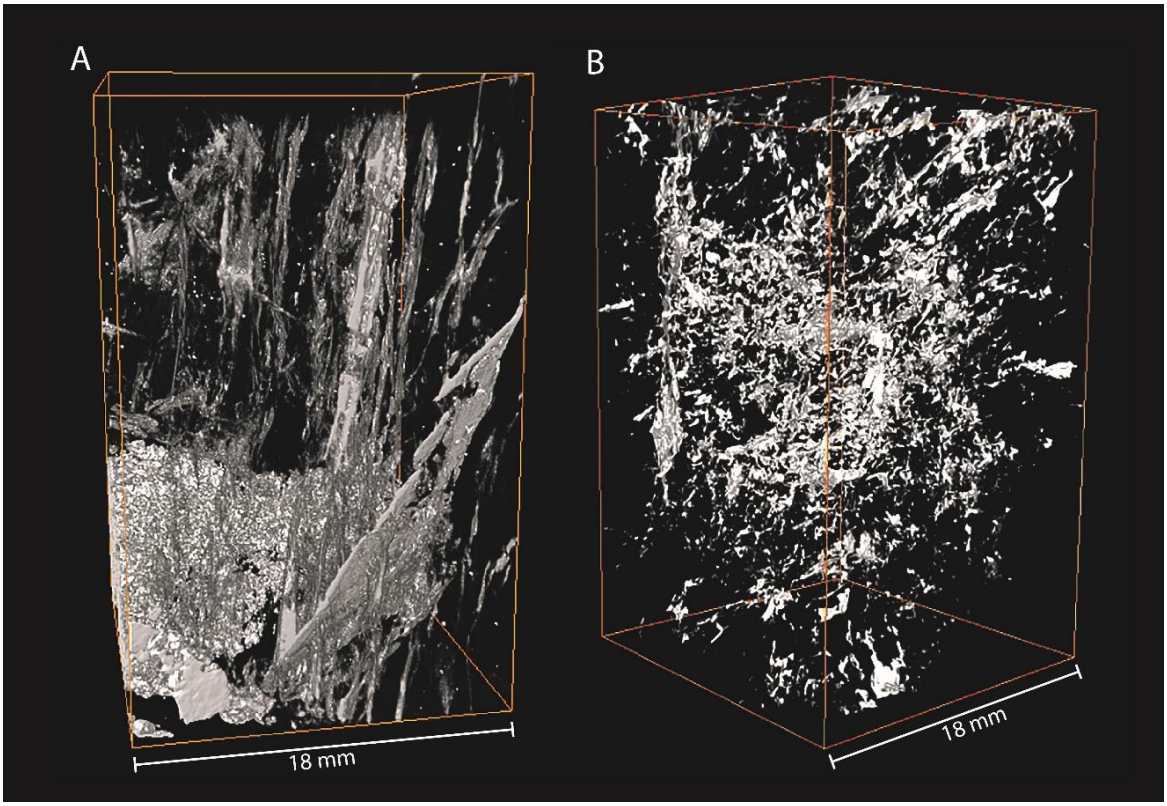

Figure 38. Three-dimensional renderings displaying the interconnectivity of the fracture networks, Hall 2B core, 5,899 ft. (A) Two sets of quartz veins, dipping 50° and 80°, are preserved. (B) Open fractures appear as discontinuous pockets of porosity throughout the sample. The extraction failed to image interconnecting hairline fractures with aperture below the voxel resolution of 31 μm.

Using ImageJ software, an operation was performed to quantify the volumetric percentage of imageable open fracture porosity in the sample. The CT data contain 1,004 slices, but only the center portions of 743 slices were used in the calculations in order to omit the pitted surfaces of the sample where rock fragments may have popped out and to eliminate edge effects at the margins of the CT scan (Fig. 39).Using the 743 slices, the histograms for all of the slices were stacked, and histogram cutoffs were applied manually to segment the fracture porosity (Fig. 40). Volumetric analysis yielded fracture porosity of 7.08%. It is important to note that this

calculation is a minimum estimate because the sample contains numerous hairline fractures that could not be extracted.

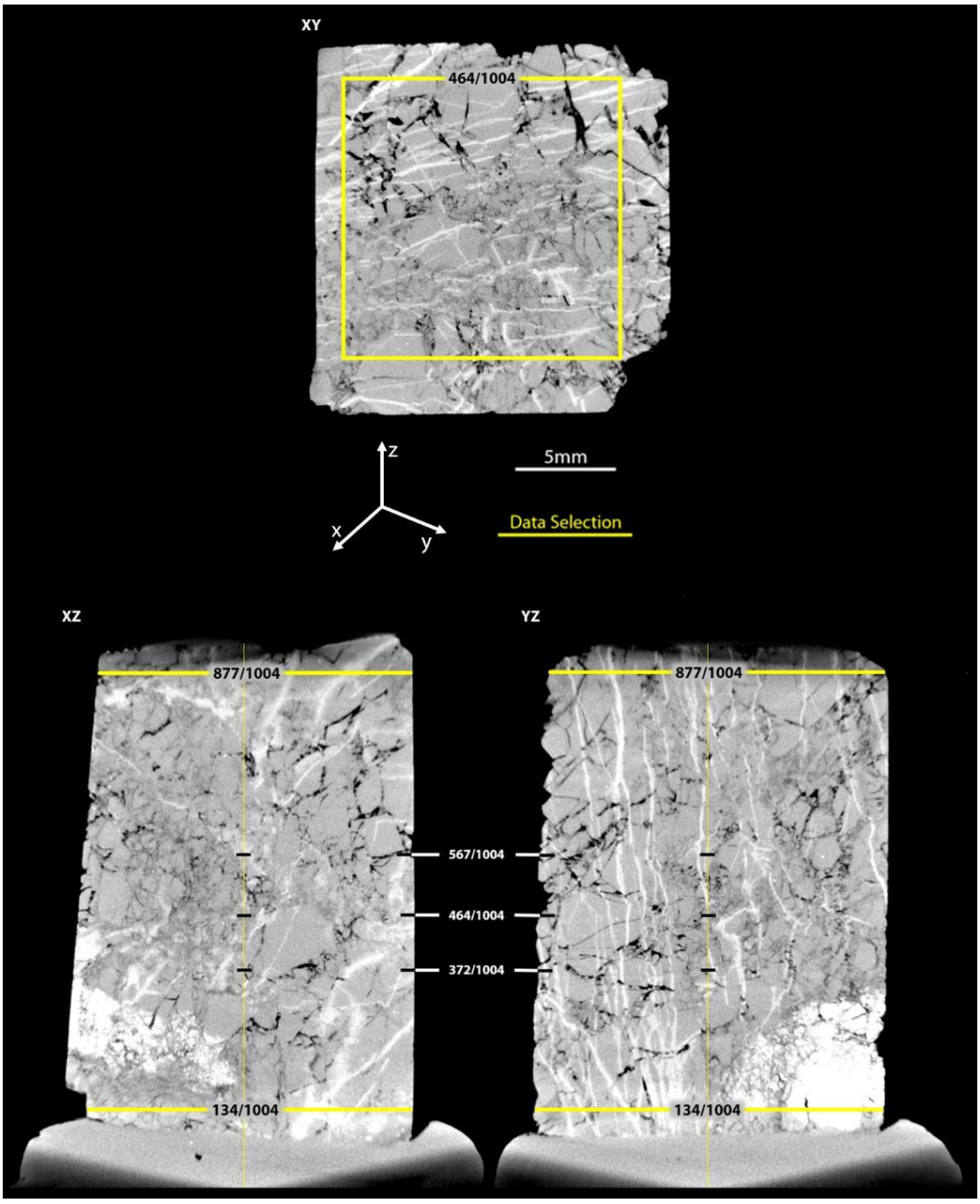

Figure 39. CT slices of brecciated chert showing the datum that were selected for calculating a volumetric percentage of fracture porosity, Hall 2B core, 5,899 ft. Yellow box defines scan area for porosity determination

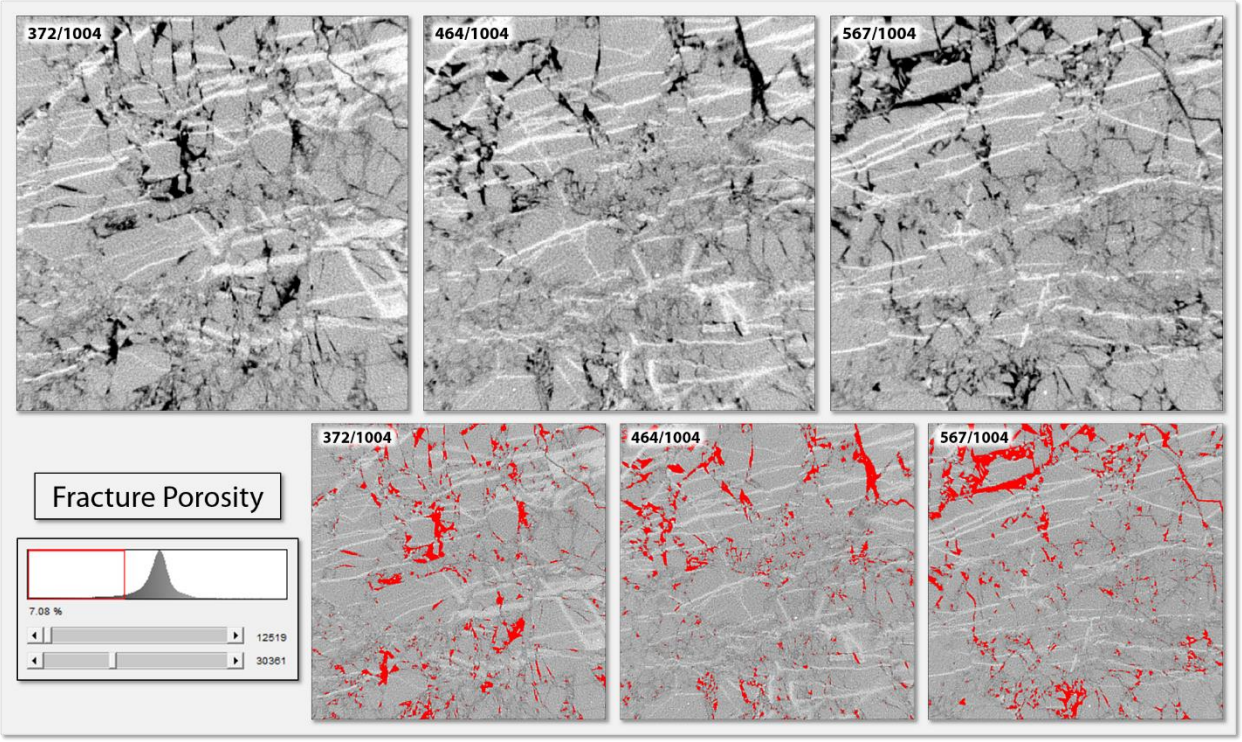

Figure 40. CT slices showing raw images and volumetric segmentation for porosity determination (highlighted in red), Hall 2B core, 5,899 ft. CT slices on the top correspond to the segmented images on the bottom and were used as visual references when applying the histogram cutoffs for segmentation (lower left).

A portion of the sample was ion milled and examined using SEM/EDS. The microfabric exhibits what appears to be fracture slit pores aligned along chert clast boundaries (Fig. 41). The pores are elongate to irregularly shaped and define fractures that have partially annealed by silica cementation. This is a good demonstration of how using SEM can reveal fine details that cannot be observed using CT. Not only are the pores below the resolution of the CT scan that was performed, but the chert clasts are in a matrix of silica, which does not provide sufficient density contrast for x-ray imaging.

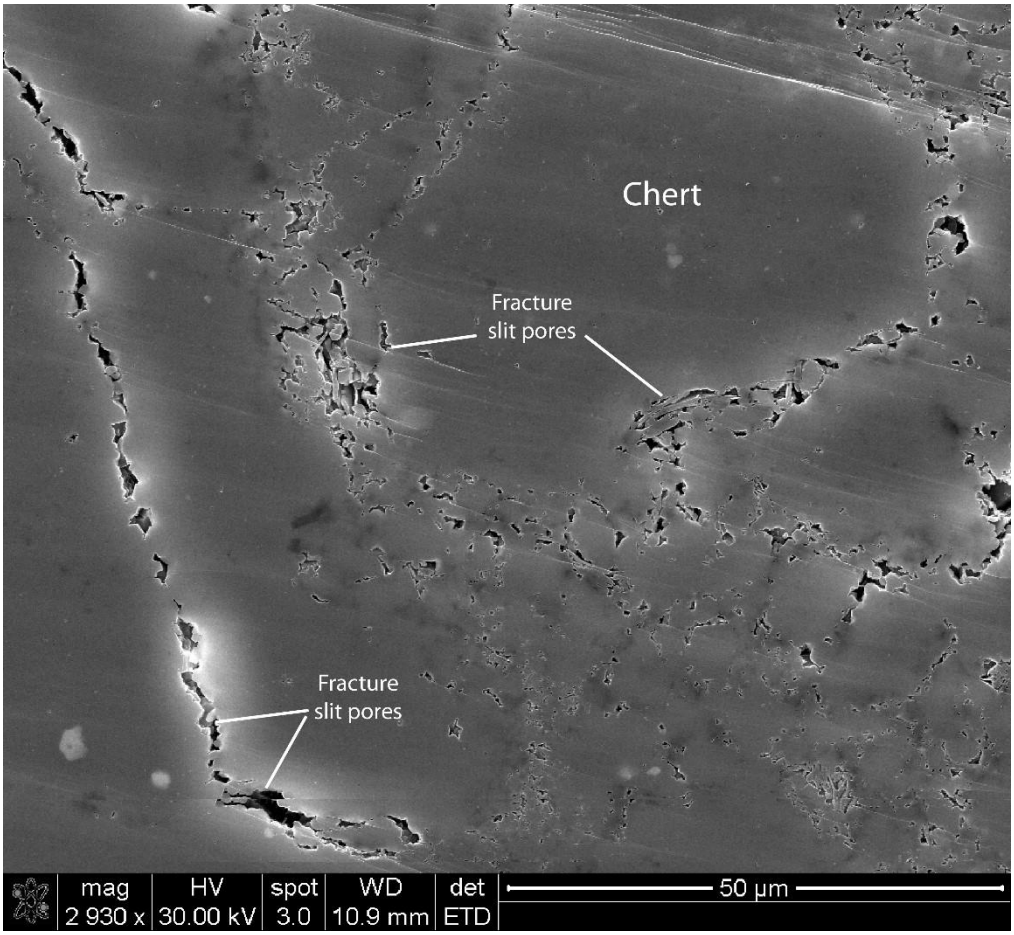

Figure 41. SEM ETD image of pores from an argon ion milled sample, Hall 2B core, 5,899 ft. Porosity appears as partially annealed fracture slit pores along chert clast boundaries.

Another method for viewing rock features that have similar densities or are below scanning resolution is thin section petrography. A thin sections from a Hall 2B sample reveals not only the brecciated texture and silica-cemented fracture fills, but organic-coated silica spheres, which include the remains of radiolaria, *Tasmanites*, and acritarchs (Figs. 42, 43).

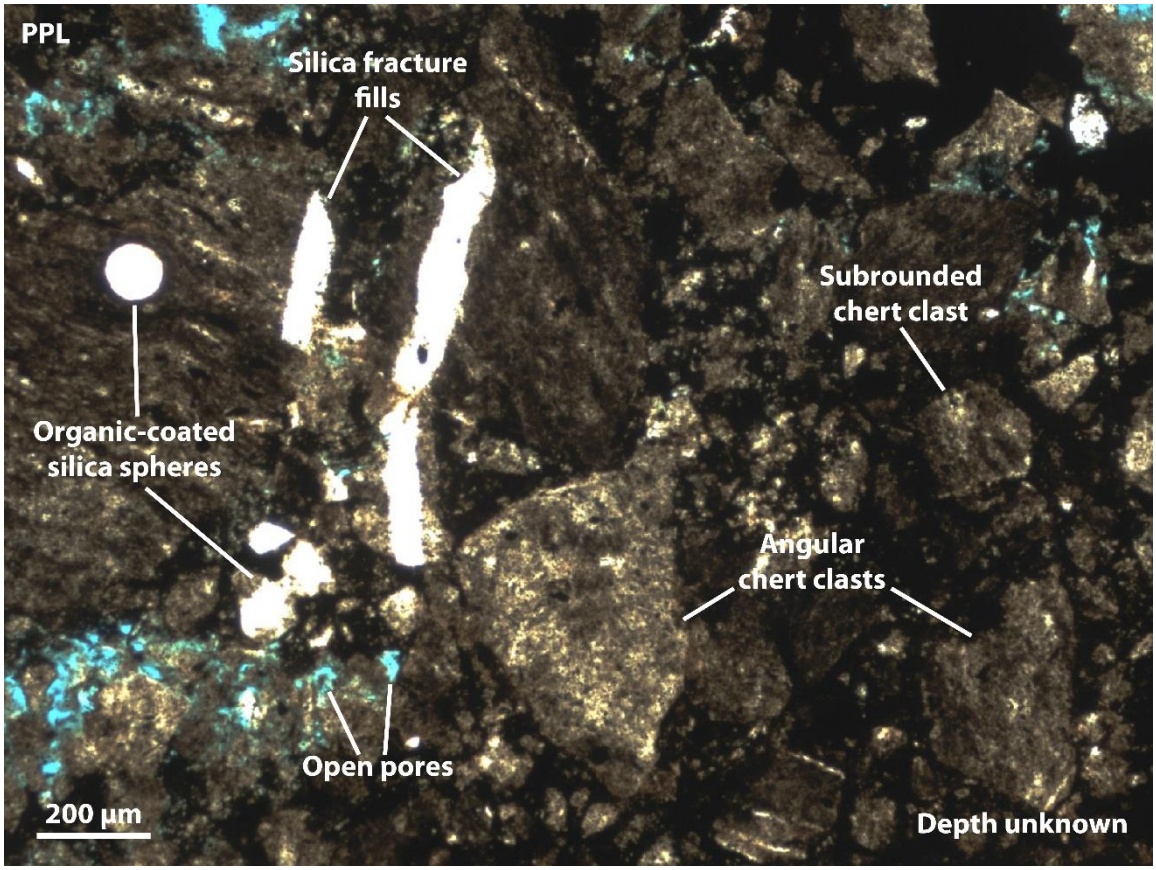

Figure 42. Thin section of chert breccia from the Hall 2B core photographed under plane-polarized light (courtesy, Jack C. Pashin). Chert breccia containing organic-coated silica spheres, silica fracture fills, and open pores.

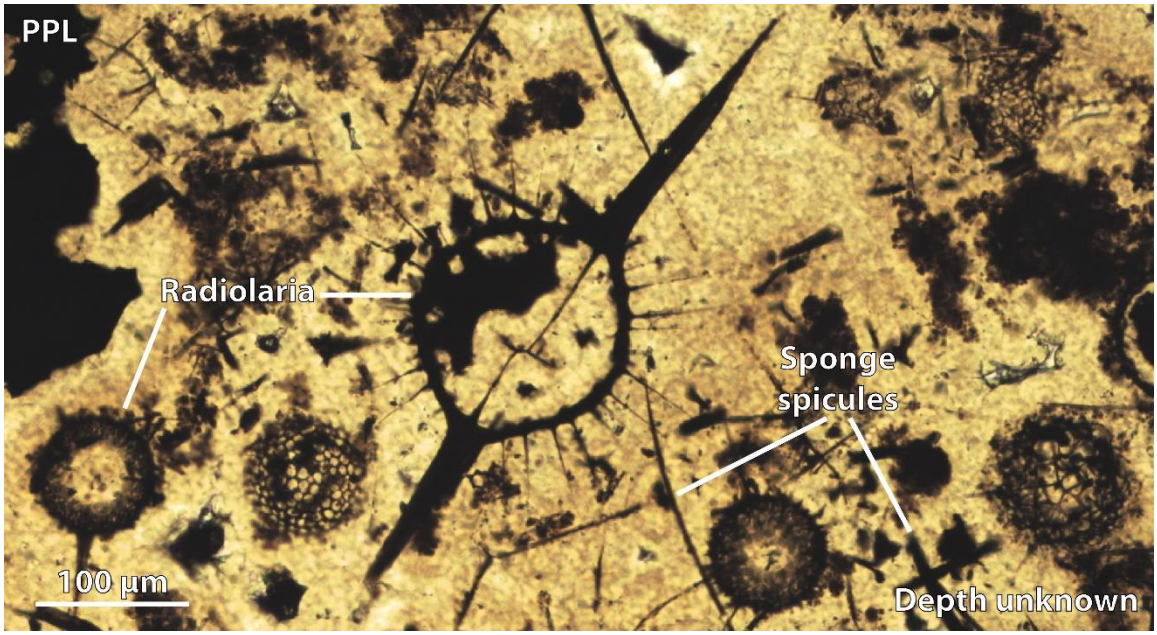

Figure 43. Thin section of a phosphate nodule from the Hall 2B core photographed under plane-polarized light (field of view = 0.75 mm wide). Note exceptional preservation of radiolaria and siliceous sponge spicules, which cannot be imaged in chert with CT technology because of low density contrast (courtesy of Jack C. Pashin).

A sample from 6,178.5 ft. consists of fractured chert blocks separated by a shale layer (Fig. 44). A CT slice of the sample reveals faulting and brecciation in the chert, which is separated by a shale layer. There is pyrite laminae within the shale and folding that occurs at the top of the layer (Fig. 45). Whereas the internal pyrite laminae and the faulting in the chert are observable in hand sample, the occurrence of folding in the shale layer is not. The faulting in the chert layer is likely syndepositonal because it appears that the shale layer above was not affected. A later tectonic event apparently brecciated the brittle chert layer and deformed the ductile shale layer.

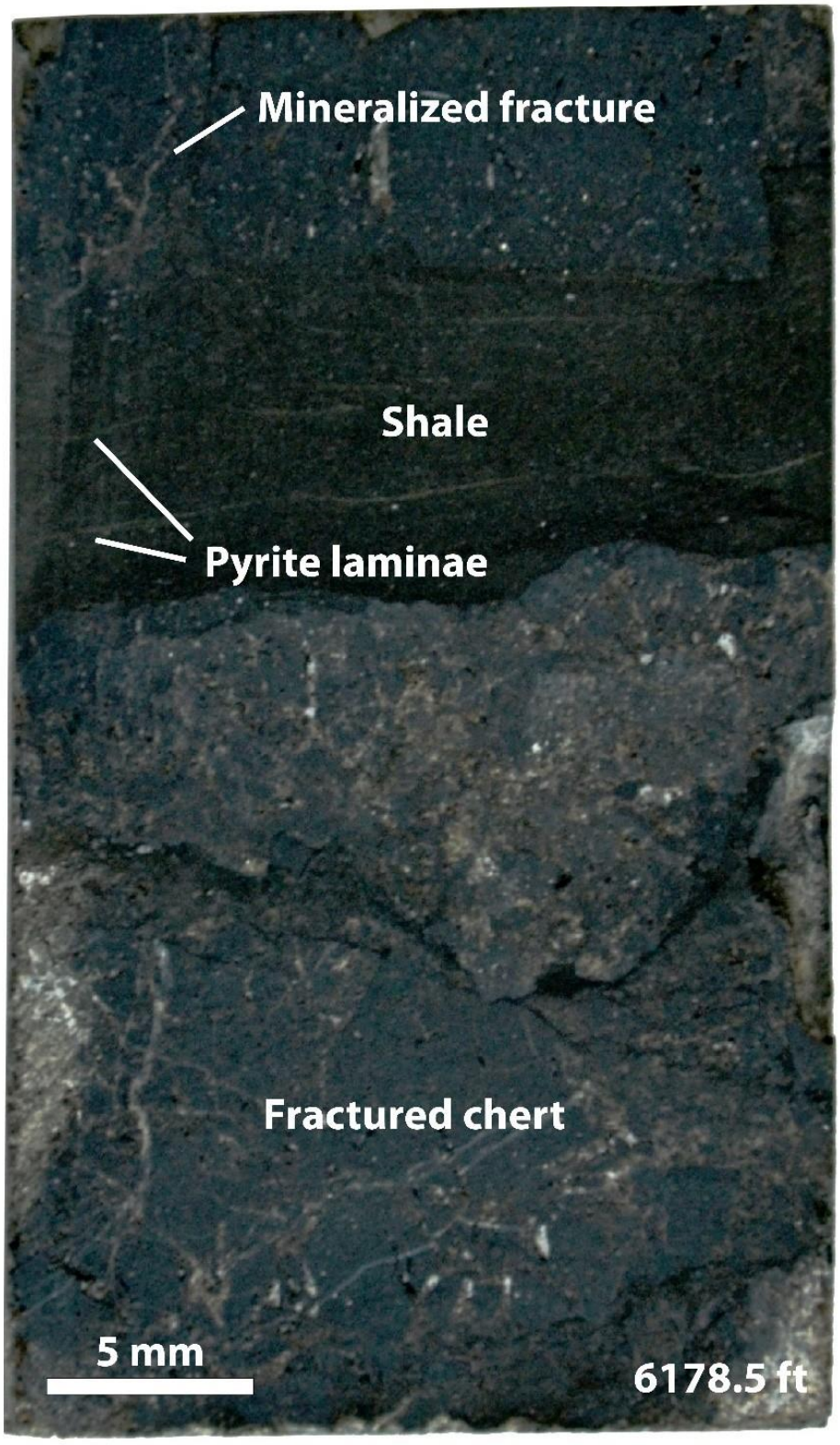

Figure 44. Photograph of fractured chert beds separated by black shale, Hall 2B core, 6,178.5 ft.

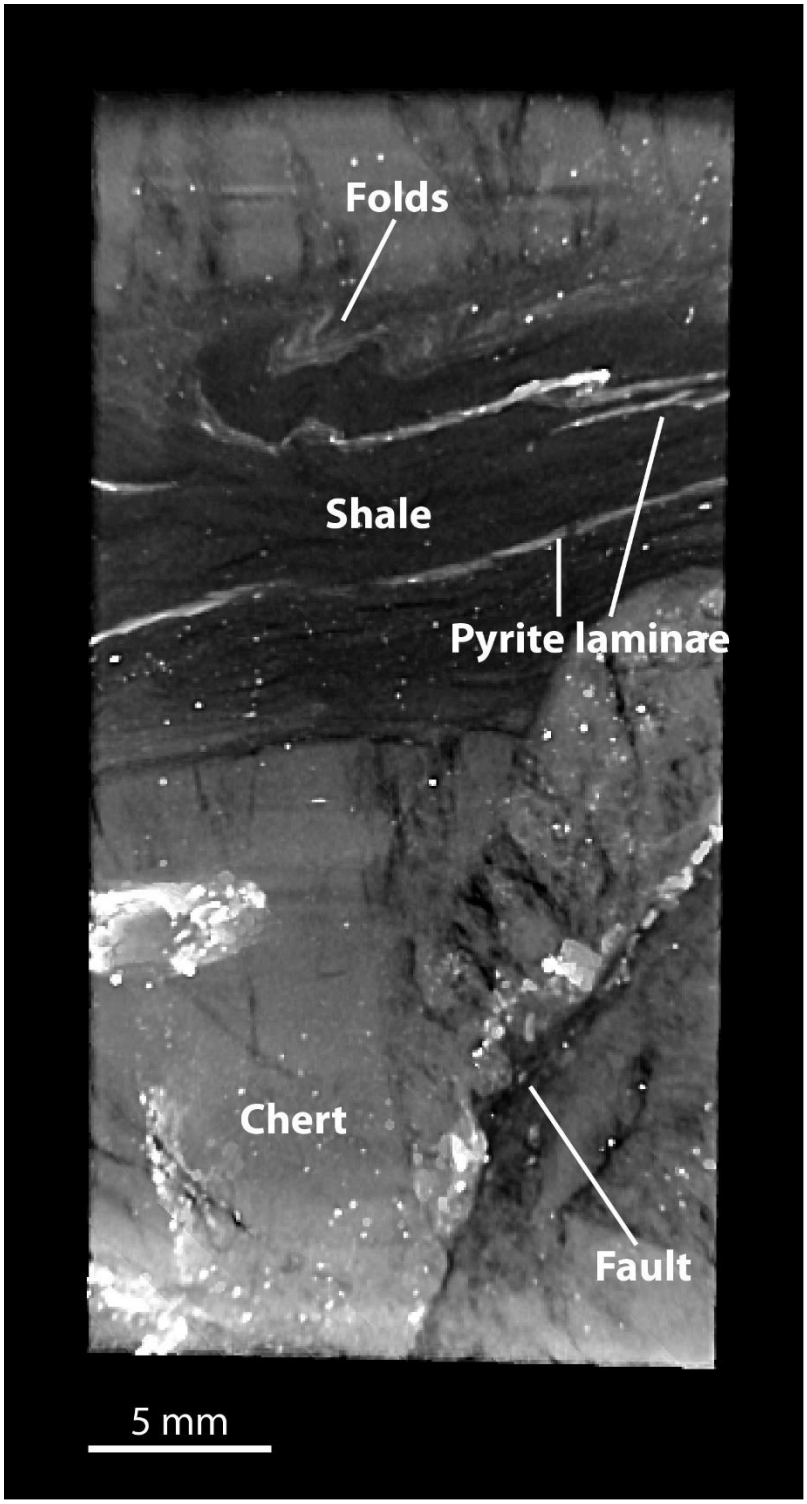

Figure 45. CT slice showing faulted chert blocks separated by a shale layer that has internal pyrite laminae and folds at the top of it, Hall 2B core, 6,178.5 ft. The chert layer appears to be faulted and brecciated.

Chert from a depth of 6,178.5 ft was argon ion milled and examined using SEM/EDS. The microfabric exhibits fissure porosity in organic matter (Fig.46) and thus appears similar to the Anderson sample that was analyzed (Fig. 31). EDS analysis indicates that the sample contains no clay (Fig. 47) and this is also supported by XRF analysis of the sample (Callner, 2014). The matrix consists of mainly chert, with some pyrite and nodules of peloidal phosphate . Organic matter fills the void space and serves as a lining between the chert, phosphate and pyrite. The pyrite nodules are likely the bright grains present in the CT slice. A circular pyrite body may be a pyrite-filled *Tasmanites* algal cyst (Fig. 48).

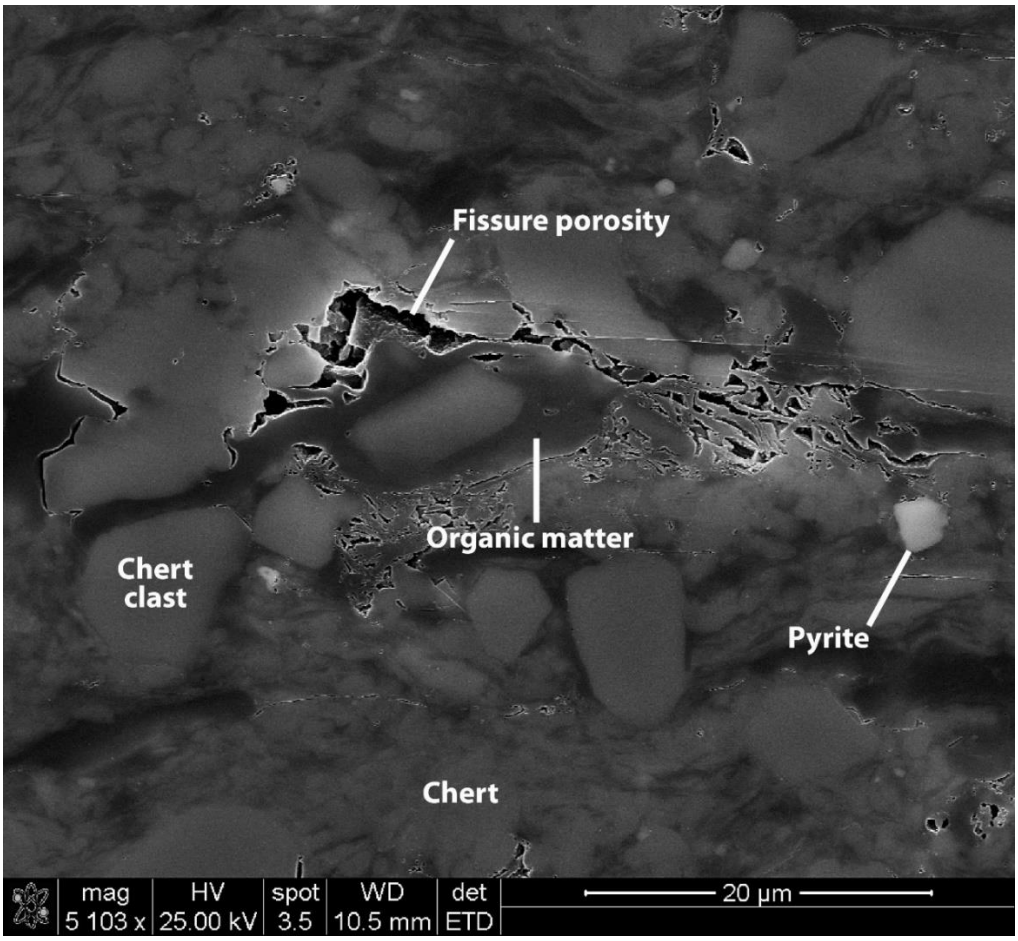

Figure 46. SEM ETD image of pores from an argon ion milled sample of Woodford chert, Hall 2B core, 6,178.5 ft. Fissure porosity in organic matter along the boundaries of some chert particles.

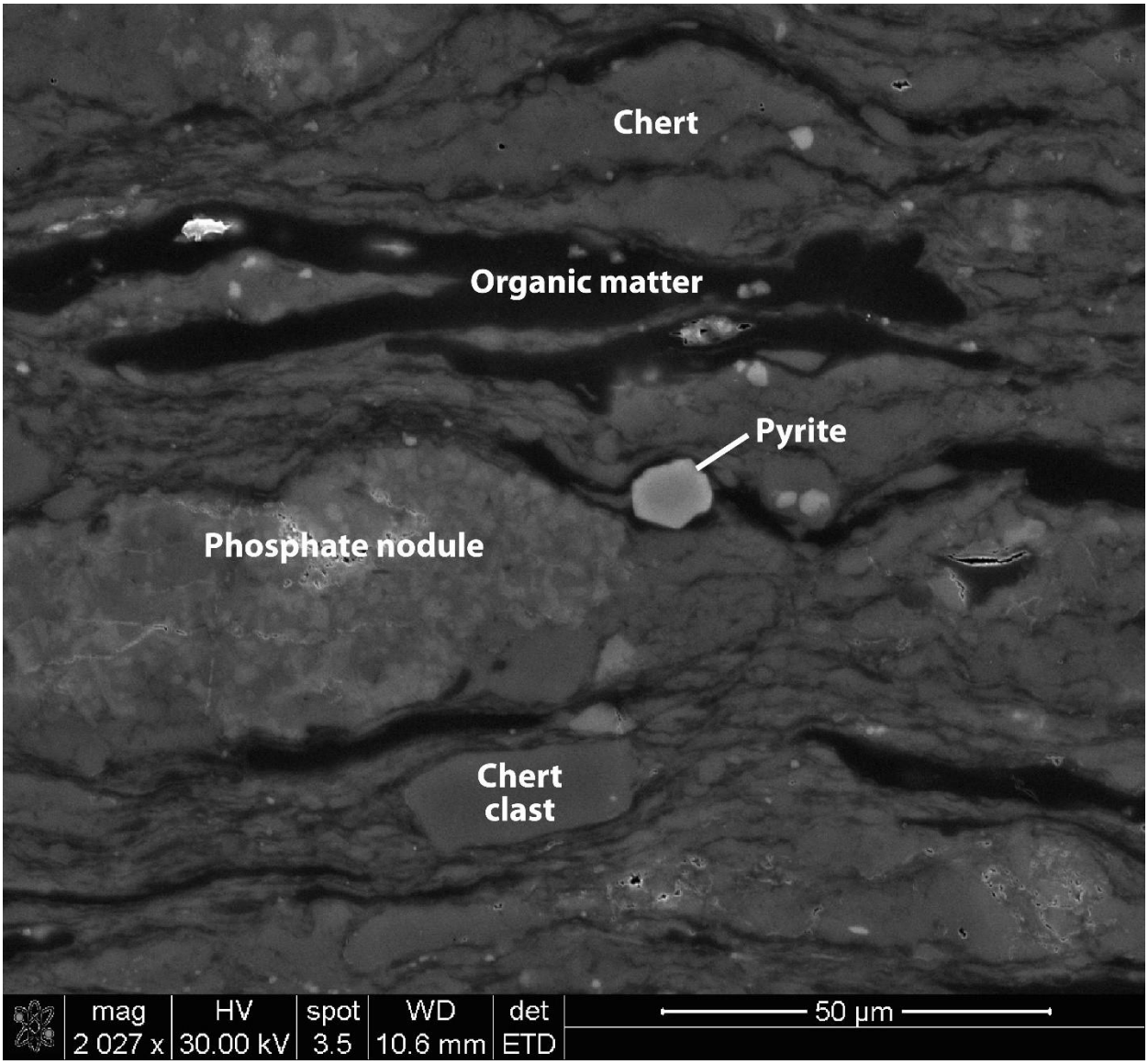

Figure 47. SEM ETD image of microfabric from an argon ion milled sample of Woodford chert, Hall 2B core, 6,178.5 ft. The sample consists of chert and organic matter. A pyrite body and phosphate nodule with peloidal texture are also present.

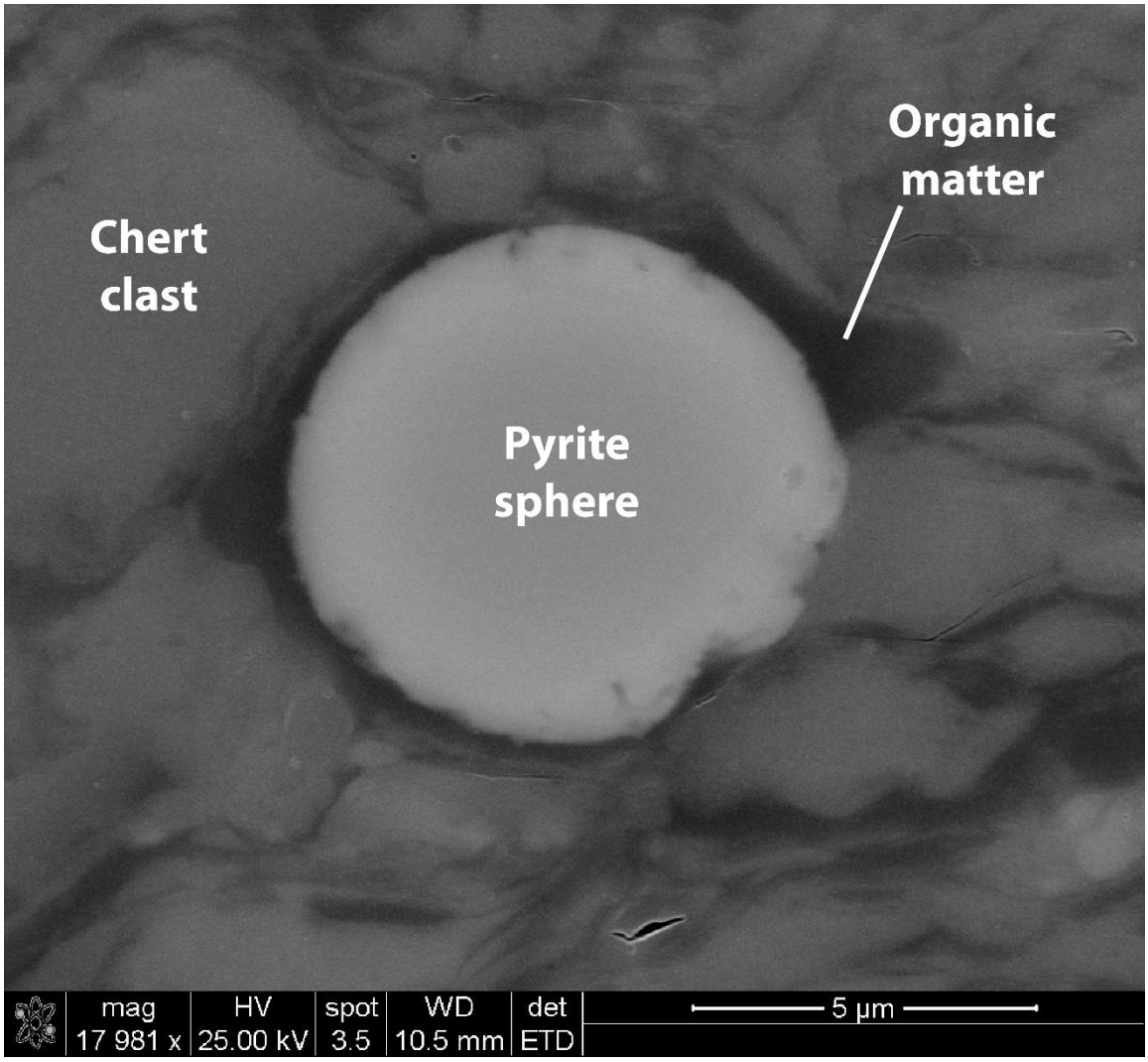

Figure 48. SEM ETD image of pyrite from an argon ion milled sample of Woodford chert, Hall 2B core, 6,178.5 ft. Pyrite-filled microfossil (*Tasmanites*?) in a matrix of organic matter and chert.

IV. 4 Floyd tongue of the Bangor Limestone; Walker core

The Floyd tongue of the Bangor Limestone is a Late Mississippian calcareous mudstone unit in the Black Warrior Basin that occurs between the Hartselle Sandstone and the main body of the Bangor Limestone (Thomas, 1972). The Hartselle was deposited in beach-barrier environments, whereas the Bangor represents an ooid shoal-rimmed carbonate ramp (Scott, 1978;

Thomas and Mack, 1982; Pashin, 1993). The Floyd tongue is an exceptionally fossiliferous mudstone unit that was deposited following marine inundation of the Hartselle strandplain. A sample from a core in Walker County, Alabama was scanned to explore the possibility of imaging calcareous fossils, which in this core include crinoids, articulate brachiopods, and fenestrate bryozoa (Fig. 49). CT slices of the core sample in the XY plane allow for rapid fossil identification and supplement fossil determinations made visually from the slabbed core (Fig. 50). Bryozoan fronds are readily identified by viewing them in the XY plane.

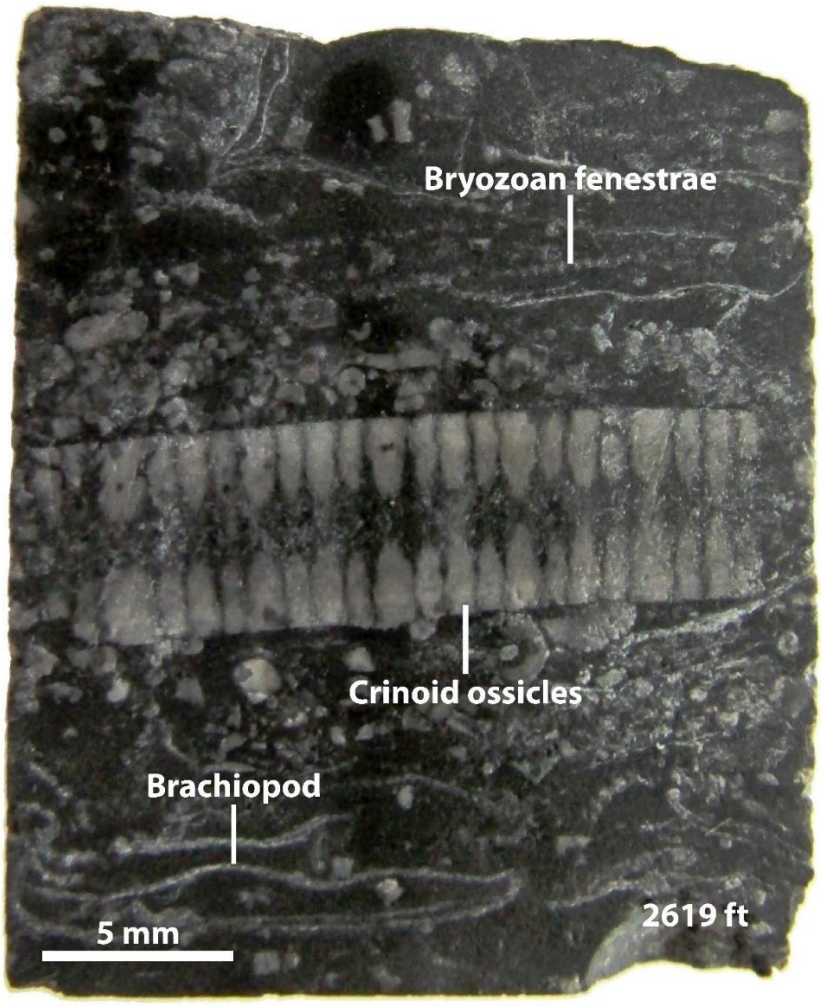

Figure 49. Photograph of fossiliferous mudstone (argillaceous rudstone), Floyd Tongue of the Bangor Limestone, Walker core, 2,619 ft.

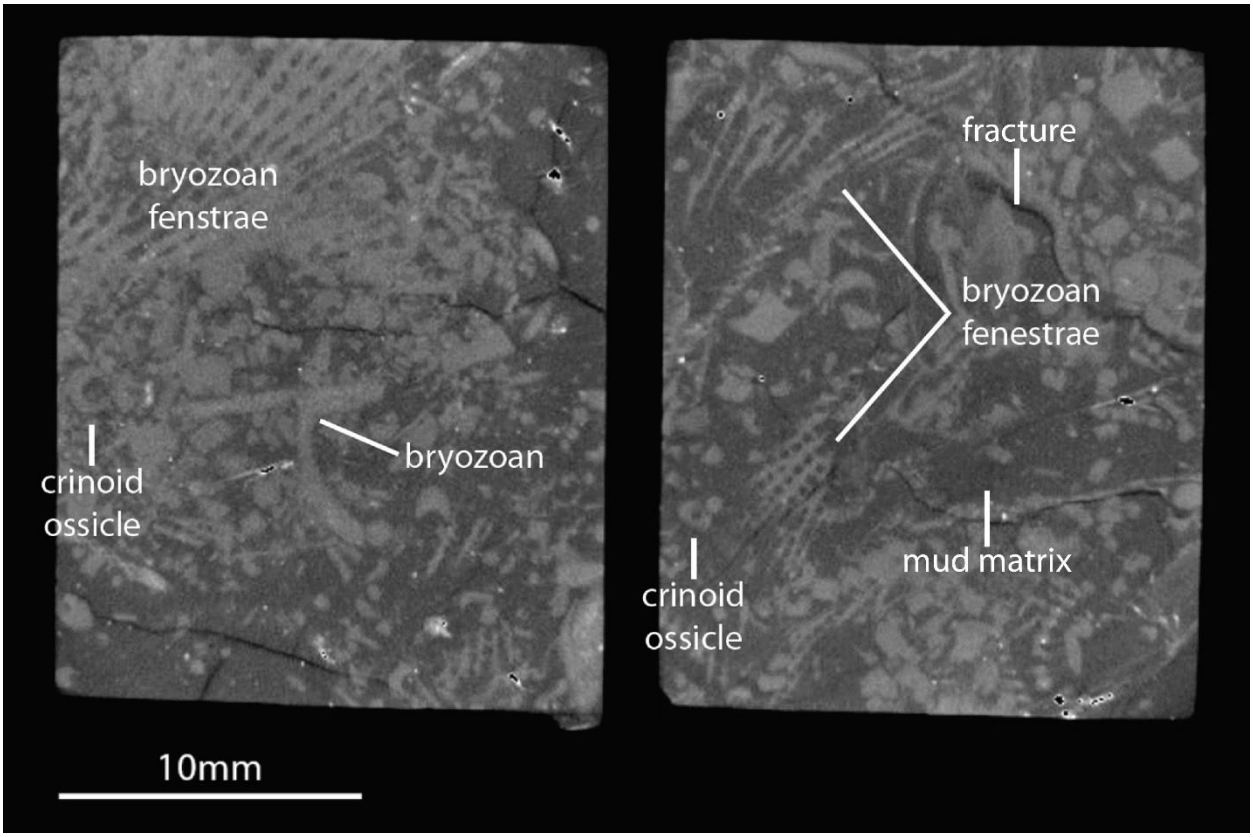

Figure 50. CT slices of fossils in the XY plane, Walker core, 2,619 ft. Fenestrate bryozoa and crinoid ossicles are easily identified. In addition to fossils, irregular fractures and the mud matrix are imaged. Black areas that appear to be pores are high density material (pyrite) that was poorly imaged because of unresolved reconstruction errors.

Fossils were imaged in three dimensions by using XM3DViewer to extract 1mm-thick sections of the tomograph parallel to bedding. After a portion was cropped, a density filter was applied in order to exclude lower density rock matrix from the image, thereby isolating the fossiliferous material. Three different slices were extracted and filtered to exclude rock matrix (Fig. 51). The extracted 1 mm slabs were superior to simple CT slices for viewing fossils, because bryozoan fronds and brachiopod shells were not completely flattened during burial and compaction. Indeed, the amount of fossil material and the level of detail imaged is greatly enhanced when 3D slices of the rock are extracted from tomographs.

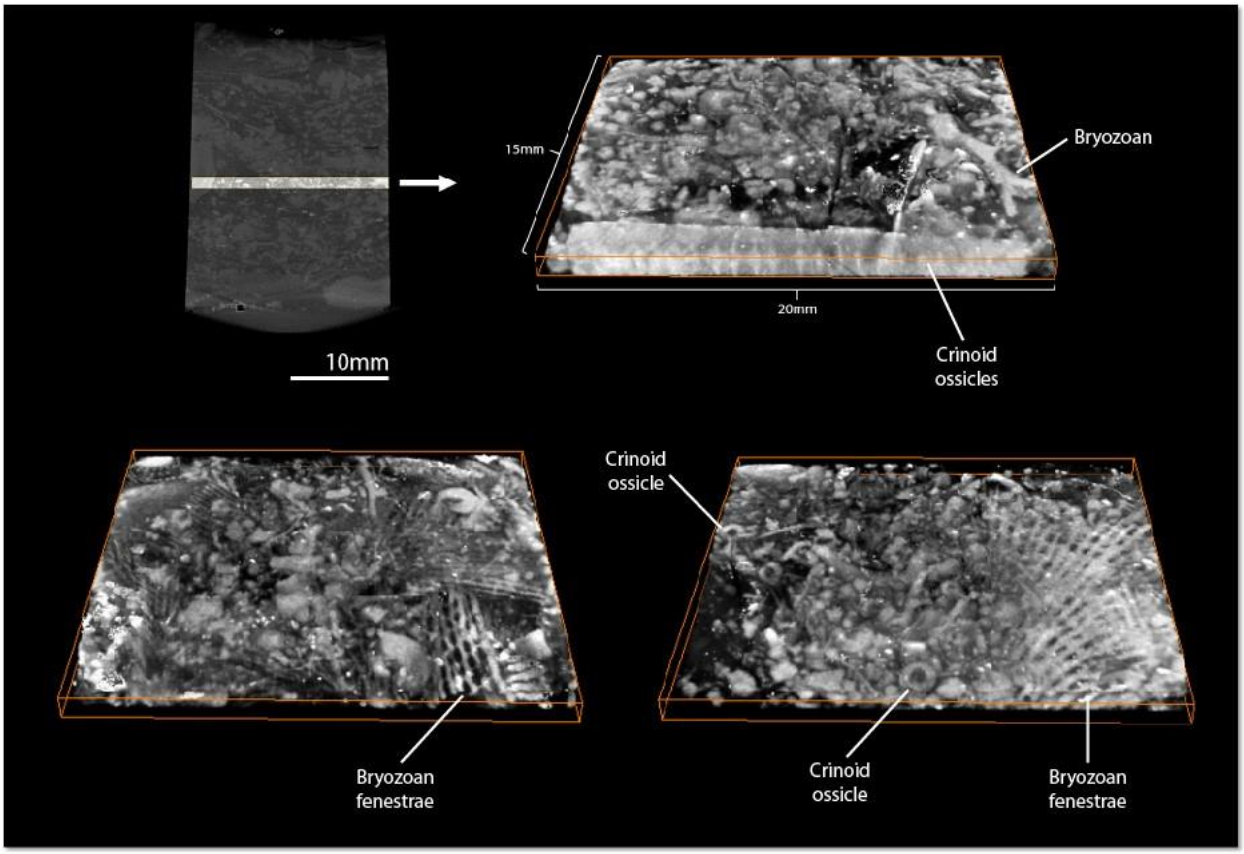

Figure 51. Three gray ramp density filtered cropped tomographsof fossils, Walker core, 2,619 ft. The tomograph has been cropped to reveal bryozoans and crinoids in three dimensions. This demonstrates the utility of the micro-CT as a tool for paleontologic and taphonomic analysis.

IV. 5 Pottsville Formation; Gorgas no. 1 core

The Pottsville Formation is Early Pennsylvanian stratigraphic unit in the Black Warrior foreland basin that was deposited in response to Appalachian-Ouachita orogenesis (Thomas, 1988). The Alabama Pottsville is composed of high frequency (Milankovitch band) transgressive-regressive cycles in which marine mudstone coarsens upward into sandstone that is overlain by an economic coal zone (e.g., Pashin, 1994, 2004; Pashin and Gastaldo, 2009). The Pottsville is a strategic source of metallurgical coal and is the birthplace of the modern coalbed methane industry; the formation also contains conventional sandstone reservoirs.

The Gorgas no. 1 core comes from an exploratory borehole that was drilled to assess CO_2 storage options at a major coal-fired power plant in Walker County, Alabama (Clark et al., 2013). The sample that was CT scanned comes from a coarsening-upward shale-siltstone interval in the Fayette depositional cycle, which is near the top of the lower Pottsville Formation and was deposited in distal delta front to prodeltaic environments (Pashin, 1994; Clark et al., 2013). A photograph of the scanned sample shows quartz silt and argillaceous laminae, as well as bioturbation (Fig. 52). The tomograph reveals several sedimentary structures, including silt and mud laminae, current ripple cross-laminae, and bioturbation (Fig. 53).

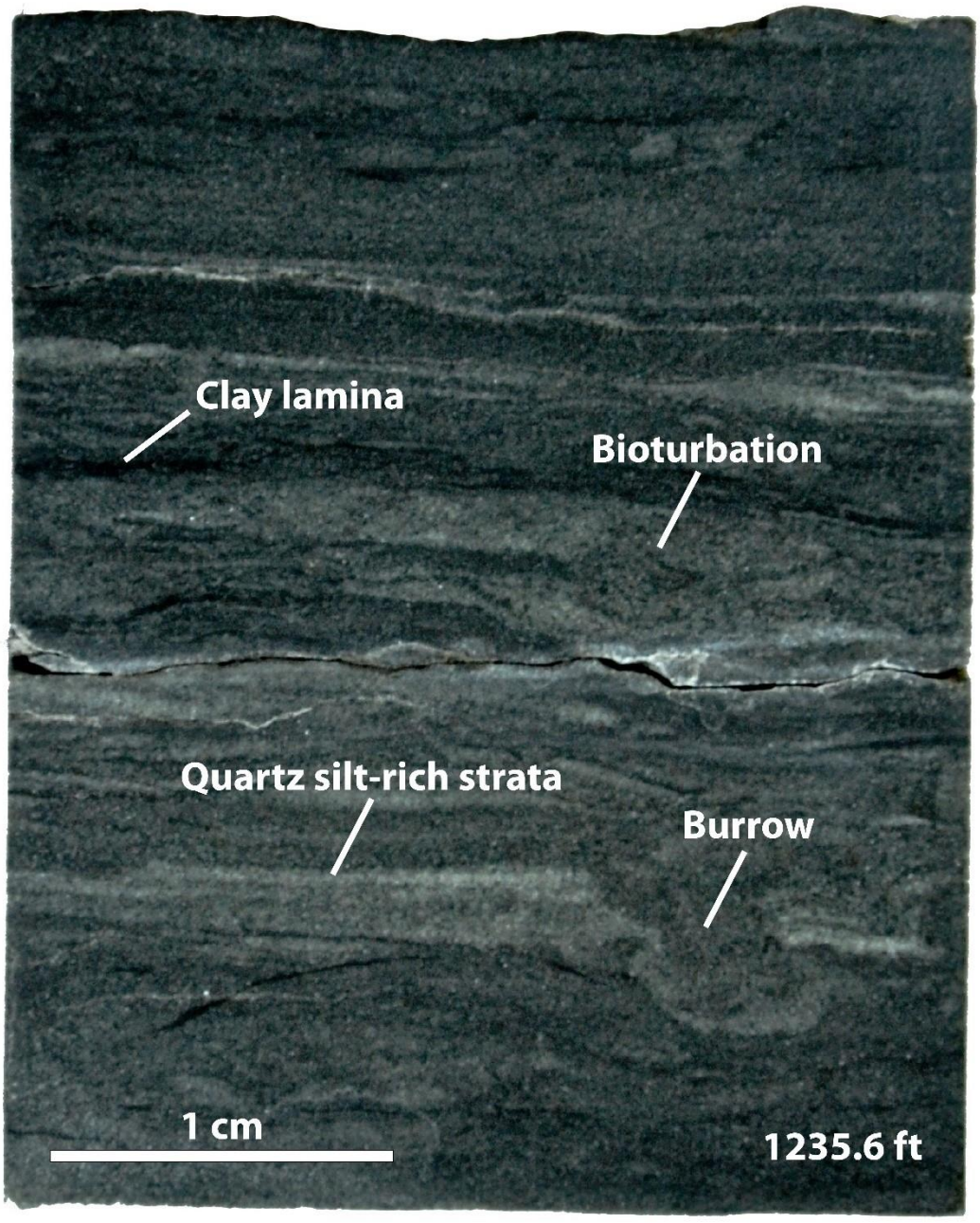

Figure 52. Photograph of a Pottsville shale-siltstone sample, Gorgas no. 1 core, 1,235.6 ft.

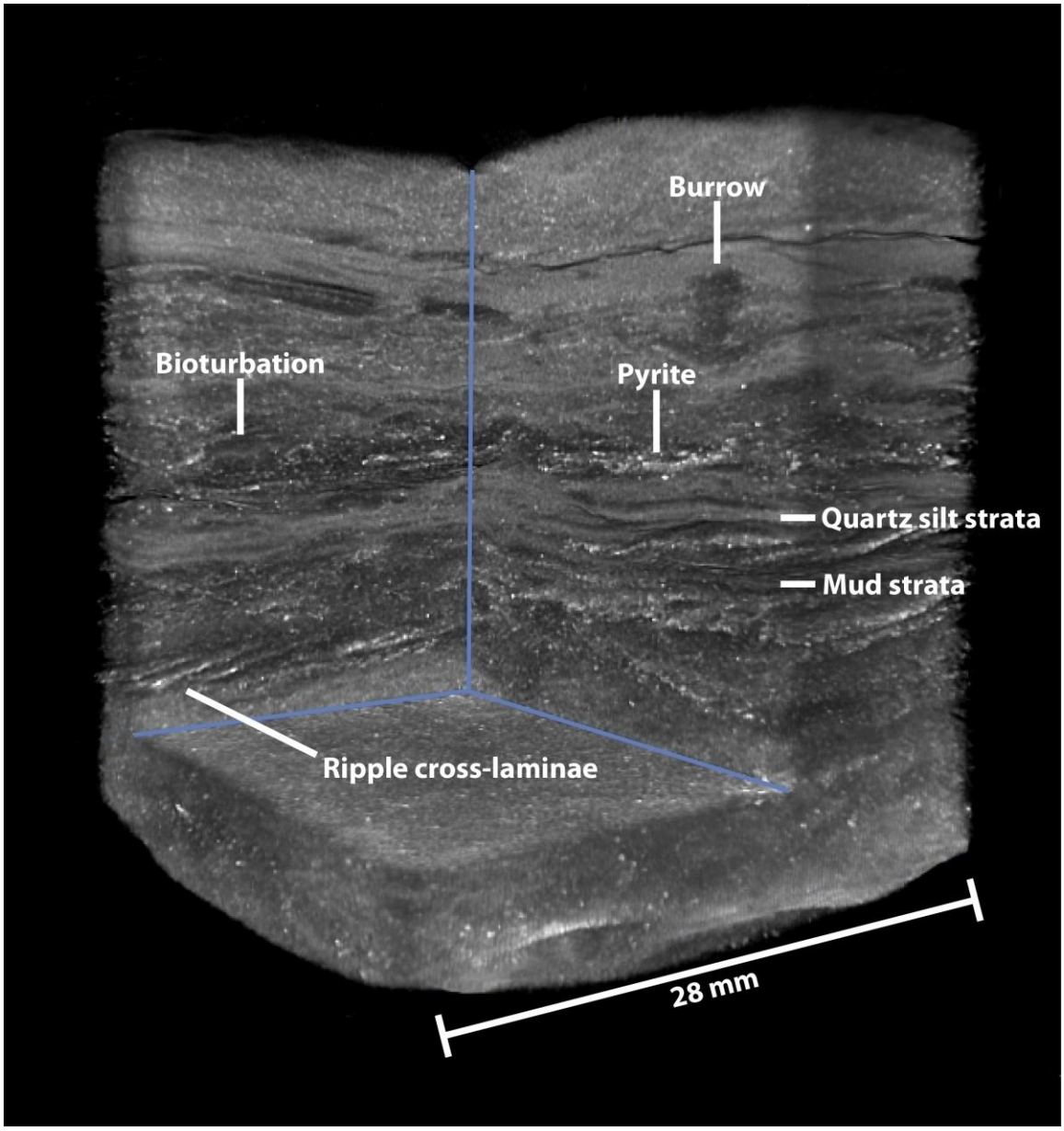

Figure 53. Gray ramp density filtered cropped tomograph showing silt and mud laminae, current ripple cross-laminae, and bioturbation, Gorgas no. 1 core, 1,235.6 ft.

A general knowledge of the composition of the sample from XRD analysis, coupled with the gray scale derived from the CT histogram, allowed for a simple semi-quantitative analysis to be performed using ImageJ software. The CT data include 1,004 slices, but only the central portions of 574 of the slices were used in order to eliminate edge effects (Fig. 54). Histograms of

the gray scales for all the slices were stacked, and gray scale cutoffs were manually applied to separate the constituents. Four constituent phases were defined based on the gray scale data, and these phases include fractures, argillaceous mud, quartz silt, and pyrite. Using the gray-scale ranges assigned to each constituent enabled volumetric percentages to be determined. This quick-look determination method resulted in volumetric percentages of 1.9% fracture fill and porosity, 29.6% clay, 67.2% quartz and 1.3% pyrite (Fig. 55). It is important to note that the precision for this sort of volumetric analysis is a function of the voxel resolution, which undoubtedly caused intermixing of clay and quartz silt, and the accuracy is based on observational bias.

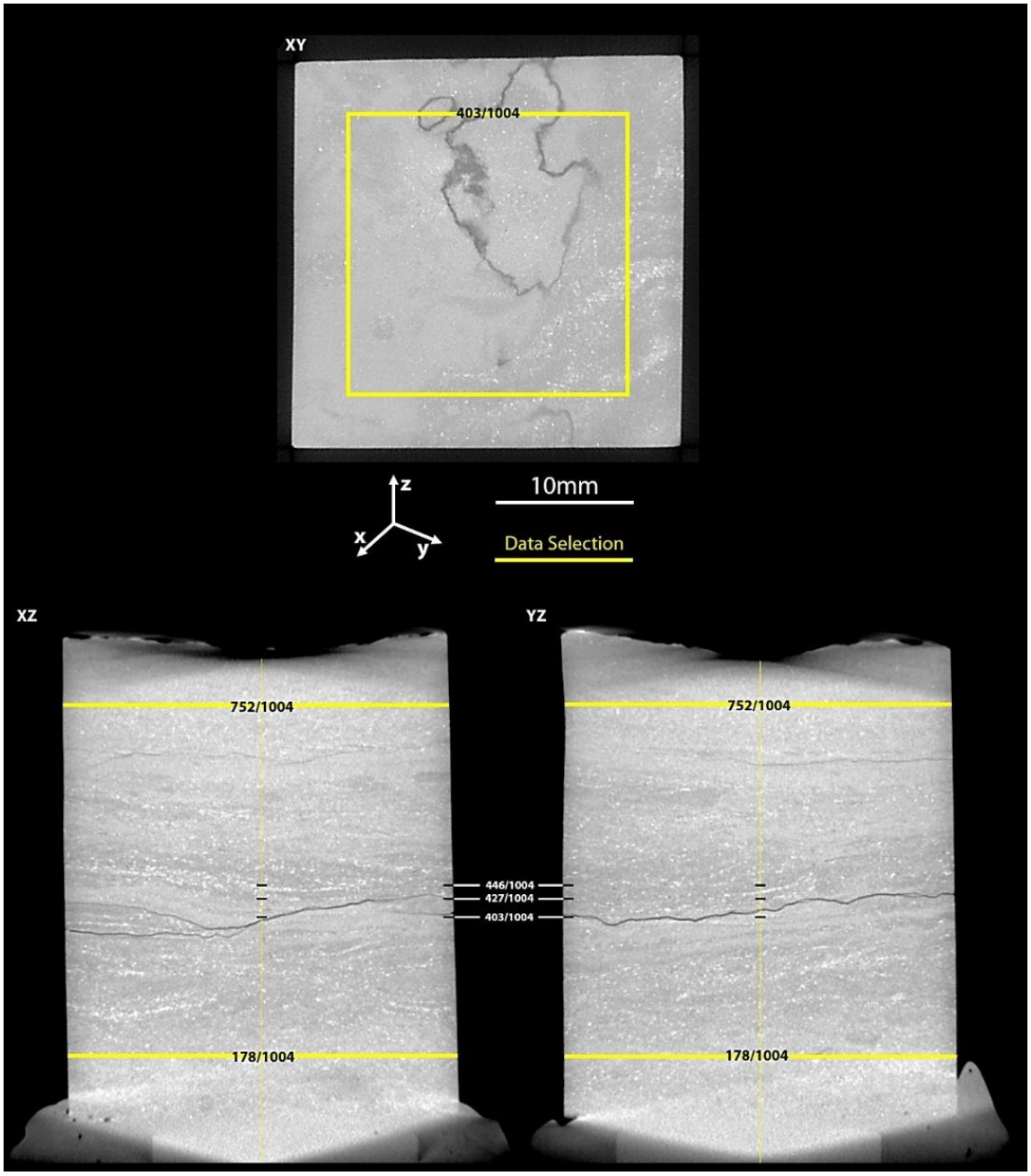

Figure 54. CT slices of the Gorgas no. 1 core sample, 1,235.6 ft. Yellow lines define the limits of the data volume that was selected for calculating volumetric percentages.

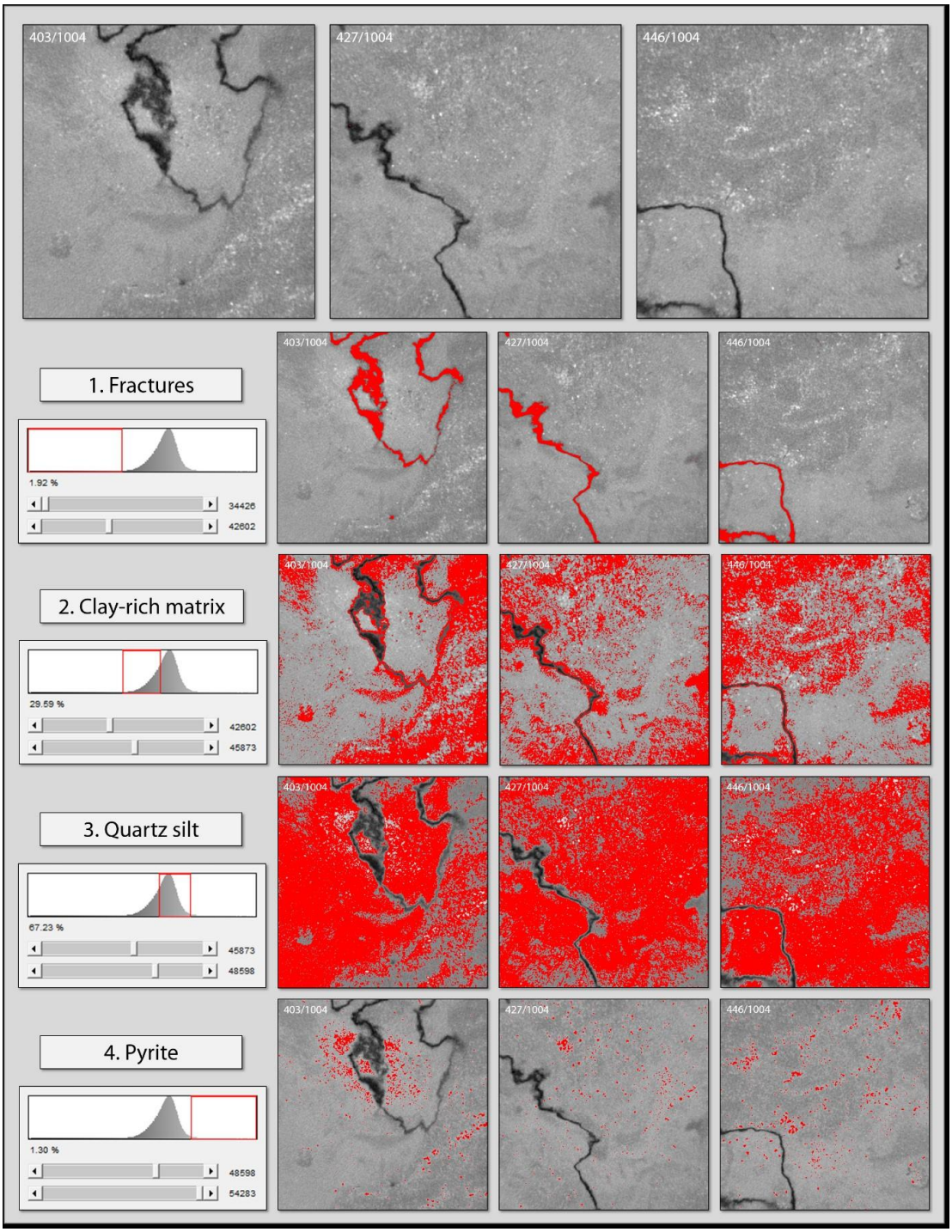

Figure 55. Analysis used to determine volumetric percentages of fracture space, argillacous mud, quartz silt, and pyrite in a Pottsville shale-siltstone sample from the Gorgas no. 1 core. The tomograph was segmented using gray-scale histogram cutoffs to identify major sample constituents.

Microfabric and compositional analysis on an argon ion milled portion of the sample via SEM/EDS provides information on the sample that aids in interpretations of the tomograph (Fig. 56). The pyrite is framboidal, and a mixture of clay and silica comprises the matrix material. A large piece of cuticular organic matter and fracture slit pores with nanometer-scale apertures are imaged within the siliceous matrix. The bright mineral in the organic matter is pyrite. Porosity is also found between the contact of a quartz grain and its surrounding siliceous matrix (Fig. 57). An intragranular pore, measuring 6 μm wide and 10 μm in length, was also imaged in a quartz grain (Fig. 58).

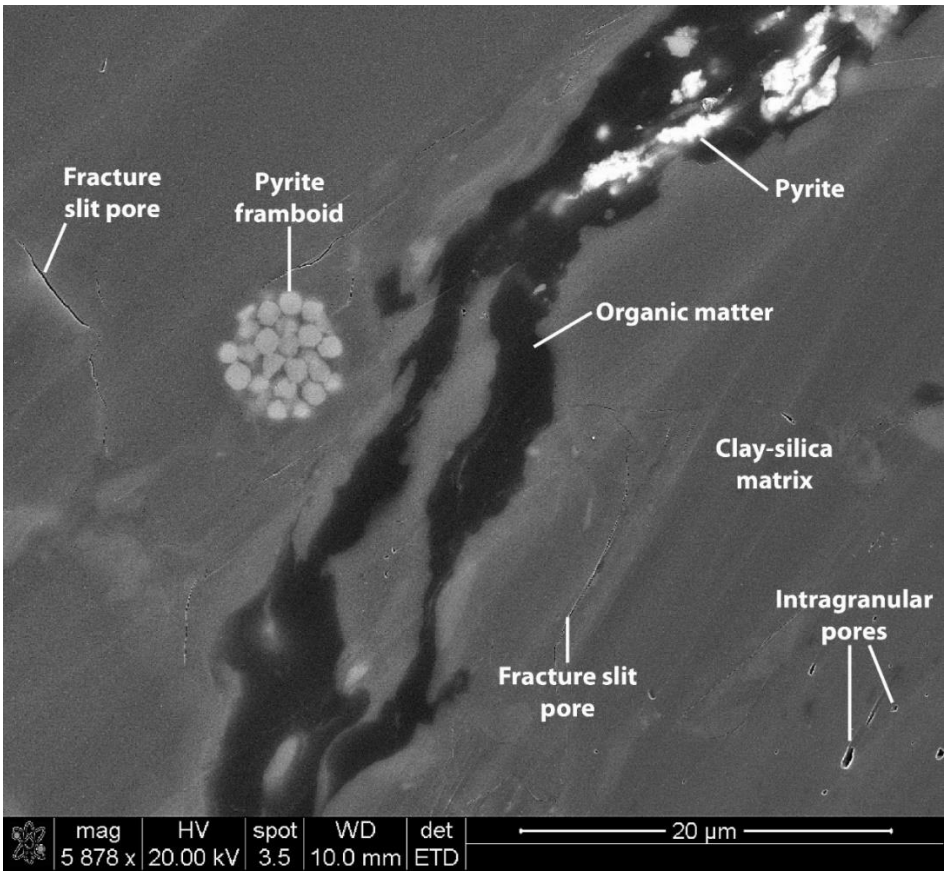

Figure 56. SEM ETD image of microfabric from an argon ion milled sample of Pottsville Formation in the Gorgas no. 1 core, 1,235.6 ft. Porosity is mainly in fracture slits, sulfide morphology is framboidal, organic matter is present and the matrix is a mixture of clay and silica. The bright material in the organic material is pyrite.

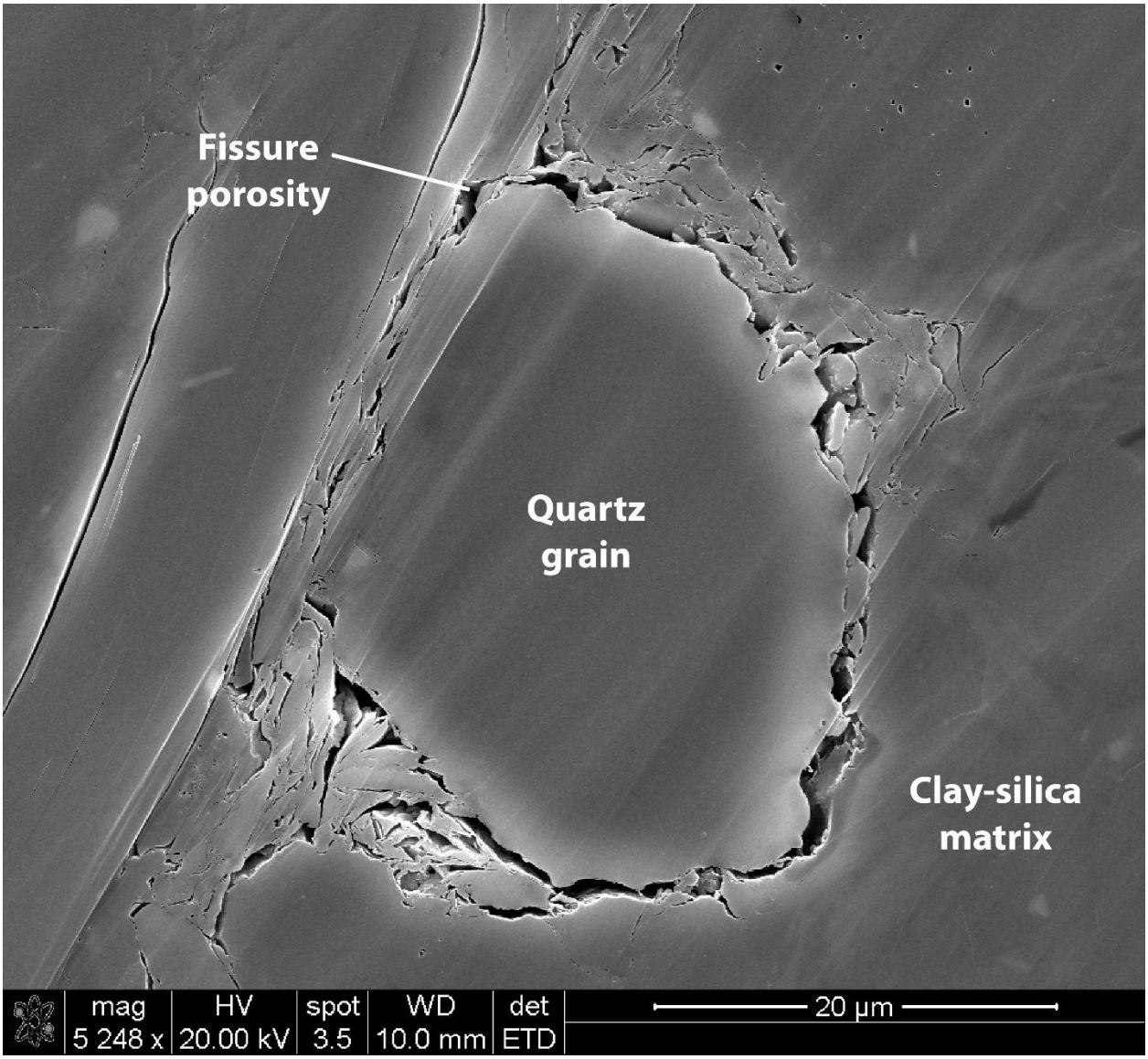

Figure 57. SEM ETD image of pores from an argon ion milled sample of Pottsville Formation in the Gorgas no. 1 core, 1,235.6 ft. Porosity appears as partially annealed fracture slit pores between a quartz silt grain and the surrounding silica-clay matrix. Porosity likely follows the grain because of desiccation of the surrounding matrix material after core recovery or matrix shrinkage during thermal maturation.

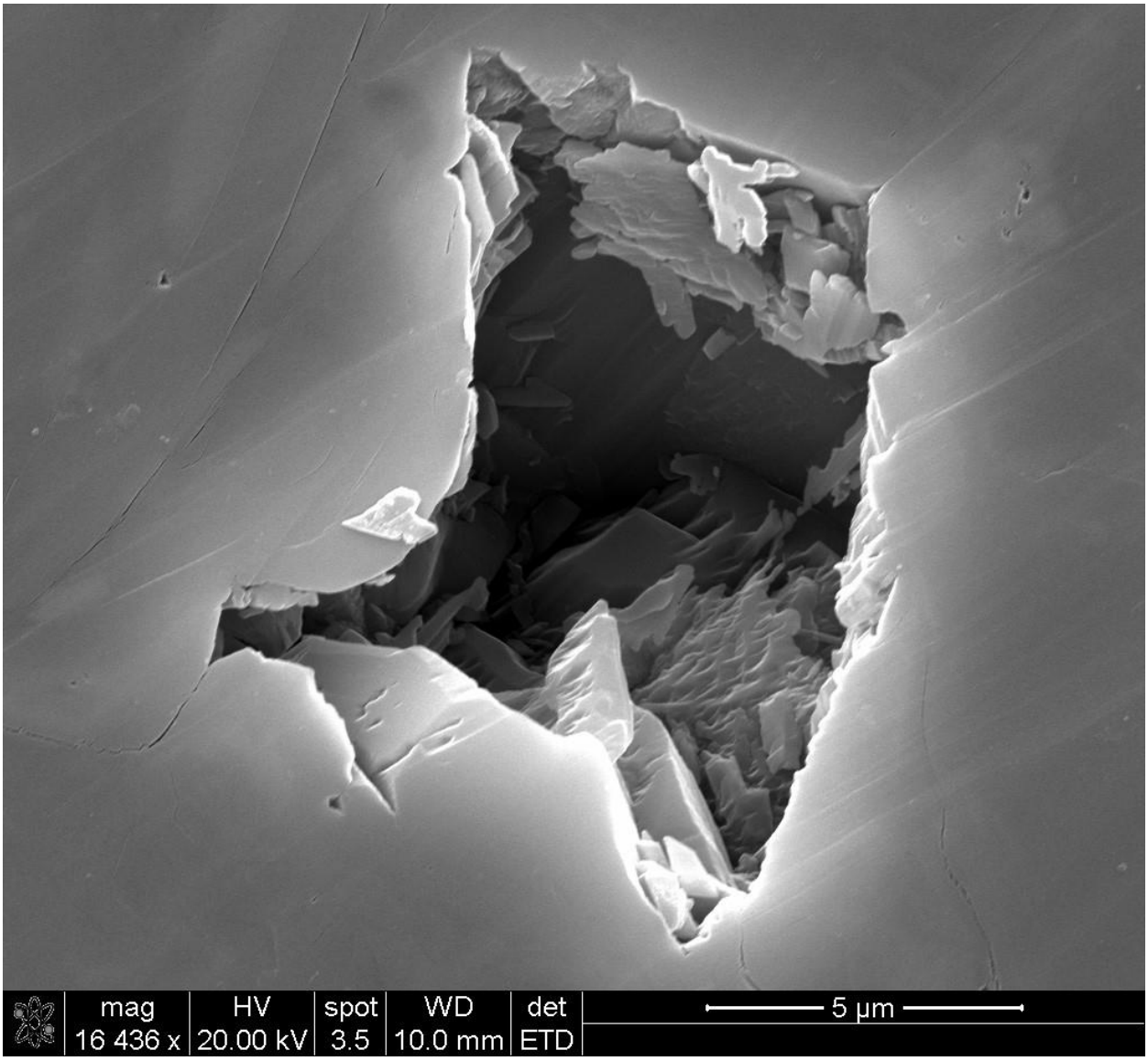

Figure 58. SEM ETD image of a pore from an argon ion milled sample of Pottsville Formation, Gorgas no. 1 core, 1,235.6 ft. Intragranular pore, measuring 6 µm wide and 10 µm in length, imaged in a quartz grain.

After observing this relatively large pore in a quartz grain, a CT scan was performed on a very small subsample from the Gorgas core to determine how well porosity could be imaged at the resolution limits of the scanner. The sample measures 0.3 mm in height, 0.2 mm in width and 0.2 mm in thickness, and was the smallest sample CT scanned in this thesis work (Fig. 59). It

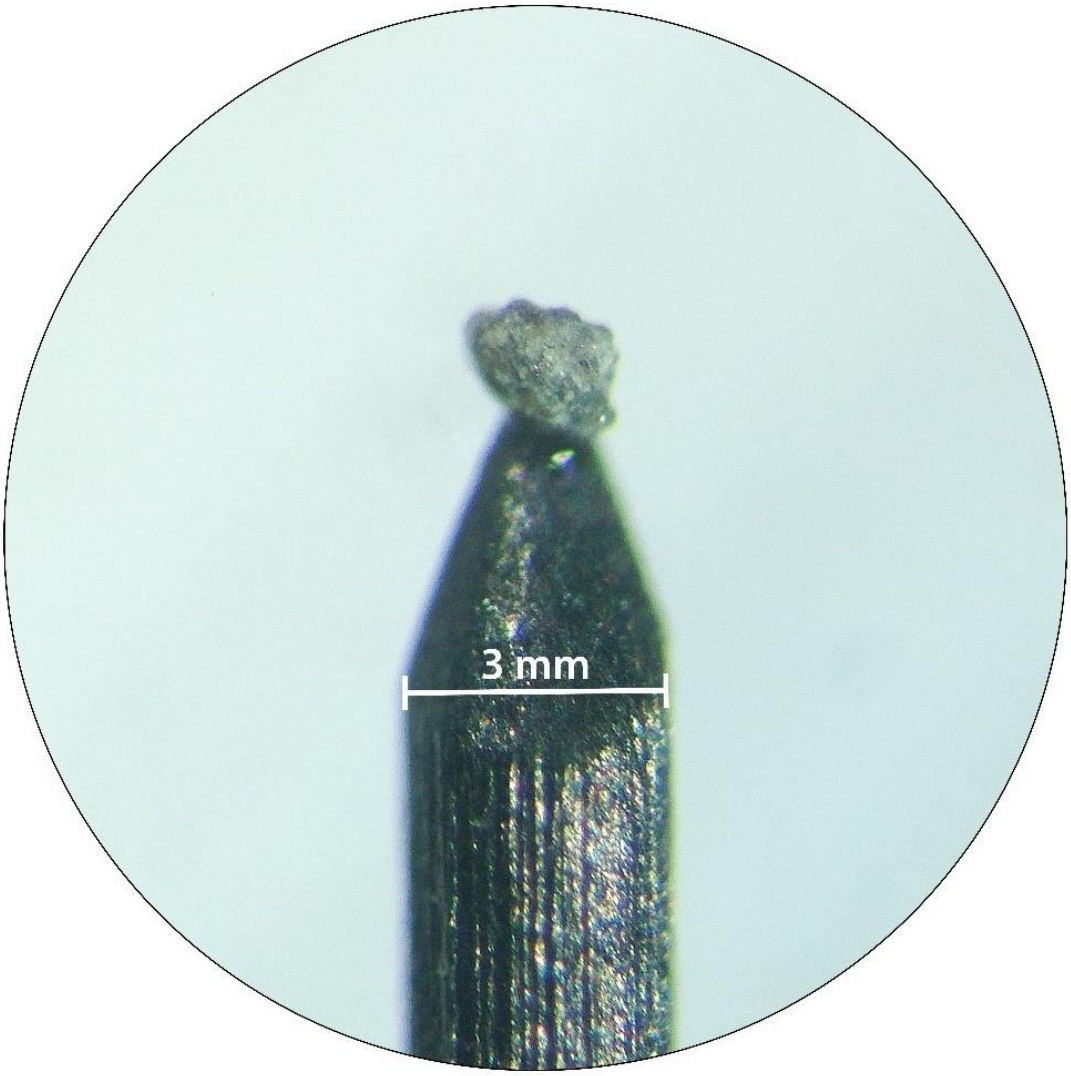

Figure 59. Photograph of a tiny Gorgas no. 1 core sample under a binocular microscope. The sample measures 0.3 mm in height, 0.2 mm in width and 0.2 mm thick. The sample was mounted on a sharpened piece of 3 mm graphite pencil lead and fixed using five-minute epoxy.

was scanned for 13 hours and 19 minutes for maximum image quality. While the tomograph for the sample proved to be an excellent observational tool for porosity, the smallest resolvable pore appeared to have a diameter of 3 μm (Fig. 60). Another important consideration is that to obtain a sample this small it must be cut or chipped away from the larger rock and in doing so, fractures or other void space may have been created during sample preparation. Nevertheless, the

tomograph does image the types of porosity identified in the SEM images. In addition, the tomograph gives you a larger field of view than SEM and allows you to see more of the samples microfabric. While CT does appear to be a good qualitative tool for observing aspects of porosity, performing quantitative volumetric calculations for the porosity poses a problem because the gray values for the pores match many of the other gray values observed in the clay portion of the matrix. In addition, significant potential for widening existing fractures or introducing new fractures during preparation of a broken rock sample of this size is high. The circular pyrite body observed from the CT slice appears to be a framboid, as it matches the 10 μm diameter of a framboid seen from an SEM image of the sample (Fig. 56).

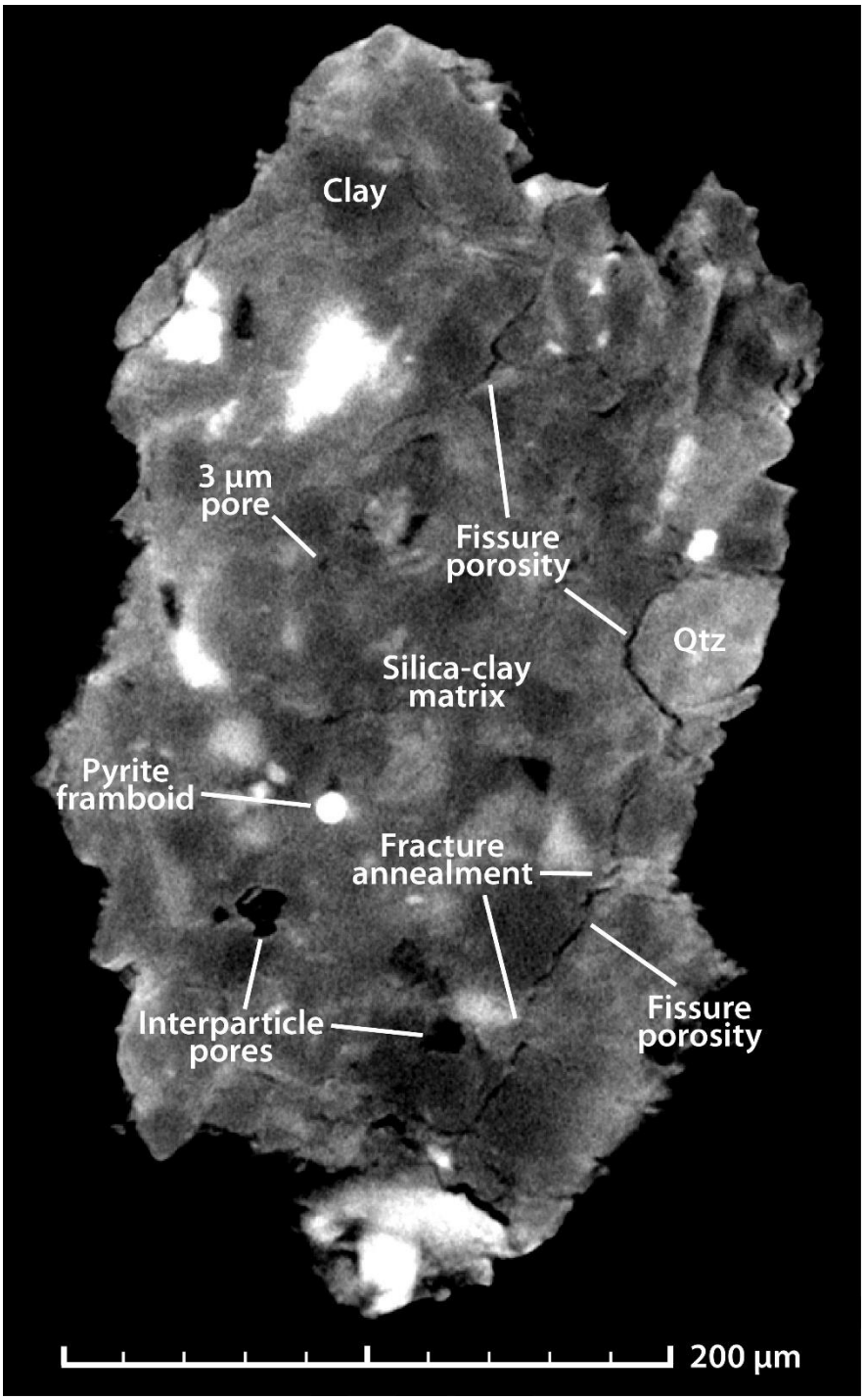

Figure 60. CT slice of a Gorgas no. 1 core sample showing microfabric. Porosity types imaged are fissure and interparticle porosity, with the smallest resolvable pore measuring 3 µm in diameter. Porosity was identified by the true black gray value assigned to it. Mineral constituents include quartz grains and pyrite bodies in a clay-silica matrix.

CHAPTER V

DISCUSSION

Throughout this study, several lessons were learned not only about the utility of micro-CT scanning for geologic investigations, but also operational considerations relating to imaging resolution, scanning arifacts, sample size and sample composition.

V. 1 Sample size

Results demonstrate that sample size is a crucial consideration for scan quality when using the micro-CT scanner. While whole core samples can be scanned, only a small volume within the actual sample can be imaged. That volume measures 5 cm in height, 4 cm wide and 4 cm thick, and the material that doesn't fit inside that sample volume window only serves to attenuate the x-ray beam and lower the contrast of the scan. In addition, the scanning of a volume within a whole core requires maximum x-ray energy (150 kV) to penetrate all of the material. This, too, lowers the contrast of the scan.

V. 2 Scanning artifacts

Another problem with scanning large samples is beam hardening, which causes the edges of an object to appear brighter than the center, even if the material is internally homogeneous. All of these problems were experienced when scanning the Lamb core (Fig. 11). Beam hardening artifacts are found throughout the sample, and mineral constituents other than pyrite are difficult

to differentiate due to low contrast of the scan. Scan time can be greatly reduced by using small samples, and the resolution of the resulting tomograph is much higher. In addition, contrast is higher in small samples because there is less material to penetrate. Moreover, less x-ray energy is required to scan small samples. While smaller samples will yield high resolution and high contrast scans, the best strategy is to tailor sample size to the scale of what is desired to be imaged.

Partial volume effects, which occur when a voxel volume comprises more than one constituent is another x-ray artifact that is important to consider. Unlike beam hardening, partial volume effects can actually enhance the quality of an image by highlighting features, like microfractures, that are below the voxel resolution of the scan (Fig. 37). However, the downside to this effect is that it can lead to erroneous volumetric determinations involving objects at the sub-voxel scale. Micron-scale mineral grains also are hard to image, and particles need to occupy many voxels to avoid blurry edges.

V. 3 Sample composition

While sample size and scanning artifacts are important considerations for CT scanning, density contrast must be present in order for sample features to be imaged. This may prove to be problematic for CT studies of rock types with low density variablity, like some nonporous carbonate and evaporite rocks. Adequate density contrast within a sample opens the door for several applications. If compositional data are available, a semi-quantitative operation can be performed to calculate the volumetric percentage of the known constituents by segmenting scans via gray value histogram cutoffs (Fig. 55). While this is a quick-look method for determining percent composition, it is possible to arrive at more precise volumes via the marriage of CT and EDS map datasets using a method called TACCo (Tomography Assisted Chemical Correlation) (Hu et al., 2014). Also, volumetric percentages can be converted to weight percent and molar

fractions so that geochemical analysis can be performed. Segmentation of gray values also enables the user to isolate and inspect features of similar density (Figs. 26, 51). However, it is important to note that even if a feature is resolvable, it must have a distinctive gray value to be segmented. This hindrance was encountered when calculating the percentage of fracture porosity in the Hall 2B core (Fig. 40). While hairline fractures below the voxel resolution were imaged, the gray values in the corresponding CT voxels were an average of the fractures and surrounding material. This caused the gray values for the hairline fractures to be brighter than the other fractures. As a result, the gray values for the hairline fractures matched the values for some of the matrix material so they couldn't be included in the volumetric calculation.

V. 4 Imaging resolution

The maximum voxel resolution of the CT scanner used in this study is 100 nm. In order to obtain that resolution while maintaining an adequate density contrast, you must have a sample that is approximately 0.2 mm in height, 0.1 mm wide and 0.1 mm thick. However, preparing a geologic specimen with those dimensions is likely going to sacrifice the integrity of the sample. A more realistic maximum voxel resolution for a geologic sample, while upholding the integrity of the specimen, is approximately 500 nm and this was demonstrated when scanning a sample from the Gorgas core (Fig. 60). While this gets close to the resolution of a typical SEM image, the image quality of a CT slice at maximum resolution is nowhere near that of an SEM micrograph due to the blurry edges caused by partial volume effects. As a result, the smallest pore diameter that can be resolved is approximately 3 μm.

V. 5 Rock fabric

Micro-scale observations of rock fabric were made in several samples. The simplest observation made from the CT scans was the recognition of dense mineral grains because of their bright appearance, which reflects a high degree of x-ray attenuation. Dense minerals that were

imaged included pyrite, quartz, carbonate and phosphate. The most common dense grains in the shale samples analyzed during this study are pyrite and detrital quartz. These minerals commonly occur at micro-scale, as shown from a tomograph and CT slices from a Lamb core sample (Fig. 17). While dense minerals are easily observed, they are difficult to differentiate because of the similar gray values assigned to them by the imaging software, as well as variability of x-ray signature related to position in the sample, particle size, and particle shape. Grain shape, size, roundness and sorting were also observable from the some of the CT scans (Figs. 17, 37). Recognition of a bladed sulfide morphology in a scan of a Woodford Shale sample allowed for identification of marcasite, which is the orthorhombic polymorph of FeS (Fig. 26). In another Woodford Shale sample, constituents of a lag bed were identified by cycling through CT slices of the sample (Fig. 29). In addition to dense mineral grains, clay matrix was readily observed due to its lower density. It also appears that imaging of organic matter may be possible (Fig. 17). In several cases, pore types were identified in CT slices (Figs. 24, 37, 60). Volumetrics for fracture pores were also calculable from one of the Hall core samples, although some fractures below the resolution limit of the instrument were not included in the calculation (Fig. 40). Zeiss does have another CT instrument, the XRadia VersaRXM 510, that has a maximum voxel resolution of 70 nm that could modestly improve volumetric calculations of porosity.

V. 6 Sedimentary structures

Physical sedimentary structures are also recognizable where density contrast is present. Throughout the course of this thesis work, several physical structures were discerned with CT scans. Ripple-cross laminae was imaged in a sample from the Pottsville Formation (Fig. 53). In several cases, alternating mud and silt laminae were observed (e.g., Figs. 13, 21). In one tomograph, fine laminae that were otherwise invisible were observed, apparently due to variation of clay and silica content (Figs. 32, 33). Considering the limitation of sample size for the instrument that was used, physical structures larger than a few centimeters, such as large scale

cross-strata, are not good candidates for imaging. Other physical structures that might fall within the size limitations and be worth imaging include sole marks, graded bedding, flaser and lenticular bedding, and irregular stratification like convolute bedding and flame structures. Considering that physical structures are excellent indicators of sedimentary processes and depositional environments, the use of micro-CT scanning for future sedimentological studies may increase.

In addition to physical structures, several biogenic sedimentary structures were imaged with micro-CT scanning in this study. A horizontal burrow network filled with dense material was observed within a mud-rich nodule in a sample of Conasauga Shale (Fig. 8). The burrows are invisible to the naked eye, even in an enlarged photograph of the sample (Fig. 8). In a sample from the Pottsville Formation, a variety of trace fossils were discerned (Fig. 53). Other biogenic structures worth imaging include trace-fossil associations (e.g., *Skolithos*, *Cruziana*, *Zoophycos* and *Nereites*), tracks and trails.

V. 7 Body fossils

Furthermore, the ability to image body fossils in detail was demonstrated with this work. Accurate identification of fossils in core slabs can often be a difficult task because one commonly sees only a cross-sectional or bedding plane view of the specimen. One of the advantages that CT scanning of rocks provides is the ability to view slices of the rock that are parallel, perpendicular, or even oblique to bedding. By looking parallel to bedding planes, flattened fossils are more readily recognized (Fig. 50). Fossil assemblages can also be viewed by cropping thicker slices from a tomograph and filtering out the lower density phases, leaving only the fossils (Fig. 51). It is important to note that CT scanning has proven itself to be just as effective for imaging low-density fossils, such as carbonized plants (Kvale, 2014). The potential to image biogenic structures and non-destructively extract a high resolution 3-D image of a fossil from the interior

of a rock sample has innumerable applications to systematic paleontology, taphonomy and paleoecology.

V. 8 Diagenetic features

CT scanning also proved useful for imaging diagenetic features. The most common diagenetic sedimentary structures in shaly sequences are concretionary (e.g. nodules) (Potter and Pryor, 1980). The study of phosphate nodules, in particular, has been used to evaluate conditions of formation and diagenetic evolution (Morad et al., 1994). Numerous phosphate nodules were imaged in a Woodford Shale sample from the Anderson core, and the ability to slice, filter, and density map enabled characterization of basic diagenetic relationships (Figs. 23, 24).

Pyrite is a common product of early diagenesis in organic-rich sediment (Berner, 1984; Taylor and Macquaker, 2000). Various pyrite morphologies and textural features have been used to infer geochemical and paleoenvironmental conditions (Schieber and Baird, 2001; Passier et al., 1997). Pyrite, in various forms, was imaged with the CT scanner and SEM in every sample analyzed (e.g., Figs. 11, 13, 26).

Other diagenetic features imaged with the CT unit include partially and fully-cemented fractures (Figs. 21, 35) and pores. Interparticle, intraparticle and organic-matter pores in mudrocks form during all stages of mudrock diagenesis, from shallow to deep burial. While organic-matter pores were only imaged using SEM (Figs. 31, 46), interparticle pores were imaged with difficulty in a sample from the Gorgas core (Fig. 60), and the small sample size required for analysis makes the likelihood of damage of the pore system during sample preparation high. Intraparticle pores were also imaged within a phosphate nodule in a sample from the Anderson core (Fig. 24). Altogether, imaging of diagenetic structures with micro-CT was successful and could be added as another investigative approach to their systematic study.

V. 9 Fractures and faults

The CT scanner proved to be an excellent tool for the analysis of faulting and fracturing. The smallest resolvable fracture apertures observed from a CT scan ranged from 1 – 2 μm (Fig. 60). Smaller fracture apertures will undoubtedly be resolvable as micro-CT imaging resolution advances. CT scanning also revealed a partially mineralized, dipping fracture in a sample that was not observable from its photograph (Figs. 21, 20). It is important to note that mineralized fractures will only image if adequate density contrast exists between the vein fill and the rock matrix.

Both mineralized and open fractures were imaged from CT scanning a Hall core sample, and their cross-cutting relationships allowed for determining structural chronology (Fig. 37). Histogram cutoffs allowed for segmentation of various fracture types and enabled 3D renderings of fracture networks to be generated for visualization purposes (Fig. 38). When fracture porosity is resolvable, a volumetric calculation is also possible (Fig. 40). In addition to structural chronology and fracture composition, identification of fracture geometry and interconnectivity of fracture networks is another powerful use of CT scanning. Determination of fracture geometry and interconnectivity by only observing the sawn surface of a core can be a challenging task, but applying a density filter to a tomograph can alleviate those difficulties. A tomograph acquired for a Lamb core sample provides an excellent demonstration of the detailed fracture network observations that can be made (Fig. 19). Being able to peel a sample layer by layer is a great way to view the internal fabric of a rock and determine how fractures and faults interrelate. One of the Poe core samples is great example, and its cropped tomograph shows the high level of detail that can be obtained from a CT scan (Fig. 35).

CT analysis proves to be an excellent analytical tool for thorough examinations of heavily fractured and faulted samples. In addition to all of these uses for CT scanning fractures

and faults, other applications include, but are not limited to: measuring fracture abundance (density and intensity), analyzing the kinematic aperture of fractures, analyzing aperture and connectivity to characterize the storage and transmissivity of fracture networks, and extracting orientation data from fracture planes and plotting the results on stereonets, rose diagrams, and the like. As micro-CT imaging resolution evolves, it will improve facilitation of advanced structural characterization and interpretation.

V. 10 SEM/EDS

Observation of rock microfabric in a CT slice or tomograph is an effective way to identify areas to characterize further with the SEM. Argon ion milling samples made microfabric characterization much easier, as it produced high quality surfaces with minimal artifacts. SEM proved to be an excellent tool for observation of pores, sulfide morphology, fossils, mineral grains, and fracture-filling cement. SEM, coupled with EDS, allowed for rapid and straightforward determination of those mineral grains. Together, CT and SEM/EDS data complemented each other very well. While CT was used to pinpoint areas for further high quality imaging and analysis, the data gathered from those areas with SEM/EDS was used to supplement interpretations made from the lower resolution CT data. A good example of this reciprocal relationship comes from the Gorgas core sample (Fig. 60). SEM images of the different pore types (Figs. 57, 58) were used to ground-truth the interpretations of the pore types that were seen from a CT slice of that same sample (Fig. 60). The two datasets work seamlessly together and thoroughly bridge the gap from micro- to nano-scale observations.

V. 11 CT strategy and shale workflow

Altogether, it is apparent that CT scanning is a very useful tool for shale characterization. Yet, a CT scanning workflow for rock imaging and analysis has not been firmly established. This is because micro-CT scanning of geological media is in its infancy. The following paragraph

outlines a generalized step-by-step process for CT scanning rocks that is designed to benefit future investigators (Fig. 61).

Using core descriptions and other data as a guide, an area with distinctive features (e.g., sedimentary structures, fossils, diagenetic structures, etc.) is chosen for closer inspection via CT analysis. Using a precision saw with a diamond blade, a sample is cut from the core slab, with the dimensions tailored to what is attempting to be imaged. The sample is then mounted in the scanner and scanning conditions are determined. After scanning, the scan file is processed to eliminate sample shifting and beam hardening that occurred during the scan. Reconstructed CT slices are generated and a continuous stack of the slices can be created to make a 3D volume. Various types of image software can then be used to perform qualitative inspections and quantitative operations on the reconstructed sample. Samples can be viewed as 2D slices in the XY, XZ and YZ directions. Samples can also be viewed in full or cropped 3D volumes. Density filters enable the user to highlight various features. Applying cutoffs to a histogram of a scans gray values allows the user to isolate features of interest and visualize them in 3D. Volumetric calculations can also be performed with histogram cutoffs.

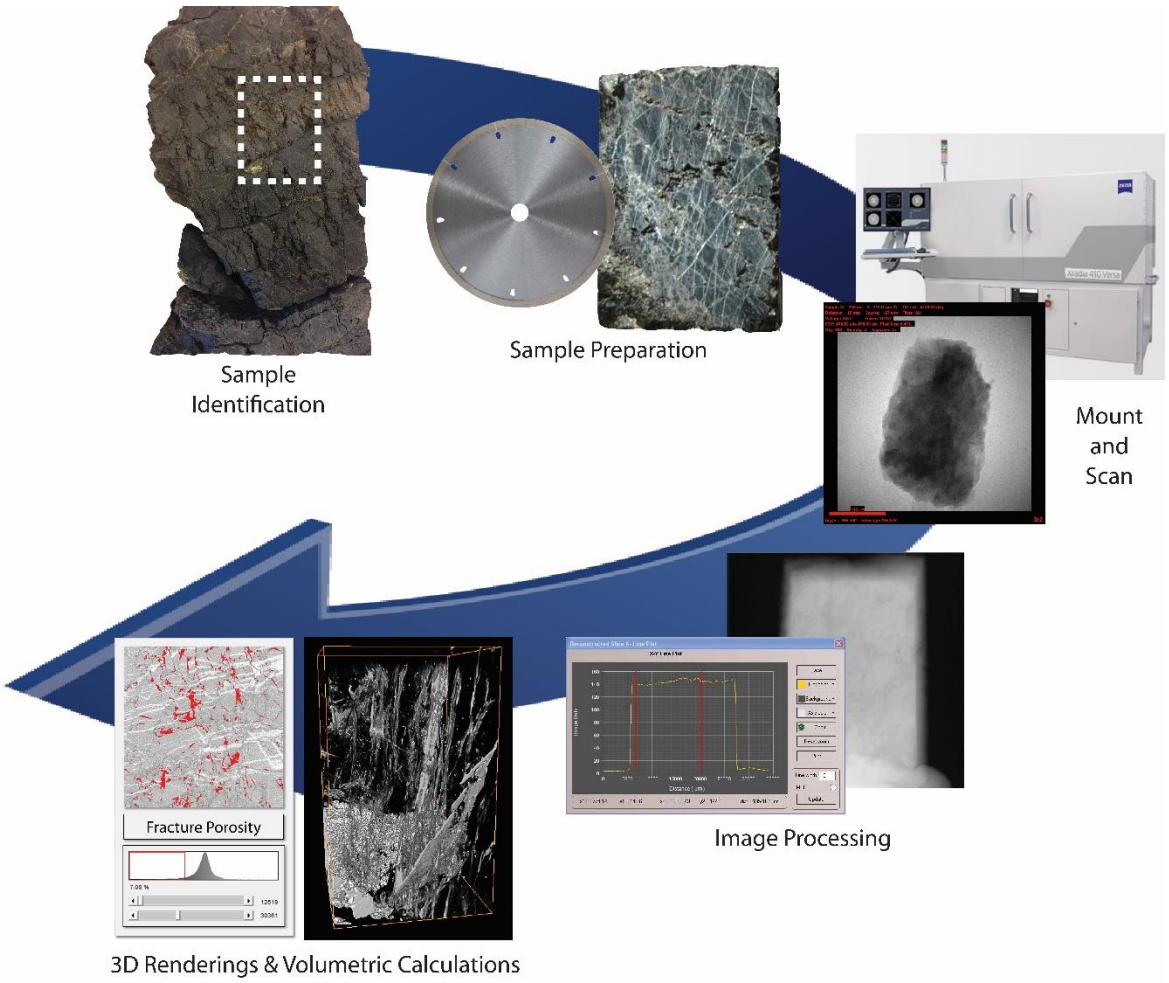

Figure 61. CT scanning strategy outlining the steps from sample identification to qualitative and quantitative data gathering.

It is desirable to develop a plan for each sample based on what is observed in hand samples, thin sections, and the available geologic, petrologic, geochemical, and petrophysical data (Fig. 62). It is further desirable to begin with an understanding of the capabilities and limitations of the CT microscope that is being used. While micro-CT has proven itself to be a useful tool in the field of shale research, it is but one component of the systematic approach that is required to adequately study shale. A robust workflow that covers a large scale of observations must be implemented to in order to understand the characteristics and origin of shale. Micro-CT scanning makes a great addition to this type of workflow because it helps bridge gaps among

different analyses. Conversely, interpretation of CT scan results is informed by the data gathered from other analytical tools. With CT being an evolving technology, data gathered from micro-CT analysis will only get better. Higher magnification objectives will allow for improved resolution. Also, a wider range of x-ray energy will enable larger samples to be scanned while maintaining an adequate contrast and will serve to enhance the contrast of scans on very small samples. Higher resolution and enhanced contrast will greatly improve geologic investigations.

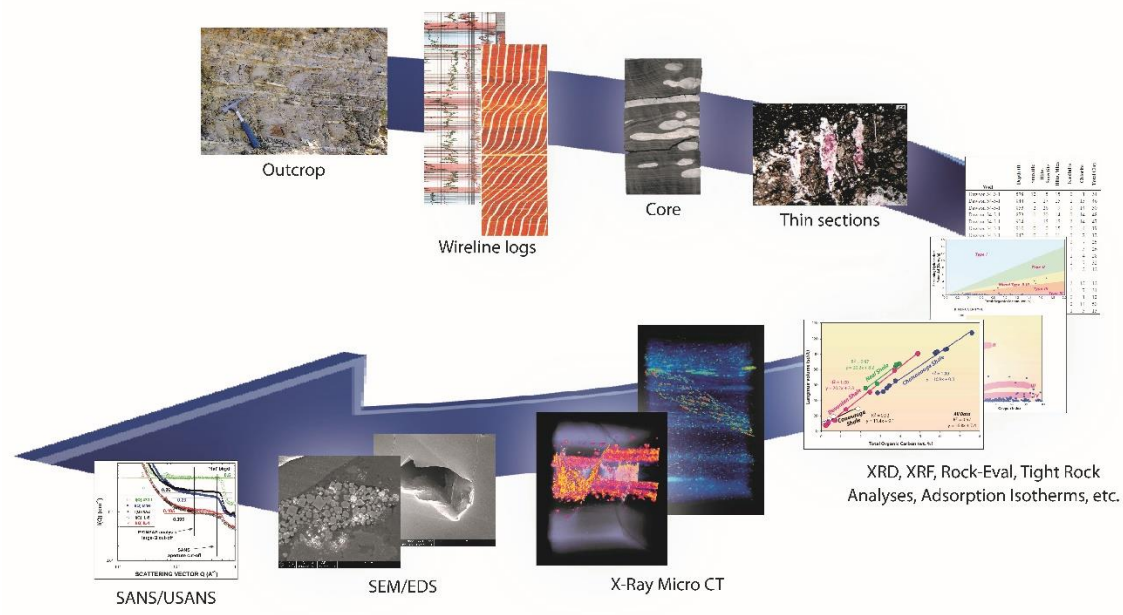

Figure 62. Integrated workflow for shale from megascopic to nano-scale data analysis.

CHAPTER VI

CONCLUSIONS

Shale is of enormous economic importance because it has sourced the majority of the world's hydrocarbons, forms the majority of the world's reservoir seals and has now emerged as a world-class reservoir rock. Nonetheless, shale is amongst the least understood of all sedimentary rock types (Wignall, 1994). A major reason for the lack of understanding of argillaceous rocks is difficulty of analysis. Non-routine methods are required to identify small textural and structural features that can normally be observed with the naked eye or a hand lens in coarser-grained rocks (O'Brien and Slatt, 1990). This thesis helps overcome this obstacle by demonstrating an approach to the systematic analysis of argillaceous rocks. The approach provides a framework for characterizing shale and improving interpretations of sedimentary, structural, and reservoir processes.

CT is a technique for visualizing features in the interior of opaque solid objects, and for obtaining digital information on their 3-D geometries and properties. It requires relatively little sample preparation and is a powerful extension to traditional petrographic analysis, as it allows observations and measurements to be extended into three dimensions. Even at its simplest, data can be visualized to observe texture and structure in sedimentary rocks. Micro-CT differs from conventional medical CAT-scanning in its ability to resolve details as small as 0.1 μm in size,

even when imaging objects consisting of high density materials. Due to its origin outside of the earth sciences, exploring applications to geological problems is still in its infancy.

A variety of major rock features were observed using micro-CT scanning. Micro-scale observations of rock fabric were made that include mineral grains, matrix materials, and pores. Physical sedimentary structures like laminae and ripples were imaged. In addition, biogenic sedimentary structures, including trace fossils and body fossils, also were imaged. Diagenetic features were observed, such as phosphate nodules and a range of sulfide forms. Lastly, fracture and fault geometry was easily discerned for both open and mineralized fracture and fault networks.

In addition to the unparalleled qualitative data that can be gathered through two- and three-dimensional observations, CT is also a very powerful method for semi-quantitative analysis. Using image analysis software, volumetric data can be collected. This is demonstrated by the percentage of fracture porosity and mineral constituent volumes that were estimated in this study. While volumetrics for porosity were not calculable from the shale samples that were scanned in this study, the ability of the machine to resolve ≥ 3 μm pores may be of interest to geoscientists interested in performing porosity studies on macroporous sedimentary rocks.

SEM/EDS data from this study were used in concert with the CT data that was gathered. The CT was used for identifying locations in which the microfabric could be further analyzed using SEM. SEM proved to be an excellent tool for observation of pores, sulfide morphologies, fossils and mineral grains, and the high resolution of the SEM images relative to the CT scans provided a wealth of information that was instrumental for the interpretation of the CT data. EDS, moreover, allowed for rapid identification of minerals by determining major element composition.

While the work here demonstrated the power of integrating CT into argillaceous rock analysis, there are still several limitations of the instrument. Resolution of the machine that was used is limited to 1/1,000th the cross-sectional diameter of the scan. Finite resolution can cause blurring of material boundaries. As such, a high resolution scan with high contrast requires small samples. Accordingly, the greatest significance should be placed on the amount of contrast a scan will generate, as it determines the overall quality of a scan. A long scan can be performed on a small volume within a large sample to obtain high resolution, but a large sample requires high x-ray energy and long scan times that may not be practical. And the higher the x-ray energy, the less contrast a scan will yield. With less contrast, a lower number of gray values will be derived, and rock features will be muted.

Experience with the Xradia VersaXRM 410 indicates that sample size should be tailored to what is attempted to be imaged. Not all features within a rock have sufficiently large attenuation contrast for effective imaging. Although a sedimentary structure may exist within a rock, it will appear homogenous if there is no density contrast. For example, while calcareous fossils in argillaceous matrix were imaged effectively, they may not have been resolvable had they been preserved in limestone. Lastly, CT produces large volumes of data (gigabytes to terrabytes) and requires large storage devices and considerable computer resources for visualization and quantitative analysis.

While these may be pitfalls in modern CT analysis, they undoubtedly will be areas of future advancement, as CT is an evolving technology. Overall, this study has demonstrated the usefulness of incorporating CT analysis into shale studies by exhibiting the wide variety of observations that can be made. Micro-CT provides a nondestructive way to image shale samples in three dimensions and facilitates in the identification of heterogeneity and inspection of sedimentary features (e.g., rock fabric, physical and biogenic sedimentary structures, diagenetic structures, fractures, and faults). By observing these characteristics, how microfabric relates to

macrostructure, sedimentary processes, and tectonic processes can be determined. In addition to shale studies, this work provides a foundation for applying CT analysis to studies of other rock types.

REFERENCES

Ashi, J., 1993, CT scan analysis of sediments from leg 1461: Proceedings of the Ocean Drilling Program, Scientific Results, p. 191-199

Astini, R.A., Thomas, W.A., and Osborne, W.E., 2000, Sedimentology of the Conasauga Formation and equivalent units, Appalachian thrust belt in Alabama, The Conasauga Formation and equivalent units in the Appalachian thrust belt in Alabama. Alabama Geological Society 31st Annual Field Trip Guidebook, p. 41-71.

Berner, R.A., 1980, Early Diagenesis: A Theoretial Approach: Princeton, Princeton University Press, 241 p.

Berner, R. A., 1984, Sedimentary pyrite formation: an update: Geochimica et Cosmochimica Acta, v. 48, p. 605-615.

Bouma, A.H., 1969, Methods for the study of sedimentary structures: New York, Wiley-Interscience

Callner, S.A., 2014, An integrated approach to understanding sedimentary structures and depositional processes in Devonian-Mississippian black shale: the Woodford Shale and associated strata in the southern midcontinent: unpublished M.S. thesis, Oklahoma State University, 90 p.

Camp, W. K., Diaz, E., and Wawak, B., ed., 2013, Electron microscopy of shale hydrocarbon reservoirs: AAPG Memoir 102, 260 p.

Clark, P.E., Pashin, J. C., Carlson, E. S., Goodliffe, A. M., McIntyre-Redden, M. R., Guohai Jin, Mann, S. D., and Thompson, M., 2013, Site characterization for CO_2 storage from coal-fired power facilities in the Black Warrior Basin of Alabama: Final Report, 219 p.

Cnudde, V., Masschaele, B., Dierick, M., Vlassenbroeck, J., Van Hoorebeke, L., and Jacobs, P., 2006, Recent progress in X-ray CT as a geosciences tool: Applied Geochemistry, v. 21, p. 826-832.

Curtis, M.E., Cardott, B.J., Sondergeld, C.H., and Rai, C.S., 2012, Development of organic porosity in the Woodford Shale with increasing thermal maturity: International Journal of Coal Geology, v. 103, p. 26-31. .

Dierick, M., Cnudde, V., Masschaele, B., Vlassenbroeck, J., Van Hoorebeke, L., and Jacobs, P., 2007, Micro-CT of fossils preserved in amber: Nuclear Instruments and Methods in Physics Research Section A: Accelerators, Spectrometers, Detectors and Associated Equipment, v. 580, p. 641-643.

Downey, M.W., 1984, Evaluating seals for hydrocarbon accumulations: AAPG Bulletin, v. 68, p. 1752-1763.

Dunham, R.J., 1962, Classification of carbonate rocks according to depositional textures, *in* Ham, W.E., ed., Classification of Carbonate Rocks - A Symposium, p. 108-121.

Erdman, N., Campbell, R., and Asahina, S., 2006, Precise SEM cross section polishing via argon beam milling: Microscopy Today, v. 14, p. 22-25.

Everhart, T., and Thornley, R., 1960, Wide-band detector for micro-microampere low-energy electron currents: Journal of Scientific Instruments, v. 37, p. 246.

Ferrill, D.A., Morris, A.P., Hennings, P.H., and Haddad, D.E., 2014, Faulting and fracturing in shale and self-sourced reservoirs: Introduction: AAPG Bulletin, v. 98, p. 2161-2164.

Folk, R.L., 1959, Practical petrographic classification of limestones: AAPG Bulletin, v. 43, p. 1-38.

___1974, Petrology of Sedimentary Rocks (3 ed.): Austin, The University of Texas, Hemphill's Bookstore, 178 p.

Gale, J.F., Laubach, S.E., Olson, J.E., Eichhubl, P., and Fall, A., 2014, Natural fractures in shale: A review and new observations: AAPG Bulletin, v. 98, p. 2165-2216.

Gale, J.F., Reed, R.M., and Holder, J., 2007, Natural fractures in the Barnett Shale and their importance for hydraulic fracture treatments: AAPG Bulletin, v. 91, p. 603-622.

Goldstein, J., Newbury, D.E., Echlin, P., Joy, D.C., Romig Jr, A.D., Lyman, C.E., Fiori, C., and Lifshin, E., 2012, Scanning electron microscopy and X-ray microanalysis: a text for biologists, materials scientists, and geologists, Springer Science & Business Media, 807 p.

Hill, R.J., and Jarvie, D.M. (eds.), 2007, Barnett Shale: AAPG Bulletin, v. 91, p. 399-622.

Holler, P., and Kögler, F.-C., 1990, Computer tomography: a nondestructive, high-resolution technique for investigation of sedimentary structures: Marine Geology, v. 91, p. 263-266.

Hu, Q., Ley, M.T., Davis, J., Hanan, J.C., Frazier, R., and Zhang, Y., 2014, 3D chemical segmentation of fly ash particles with X-ray computed tomography and electron probe microanalysis: Fuel, v. 116, p. 229-236.

Ketcham, R.A., 2005, Computational methods for quantitative analysis of three-dimensional features in geological specimens: Geosphere, v. 1, p. 32-41.

Ketcham, R.A., and Carlson, W.D., 2001, Acquisition, optimization and interpretation of X-ray computed tomographic imagery: applications to the geosciences: Computers & Geosciences, v. 27, p. 381-400.

Ketcham, R.A., and Iturrino, G.J., 2005, Nondestructive high-resolution visualization and measurement of anisotropic effective porosity in complex lithologies using high-resolution X-ray computed tomography: Journal of Hydrology, v. 302, p. 92-106.

Klemme, H., and Ulmishek, G.F., 1991, Effective petroleum source rocks of the world: stratigraphic distribution and controlling depositional factors (1): AAPG Bulletin, v. 75, p. 1809-1851.

Kvale, E., 2014, Depositional Implications of Museum-Quality Terrestrial Ferns in Deep Water Wolfcamp Formation: Denver, Unconventional Resources Technology Conference Proceedings, unpaginated.

Kyle, J.R., and Ketcham, R.A., 2015, Application of high resolution X-ray computed tomography to mineral deposit origin, evaluation, and processing: Ore Geology Reviews, v. 65, p. 821-839.

Lewan, M., 1978, Laboratory classification of very fine grained sedimentary rocks: Geology, v. 6, p. 745-748.

Loucks, R.G., Reed, R.M., Ruppel, S.C., and Hammes, U., 2012, Spectrum of pore types and networks in mudrocks and a descriptive classification for matrix-related mudrock pores: AAPG Bulletin, v. 96, p. 1071-1098.

Louk, A.K., 2014, Sequestration in unconventional reservoirs—results from the Emory River "huff and puff" test (abstract): Lexington, University of Kentucky, Center for Applied Energy Research, Eastern Unconventional Oil and Gas Symposium Proceedings, unpaginated.

McBride, E.F., 1963, A classification of common sandstones: Journal of Sedimentary Research, v. 33, p. 664-669.

Mees, F., Swennen, R., Van Geet, M., and Jacobs, P., 2003, Applications of X-ray computed tomography in the geosciences: Geological Society (London) Special Publication 215, p. 1-6.

Morad, S., and Al-Aasm, I., 1994, Conditions of formation and diagenetic evolution of Upper Proterozoic phosphate nodules from southern Sweden: evidence from petrology, mineral chemistry and isotopes: Sedimentary Geology, v. 88, no. 3, p. 267-282.

Nuttall, B.C., Drahovzal, J.A., Eble, C.F., and Bustin, R.M., 2009, Regional assessment of suitability of organic-rich gas shales for carbon sequestration: An example from the Devonian shales of the Illinois and Appalachian basins, Kentucky, AAPG Studies in Geology 59, p. 173-90

O'Brien, N.R., and Slatt, R.M., 1990, Argillaceous rock atlas: New York, Springer-Verlag, 141 p.

Pashin, J.C., 1993, Tectonics, paleoceanography, and paleoclimate of the Kaskaskia sequence in the Black Warrior basin of Alabama, *in* Pashin, J.C., ed., New Perspectives on the Mississippian System of Alabama: Alabama Geological Society 30th Annual Field Trip Guidebook, p. 1-28.

___1994, Cycles and stacking patterns in Carboniferous rocks of the Black Warrior foreland Basin: Gulf Coast Association of Geological Societies Transactions, v. 44, p. 555-563.

___2004, Cyclothems of the Black Warrior Basin, Alabama, USA: Eustatic snapshots of foreland basin tectonism, *in* Gastaldo, R., and Pashin, J.C., eds., Sequence stratigraphy, paleoclimate, and tectonics of coal-bearing strata: AAPG Studies in Geology 51, p. 199-217.

___2008, Gas shale potential of Alabama: Tuscaloosa, University of Alabama, College of Continuing Studies, 2008 International Coalbed & Shale Gas Symposium Proceedings, paper 0808, 13 p.

Pashin, J.C., Grace, R.L.B., and Kopaska-Merkel, D.C., 2010, Devonian shale plays in the Black Warrior basin and Appalachian thrust belt of Alabama: Tuscaloosa, University of Alabama, College of Continuing Studies, 2010 International Coalbed & Shale Gas Symposium Proceedings, paper 1016, 20 p.

Pashin, J.C., and Gastaldo, R.A., 2009, Carboniferous of the Black Warrior basin, *in* Greb., S. F., and Chesnut, D. R., eds., Carboniferous Geology and Biostratigraphy of the Appalachian Basin: Kentucky Geological Survey Special Publication 10, p. 10-21.

Pashin, J.C., Kopaska-Merkel, D.C., Arnold, A.C., McIntyre, M.R., and Thomas, W.A., 2012, Gigantic, gaseous mushwads in Cambrian shale: Conasauga Formation, southern Appalachians, USA: International Journal of Coal Geology, v. 103, p. 70-91.

Pashin, J.C., Kopaska-Merkel, D.C., Arnold, A.C., and McIntyre, M.R., 2011, Geological foundation for production of natural gas resources from diverse shale formations: Sugarland, Texas, Research Partnership to Secure Energy for America Final Report, 156 p.

Passier, H.F., Middelburg, J.J., de Lange, G.J., and Böttcher, M.E., 1997, Pyrite contents, microtextures, and sulfur isotopes in relation to formation of the youngest eastern Mediterranean sapropel: Geology, v. 25, p. 519-522.

Penney, D., Dierick, M., Cnudde, V., Masschaele, B., Vlassenbroeck, J., Van Hoorebeke, L., and Jacobs, P., 2007, First fossil Micropholcommatidae (Araneae), imaged in Eocene Paris amber using X-ray computed tomography: Zootaxa, v. 1623, p. 47-53.

Potter, P.E., Maynard, J.B., and Pryor, W.A., 1980, Sedimentology of Shale: Study Guide and Reference Source: New York, Springer-Verlag, 303 p.

Rheams, K.F., and Neathery, T. L., 1988, Characterization and geochemistry of Devonian oil shale, north Alabama, northwest Georgia, and south-central Tennessee (a resource evaluation): Alabama Geological Survey Bulletin, v. 128, 214 p.

Ross, D.J., and Bustin, R.M., 2008, Characterizing the shale gas resource potential of Devonian–Mississippian strata in the Western Canada sedimentary basin: Application of an integrated formation evaluation: AAPG Bulletin, v. 92, p. 87-125.

Schieber, J., 1998, Deposition of mudstones and shales: Overview, problems, and challenges: Stuttgart, Schweizerbart'sche Verlagsbuchhandlung, Shales and Mudstones: Basin Studies, Sedimentology and Paleontology, p. 187-215.

Schieber, J., and Baird, G., 2001, On the origin and significance of pyrite spheres in Devonian black shales of North America: Journal of Sedimentary Research, v. 71, p. 155-166.

Schieber, J., 2011, Shales, Encyclopedia of Geobiology: Springer Verlag, p. 785-791.

Scott, G., 1978, Deposition, Facies Patterns, and Hydrocarbon Potential of Bangor Limestone (Mississippian) Northern Black Warrior Basin, Alabama and Mississippi, Mississippi Geological Society Guidebook, 17th Annual Field Trip, p. 34-54.

Shepard, F. P., 1954, Nomenclature based on sand-silt-clay ratios: Journal of Sedimentary Research, v. 24, p. 151-158.

Shirai, M., Nishimura, M., and Yasuda, H., 2007, Data report: descriptive evaluation of consolidated sedimentary rock structures with x-ray imaging: examples from site 1276 core samples *in* Tucholke, B.E., Sibuet, J.C., and Klaus, A., eds., Proceedings of the Ocean Drilling Program: Scientific Results, v. 210, p. 1-21.

Slatt, R.M., and O'Brien, N.R., 2011, Pore types in the Barnett and Woodford gas shales: Contribution to understanding gas storage and migration pathways in fine-grained rocks: AAPG Bulletin, v. 95, p. 2017-2030.

Soh, W., Byrne, T., Taira, A., and Kono, A., 1993, Computed tomography (CT) scan image analysis of site 808 cores: structural and physical property implications *in* Hill, I.A., Taira, A., and Firth, J.V., eds., Proceedings of the Ocean Drilling Program: Scientific Results, v. 131, p. 135-140.

Spanne, P., Thovert, J., Jacquin, C., Lindquist, W., Jones, K., and Adler, P., 1994, Synchrotron computed microtomography of porous media: topology and transports: Physical Review Letters, v. 73, p. 2001-2004.

Surdam, R. C., ed., 1997, Seals, traps, and the petroleum system: AAPG Memoir 67, 317 p.

Taud, H., Martinez-Angeles, R., Parrot, J., and Hernandez-Escobedo, L., 2005, Porosity estimation method by X-ray computed tomography: Journal of Petroleum Science and Engineering, v. 47, p. 209-217.

Taylor, K.G., and Macquaker, J.H.S., 2000, Early diagenetic pyrite morphology in a mudstone-dominated succession: the Lower Jurassic Cleveland Ironstone Formation, eastern England: Sedimentary Geology, v. 131, p. 77-86.

Thomas, W.A., 1972, Mississippian stratigraphy of Alabama: Alabama Geological Survey Monograph 12, 121 p.

___1974: Evolution of Appalachian-Ouachita salients and recesses from reentrants and promontories in the continental margin: American Journal of Science, v. 277, p. 1233-1278.

___1988, The Black Warrior basin, *in* Sloss, L.L., ed., Sedimentary cover—North American craton; U.S.: Geological Society of America, The Geology of North America, p. 471 - 492.

___2001, Mushwad: Ductile duplex in the Appalachian thrust belt in Alabama: AAPG Bulletin, v. 85, p. 1847-1869.

Thomas, W.A., Astini, R.A., Osborne, W.E., and Bayona, G., 2000, Tectonic framework of deposition of the Conasauga Formation, The Conasauga Formation and equivalent units in the Appalachian thrust belt in Alabama: Tuscaloosa, Alabama Geological Society 31st Annual Field Trip Guidebook, p. 19-40.

Thomas, W.A., and Mack, G.H., 1982, Paleogeographic relationship of a Mississippian barrier-island and shelf-bar system (Hartselle Sandstone) in Alabama to the Appalachian-Ouachita erogenic belt: Geological Society of America Bulletin, v. 93, p. 6-19.

Trask, P.D., and Patnode, H.W., 1942, Source beds of petroleum: AAPG Special Publication, v. 1, 556 p.

Wellington, S., and Vinegar, H., 1987, X-ray computerized tomography: Journal of Petroleum Technology, v. 39, p. 885-898.

Wignall, P.B., 1994, Black shales: Oxford, Oxford University Press, 127 p.

VITA

Michael Ray Powers

Candidate for the Degree of

Master of Science

Thesis: EXPLORING MICRO X-RAY COMPUTED TOMOGRAPHY COUPLED WITH SCANNING ELECTRON MICROSCOPY AS TOOLS FOR PALEOZOIC SHALE STUDIES

Major Field: Geology

Biographical: Michael Powers was born and raised in Bowling Green, Kentucky where he developed a passion for geology and aspirations to become a petroleum geologist.

Education:

Completed the requirements for the Master of Science in Geology at Oklahoma State University, Stillwater, Oklahoma in December, 2015.

Completed the requirements for the Bachelor of Science in Geology at Western Kentucky University, Bowling Green, Kentucky/United States in 2013.

Experience: Internship at SM Energy (1 summer), Internship at ConocoPhillips (1 summer)

Professional Memberships: AAPG, GSA